First-Principle Investigations of C-H bond Activation on Nickel Oxide: Electrochemical Activation of Methane and Oxidative Dehydrogenation of Ethane

by
Qianyu Ning

A dissertation submitted to the
William A. Brookshire Department of Chemical and Biomolecular Engineering,
Cullen College of Engineering
in Partial Fulfillment of the Requirements for the Degree of

Doctor of Philosophy
In Chemical Engineering

Chair of Committee: Lars C. Grabow

Committee Member: Jeffrey Rimer

Committee Member: Praveen Bollini

Committee Member: T. Randall Lee

Committee Member: Omar Abdelrahman

University of Houston
December 2021

Acknowledgments

First of all, I would like to gratefully express my appreciation to my Ph.D. advisor Dr. Lars Grabow. He has enlightened my scope of research and encouraged me on both aspects of academic and daily life. During these five years of Ph.D. study, he has always been a patient, supportive and enthusiastic mentor. He has accompanied me with his insightful thoughts to overcome the difficulties and challenges that I have ever met. I deeply appreciate the opportunity to work with him and the skills developed under his invaluable guidance which are in great value for my future career.

I would like to acknowledge the cooperation with Xiaohui Zhao who is co-advised by Dr. Praveen Bollini and Dr. Jeffrey Rimer. She has been a wonderful collaborator who has excellent experimental skills as well as valuable ideas. I would also like to thank the collaboration with Dr. Hung-Vu Tran from Dr. Randall Lee's group. Working with him has widened my research area and has given me the opportunity to gain more valuable research skills. I also want to thank Dr. Jeffrey Rimer, Dr. Praveen Bollini, Dr. Randall Lee and Dr. Omar Abdelrahman for serving on my committee and providing insightful thoughts.

I would not be able to accomplish my Ph.D. research without the computational resources provided by RCDC from University of Houston, Department of Energy - NERSC, and XSEDE from Texas Advanced Computing Center, that I could always trust to run thousands of calculations. It is the fast-developing supercomputing resources that enabled me to discover the world in the atomic level.

Moreover, I own the special thanks to all members from Grabow group. They are all wonderful people to work with. I would like to express my appreciation to Dr. Hari Thirumalai, Dr. Yuying Song, Dr. Sashank Kasiraju, Dr. Shengguang Wang, Dr. Juan Manuel Arce-Ramos and Dr. Xiao Li for not only their mentorship at the beginning of my research but also their kind assistance and suggestion throughout my Ph.D. study. I also want to thank Dr. Quan Do, Dr. Unmesh Menon, Dr. Sravan Kumar, Dr. Karun Kumar Rao, Mushfikur Rahman, Deependra Parmer, Pak Wing Chen, Chenghao Wang, Yu Liu, Surya Pratap Singh Solanki and Kai Wu for being willing to provide excellent ideas and help me through tough times. They have created a wonderful group environment and I will always be missing the time that we worked and had fun together.

I also want to thank all the old friends back in China who have always be by my side no matter how far away I am, and the new friends that I've made in Houston for their accompany and support. They have shared both my happy and sad time. My life here would have been much more boring without the time spent with my friends.

Besides, the help and support from all the UH stuff are invaluable to me. I want to thank for their patience in issuing all the paperworks throughout my Ph.D. study in UH. The wonderful campus environment, especially the recreation center, which is one of the best gyms in universities of America, has added more color to my Ph.D. life here in UH. I have not only gained a lot fun exercising, but also had the chance to watch football and basketball games and felt so proud for being a student from UH.

Last but not least, I would like to express my gratitude to my lovely family. I was raised up in a family full of love and energy. They have always been supportive to me especially during the time of pandemic. My grandfather passed away the beginning of

this year while I was stuck in a country thousands of miles away from home. I would have not been able to make it through without the unconditional love and accompany from my family. No matter where I am or what I am pursuing, they will always be there for me and I will do my best to love and support them as well.

Abstract

Computational design of heterogeneous catalysts requires a detailed understanding of reaction mechanisms and the identification of active sites. Over the last decades, density functional theory (DFT) has evolved as the standard tool for investigating catalytic reactions, because it can make *ab initio* predictions of surface properties, allowing for the estimation of thermodynamic and kinetic parameters of elementary reaction steps. In this dissertation, DFT calculations were performed to elucidate the mechanism of C-H bond activation thermodynamically stable hydrocarbons such as methane and ethane, the primary components of abundant natural gas.

First, methane conversion to methanol assisted by pre-adsorbed CO_3 and O on both Ni(111) and NiO(100) surfaces were studied. The direct formation of methanol, either activated by CO_3 or O on Ni(111) has high activation barriers and thus, is not likely to proceed. Conversely, a direct pathway to methanol was discovered on the NiO(100) surface, which involves an oxygen adatom and mimics the radical rebound mechanisms previously reported for various single site catalysts. Despite the transient formation of a methyl radical, this pathway is energetically preferred over other mechanisms involving the highly activated C-O bond formation step between adsorbed CH_3 and OH intermediates.

Relevant to the electro-oxidation of methane, we then investigated the sensitivity of the methane-to-methanol reaction on NiO(100) to the presence of (oscillating) electric fields. Our DFT results show that positive and negative electric fields favor different elementary steps in the reaction cycle, indicating that the overall reaction can be accelerated with a dynamically applied, oscillating potential.

The oxygen adatom site on NiO(100) also plays a critical role as active site for the first C-H bond activation step in the oxidative dehydrogenation (ODH) of ethane. This conclusion is supported CO_2 adsorption experiments, FTIR spectroscopy, and reactivity measurements contributed by our experimental collaborators. These experiments showed that CO_2 can be used as probe molecule to titrate two distinct active oxygen sites, and DFT calculations suggest that nearby Ni vacancies are required. These sites were identified by matching the calculated CO_2 vibrational fingerprints and the experimental FTIR spectra of CO_2 adsorption. Combining the experimental results of the ODH reaction and the calculated reaction enthalpy, we were able to propose a reaction cycle involving two active oxygen sites near Ni vacancies with different activity: the more active non-stoichiometric oxygen adatoms are readily passivated by CO_2, whereas the less reactive lattice oxygen persists in the presence of CO_2 at reaction temperature. These outcomes provide fundamental insight into the role of non-stoichiometric oxygen in metal oxides and help guide the future design of catalysts with tailored surface oxygen population for ODH reactions.

Overall, this dissertation demonstrates the power of *ab initio* simulations in assisting the interpretation of experimental observations. This concept can be extended to other non-catalytic systems, such as providing an explanation for the reported odd-even effect in the experimentally measured wettability of organic self-assembled monolayers (SAMs). Here, our *ab initio* molecular dynamics (AIMD) simulations provided insight into dipole moments at the SAMs-liquid interface that can be tailored by different tail groups and number of CH_2 units in the carbon chain. Other than aiding the interpretation of experiments, we have also discovered novel mechanisms and used DFT to predict

how oscillating electric fields may be leveraged to accelerate methane electro-oxidation to methanol.

Table of Contents

List of Tables

Appendix

List of Figures

Appendix

Chapter 1. Introduction

1.1. Catalysis

According to the definition of International Union of Pure and Applied Chemistry (IUPAC) Gold Book, a catalyst is a substance that increases the rate of a reaction without modifying the overall standard Gibbs energy change in the reaction. In other words, the catalyst is both a reactant and product of the reaction. Catalysis can be classified as homogeneous catalysis, in which only one phase is involved, heterogeneous catalysis, in which the reaction occurs at or near an interface between phases, and enzymes, the catalysts of nature. A catalyst increases the reaction rate by decreasing the energy of the transition state or enabling a reaction pathway that has a lower activation barrier (Figure 1-1). Well-developed catalysts have been applied in industry over decades and result in a great socio-economic impact by lowering the cost for chemical productions and reducing the energy input to industrial processes. One of the best-known and commercialized catalytic processes is the Haber-Bosch process that converts nitrogen and hydrogen to ammonia using iron catalyst. Ammonia fertilizer is essential for increasing the crop yields and thus, the Haber-Bosch process is considered to be one of the most important technologies in the 20th century.

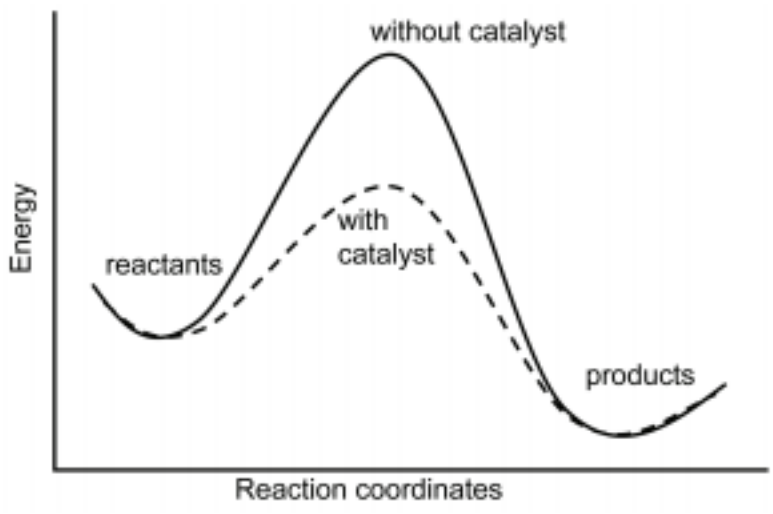

Figure 1-1. General principles of catalysis

Improvement of catalytic performance has been widely investigated to increase product selectivity and yield, and to reduce the energy cost by moderating operating conditions and lowering the pressure and temperature requirement of catalytic processes. This is normally done by modifying the catalyst topologies and introducing sites that are more active for the reaction. Density functional theory (DFT) can be applied to simulate the atomic interactions between reaction intermediates and the catalyst surface. Despite the large gap between the idealized catalyst structures used in modeling and real-life catalyst, the calculated binding energies and activation barriers have proven to be useful for predicting catalytic performance trends and identifying reaction mechanisms.

1.2. Catalytic C-H Bond Activation of Hydrocarbons

The short-chain hydrocarbons, such as methane and ethane, are the major components of natural gas. In addition to being used as fuel, methane and ethane are also important feedstocks for the production of chemicals such as syngas, olefins,

alcohols, ammonia etc., through catalytic processes, which require high energy input because of the strong, non-polar C-H bonds in methane and ethane.

Methane is primarily used to produce syngas via steam reforming (SMR) and water gas shift (WGS) [1], oxidative reforming (auto thermal reforming (ATR)) [2], partial oxidation (POX)[3], and dry reforming[4]. Syngas is then used for the production of value-added products such as hydrogen, ammonia, methanol and synthetic hydrocarbon fuels. However, the operating temperature of methane reforming normally falls into the range of 800-1100 °C, which reduces the catalyst lifetime drastically, and increases the reactor investment. While challenging to design, catalytic processes that convert methane directly to higher value products are potentially economic at smaller scale and are highly desirable to valorize stranded natural gas resources.

Emerging processes using methane feedstock include oxidative coupling of methane, monohalogenation, or the direct conversion of methane to methanol. Keller [5] and Hinsen[6] have reported that ethylene can be formed via oxidative coupling of methane (OCM) on a variety of metal oxides between 500-1000 °C. As methane conversion increases, however, the selectivity to C_2 products decreases such that the overall yield is limited to 25-30 %.[7]

Catalytic monohalogenation of methane over supported acids of platinum group metals is reported by Olah et al. The reactions were carried out between 180 and 250 °C, giving 8-58 % methane conversion with selectivity towards methyl chloride exceeding 90 %.[8] A following hydrolysis of methyl halides produces methanol and dimethyl ether with varying product yields depending on the water to methyl halides ratio.

Direct conversion of methane to methanol is a promising process to upgrade methane and has attracted great interest. Sajith and colleagues have performed a theoretical study of methane conversion to methanol using H_2O_2 as oxidant on Pd and Au/Pd.[9] The OH produced by H_2O_2 decomposition was found to be able to lower the activation barrier of C-H bond activation on Pt. And alloying Au on Pd further lowers the activation barrier because of the weakly bound OH on Au. Besides, zeolite catalysts containing transition metal ions, such as Cu, Fe and Co, have also been found to be active for the methane oxidation to methanol, albeit with very small overall yields.[10] On zeolites, the direct conversion may be accomplished with both stepwise [11] and continuous[12] processes.

Metal-oxides, another class of important heterogeneous catalysts, have received much less attention as potential catalysts for the direct conversion of methane to methanol. In Chapter 3 we present an *ab initio* mechanistic study of methane conversion to methanol on Ni(111) and NiO(100). Notably, we found that the presence of an oxygen adatom on NiO(100) provides an active site that efficiently catalyzes the radical rebound mechanism leading directly to methanol. A similarly direct pathway to methanol could not be identified on the metallic Ni(111) surface.

The second most abundant component of natural gas is ethane. Its primary commercial use is in steam cracking for the production of ethene, which is the building block of the most widely used plastic, polyethylene. The process is highly endothermic, and the catalysts rapidly deactivate due to the formation of coke.[13] In contrast, oxidative dehydrogenation (ODH) of ethane is exothermic and is receiving growing attention as an alternative process for ethene production. One of the challenges that the ethane ODH

reaction is facing is the low selectivity towards ethene due to the total oxidation of ethane to CO_x. Oyama et al. have reported ethane ODH on vanadium oxide with 26-21 % selectivity to ethene at 8-18 % ethane conversion.[14] Bars and co-workers were able to increase the selectivity by increasing the ethane to O_2 ratio.[15] NiO-based catalyst has been studied by Lemonidou et al. and the non-stoichiometric oxygen (NSO) was reported to be active site for ethane activation, but it is unselective for the ODH reaction.[16] They have also shown that Nb-doped NiO gives higher selectivity towards ethene. The selectivity is proposed to be controlled by the binding site of C_2H_5, the first intermediate formed after activating the C-H bond in ethane: C_2H_5 binding to Ni selectively forms ethene, while C_2H_5 binding to O forms CO_2 eventually.[17]

In Chapter 5 we have used DFT to characterize active sites for ethane ODH on NiO and proposed a reaction mechanism accounting for two different active sites. These sites can be distinguished based on their affinity to CO_2 and the types of carbonates that form on the surface. Moreover, we found that nickel vacancies are necessary to create active oxygen sites. Measurements of turn over frequencies, CO_2 adsorption isotherms and FTIR characterization performed by our experimental collaborators are in good agreement with our computational results and support the conclusion that oxygen adatoms near Ni vacancies bind CO_2 most strongly and are the most active sites for ethane ODH.

1.3. Catalytic Stimuli: Dynamically Promoting the Catalytic Performance

While catalysts help improve chemical reactions in terms of turnover frequencies and selectivities towards desired products, the catalytic performance is limited by the

Sabatier principle.[18] Paul Sabatier has shown that, the catalyst that binds the reactants neither too strongly nor too weakly give the best catalytic performance. The reactants that bind too strongly to the surface will cause poisoning of active sites and a slow product desorption rate, while reactants that bind too weakly will not be activated by the catalyst. The principle can be visualized as the well-known volcano plot shown in Figure 1-2.

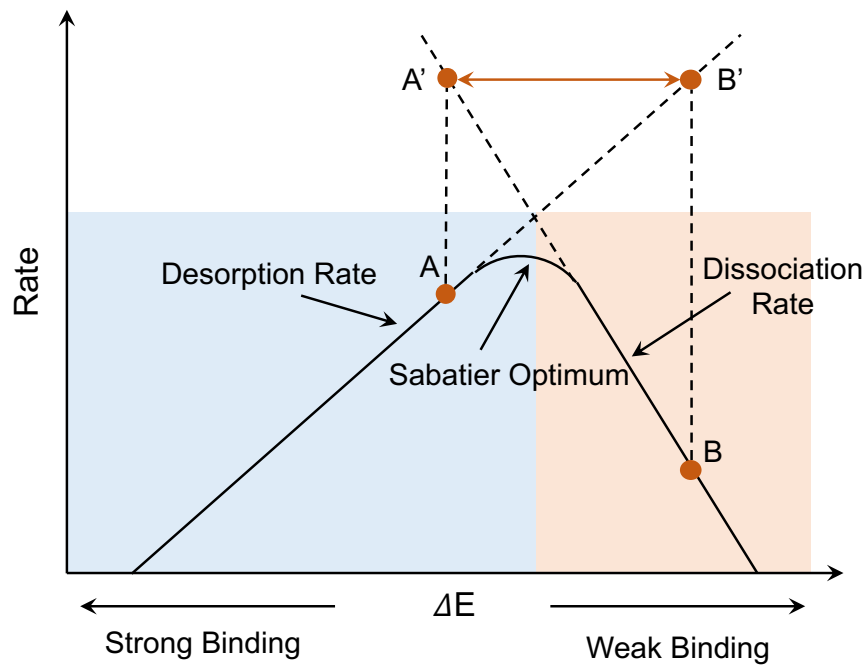

Figure 1-2. The volcano plot based on the Sabatier principle.

At point A, the reaction is limited by product desorption, while at point B, the reaction is limited by the reactant activation. We hypothesize that under dynamically oscillating conditions between A' and B' there exists a dynamic optimum with higher averaged reaction rate above the Sabatier optimum at static condition. Examples of such dynamic rate enhancements have been reported by Shetty et al, where various dynamic

catalyst stimuli were used to improve the overall conversion by accelerating elementary steps independently.[19]

Dynamic catalysis can be divided into two categories: passively changing systems (spontaneously occurring), and systems operated under forced variation/oscillation (external stimulus). Depending on the scale of the chemical dynamics, they can be further divided into the dynamics occurring on the catalyst, throughout the reactor or within a chemical loop.

A seminal demonstration of dynamic rate enhancement under forced dynamic operation is the study by Gopeesingh and co-workers, who have achieved an order of magnitude increase in the rate of formic acid electro-oxidation via dynamic electrocatalytic modulation.[20] The reaction contains a non-Faradaic formic acid dehydration step and the Faradaic CO electrooxidation step, which can be accelerated by a positive potential. Results show that, by applying a square wave oscillating potential between open circuit and 0.8 V, the time averaged turnover frequency of the reaction can have a 10-fold increase comparing with the turnover frequency at steady applied potential of 0.8 V.

Our potential energy diagram for methane electro-oxidation to methanol over NiO(100) as function of applied potential in Chapters 3 and 4 suggests that a similar rate enhancement may be expected when alternating potentials are applied. Our theoretical predictions show that the forward reaction is promoted by a positive electric field, while the reactant adsorption and product desorption are favored by a negative electric field. The process shows great similarity to the reaction discussed by Gopeesingh.[20] Thus, the reaction rate is expected to increase by applying oscillating

potentials between positive and negative potentials; however, this hypothesis requires further studies and verification. Moreover, the optimal frequency and amplitude of the oscillation needs to be investigated.

1.4. Odd-Even Effect in Self-Assembled Monolayers

A self-assembled monolayer (SAM) is a one-molecule thick layer of material that binds to a surface in an ordered fashion as a result of physical or chemical forces during a deposition process.[21] As shown in Figure 1-3, SAMs are formed by the chemisorption of head groups to a substrate, followed by the self-organization of the tail groups.[22,23]

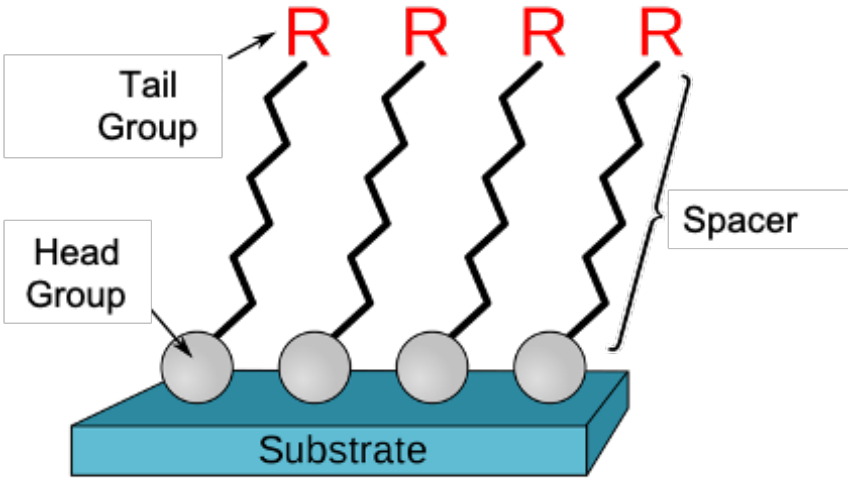

Figure 1-3. Schematic representation of a self-assembled monolayer.

SAMs can be used as surface coating for the control of wettability,[24] bio compatibility and sensitization.[25] They can also be leveraged to modify the electronic structure of the host material.[26-28] One organic SAM of interest is the self-assembled alkanethiolate monolayer formed on the Au(111) surface.[29] As shown in Figure 1-4a the geometry can be described by the tilt angle α, the angle between the zigzag carbon skeleton and the surface normal, and the twist angle β, the rotation of the plane

containing the carbon skeleton along the long axis of the alkyl chain. When the tilt angle α is 0°, the orientations of the terminal CH_3 groups are identical for SAMs with an odd or even number of CH_2 units (Figure 1-4b,e). However, when α is not 0°, the tail CH_3 group of SAMs with an odd or even number of CH_2 units will have different orientations (Figure 1-4c,f). Thus, perfectly ordered SAMs often exhibit properties with an odd-even effect that can be tuned by the number of CH_2 units in the carbon chain.

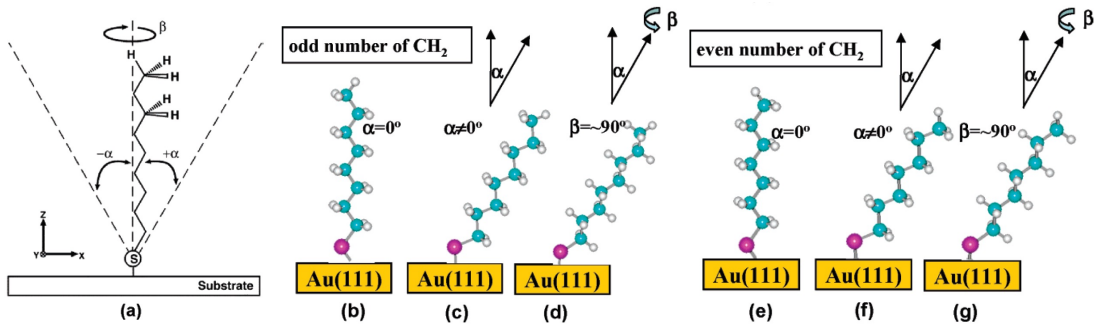

Figure 1-4. (a) Scheme of the tilt angle α and twist angle β. Geometries of alkyl chains of $CH_3(CH_2)_nS$-Au SAMs with (b-d) n = odd, and (e-g) n = even.[29]

SAMs can be modified by changing the head and tail groups. Arefi and co-workers have reported SAMs with modified head and tail groups (O(H), S(H), and NH_2) of the alkyl chain on the H:Si(111) surface.[30] The functionalized work function and tilt angle of the tail group were observed, as well as the odd-even effect. Zenasni et al. have shown the relation between surface dipole and interfacial properties of fluorinated SAMs.[31] Using polar contacting liquids, the fluorinated SAMs show enhanced wettability than the hydrocarbon SAMs, which can be attributed to the HC-FC dipole. Researchers from the same group have continued the work with more alkyl-terminated fluorinated SAMs and have shown that the HC-FC dipoles have a strong effect on the wettability of the monolayers.[32]

In Chapter 6 we have used *ab initio* molecular dynamics (AIMD) simulations to study the structure and surface dipole properties of self-assembled monolayers of CF_3-terminated *n*-alkyl xanthic acid on Au(111). The tilt angle of the tail group was found to be strongly impacted by the number *n* of $(CH_2)_n$ groups and exhibited a pronounced odd-even effect. Overall, the simulated structures agree well with wettability measurements performed by our collaborator Hung-Vu Tran from Dr. Randall Lee's group. Based on the odd or even number of CH_2 units in the carbon chain, the orientation of the terminal tail group leads to different dipole moments, which in turn imparts and odd-even behavior on the contact angle measurements.

Chapter 2. Methods

2.1. Density Functional Theory

Density functional theory (DFT) has become an important and standard technique for the approximation of electronic structure which can be applied in physics, chemistry and material science. Over decades, the development and employment of DFT have drawn increasing attention and the 1998 Nobel prize in chemistry was shared by Kohn[33] for developing the theory. Figure 2-1 shows the increasing number of papers in the research topic of DFT (grey bars) and the two major fractions of B3LYP (blue bars), which is largely applied in chemistry, and PBE (green bars), which is widely used in material science.[34] A comprehensive description of the history and development of DFT is beyond the scope of this Chapter since it has been well explained and reviewed in the literature and book.[35,36] Here we focus on the fundamental quantum mechanical principles and the application of DFT to calculate the properties of interest.

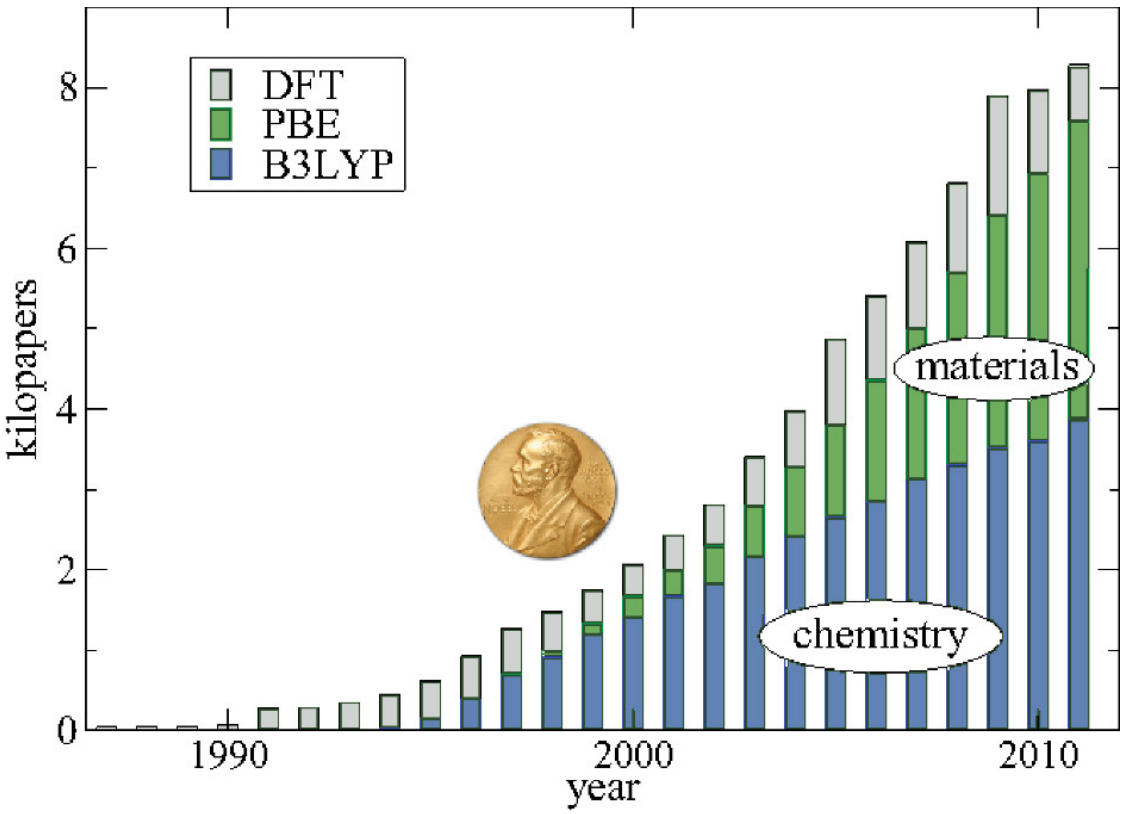

Figure 2-1. Number of papers in the research topic of DFT (grey) and fractions of B2LYP (blue) and PBE (green).[34]

For a many-body system, the energy E can be calculated from the Schrödinger Equation

$$H\psi = E\psi, \tag{2-1}$$

where H is the Hamiltonian operator, and ψ is the corresponding eigenstate of the Hamiltonian, which is also referred to as the wavefunctions. For a system containing N electrons interacting with M nuclei, according to the Born-Oppenheimer approximation that electrons respond much more rapidly than nuclei since nuclei are much heavier than electrons, the system can be treated as electrons interacting with a set of stationary nuclei so that the kinetic energy of nuclei is negligible. Thus, the Hamiltonian can be expanded to

$$\left[-\frac{h^2}{2m}\sum_{i=1}^{N}\nabla_i^2+\sum_{i=1}^{N}V(\boldsymbol{r}_i)+\sum_{i=1}^{N}\sum_{j<i}U(\boldsymbol{r}_i,\boldsymbol{r}_j)\right]\psi=E\psi, \tag{2-2}$$

where the three terms from left to right representing the kinetic energy of electrons, the electron-nuclei interaction energy and the electron-electron interaction energy respectively. However, the Equation 2-2 cannot be fully solved in practical since the wavefunction is a function of the spatial coordinates of the N electrons, which is a $3N$-dimensional wavefunction. For instance, the full wavefunction for a simple system containing one water molecule with 18 electrons is a 54-dimensional wavefunction. Thus, density functional theory considers the electron density instead of the set of individual electrons (Figure 2-2).

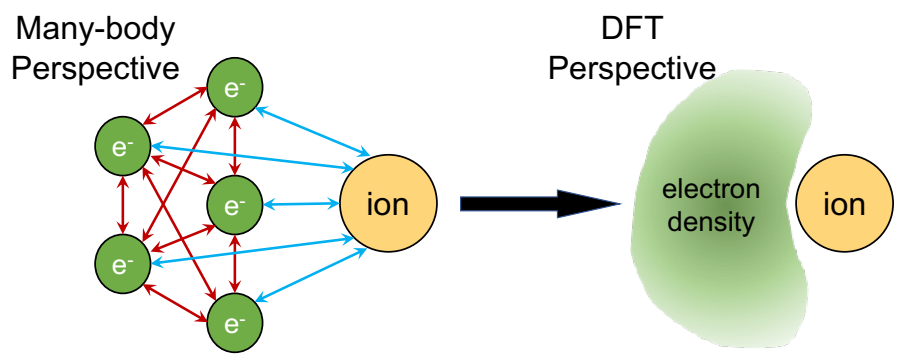

Figure 2-2. The scheme showing the many-body system treated as electron density by DFT.[37]

The electron density n is defined as

$$n(\boldsymbol{r})=2\sum_{i}\psi_i^*(\boldsymbol{r})\psi_i(\boldsymbol{r}), \tag{2-3}$$

where $\psi_i^*(\boldsymbol{r})$ is the probability that an electron in wavefunction $\psi_i(\boldsymbol{r})$ is located at position $\boldsymbol{r}$. According to the Hohenberg and Kohn theorem,[38,33] the energy of the system can be written as $E=E[n(\boldsymbol{r})]$, which is a function of the three Cartesian coordinate $\boldsymbol{r}$,

rather than $3N$ in the full wavefunction in Equation 2-2. The electron density that minimizes the functional $E[n(\boldsymbol{r})]$ is referred to as ground state electron density $n_0(\boldsymbol{r})$. Rewriting the Hamiltonian in Equation 2-2, the Khon-Sham Equation is shown as

$$\left[-\frac{h^2}{2m}\nabla^2 + V(\boldsymbol{r}) + V_H(\boldsymbol{r}) + V_{XC}(\boldsymbol{r})\right]\psi_i(\boldsymbol{r}) = \varepsilon_i\psi_i(\boldsymbol{r}), \tag{2-4}$$

where h is the Plank's constant, m is the electron mass, $V(\boldsymbol{r})$ is the electron-nuclei interaction, $V_H(\boldsymbol{r})$ is the electron-electron exchange interaction (Hartree Potential), $V_{XC}(\boldsymbol{r})$ is the exchange-correlation potential to correct the self-interaction of the electron in the Hartree Potential, $\psi_i(\boldsymbol{r})$ is the electron wavefunction located at position $\boldsymbol{r}$, and ε_i is the ground state energy of the electron. The exchange-correlation potential is the functional derivative of the exchange-correlation energy E_{XC} which can be expressed as

$$V_{XC}(\boldsymbol{r}) = \frac{\delta E_{XC}(\boldsymbol{r})}{\delta n(\boldsymbol{r})}. \tag{2-5}$$

Thus, the total energy is contributed by three parts: the kinetic energy of electrons T_0, the Coulomb repulsion U between electrons and nuclei, the pairs of electrons, and the pairs of nuclei, and the exchange-correlation energy E_{XC}:

$$E_{tot} = T_0 + U + E_{XC}, \tag{2-6}$$

$$T_0 = \frac{h^2}{m}\sum_i \int \psi_i^* \nabla^2 \psi_i d^3r, \tag{2-7}$$

and

$$U = \int V(\boldsymbol{r})n(\boldsymbol{r})d^3r + \frac{e^2}{2}\int\int \frac{n(\boldsymbol{r})n(\boldsymbol{r}')}{|\boldsymbol{r}-\boldsymbol{r}'|}d^3r\, d^3r' + E_{ion}. \tag{2-8}$$

Equation 2-6 can be solved is the exchange-correlation energy functional is exact. However, it remains unknown and can only be approximated.[39] Commonly used forms of exchange-correlation functional are local density approximation (LDA)[40], which uses the local electron density to define the exchange-correlation functional

$$V_{XC}(\boldsymbol{r}) = \boldsymbol{V_{XC}^{electron\ gas}}[n(\boldsymbol{r})], \tag{2-9}$$

and generalized gradient approximation (GGA)[40] in which the exchange-correlation functional is defined as the function of local electron density and local gradient in the electron density

$$V_{XC}(\boldsymbol{r}) = V_{XC}[n(\boldsymbol{r}), \nabla n(\boldsymbol{r})]. \tag{2-10}$$

All density functional theory calculations presented in this dissertation apply the Bayesian error estimation functional with van der Waals (BEEF-vdW) exchange-correlation functional, which is a semilocal approximation with an additional nonlocal correlation term to the finite contribution of LDA and GGA approximation.[41]

In the conversion of a DFT calculation, an initial guess of wavefunction $\psi_i(\boldsymbol{r})$ is used to calculate the electron density $n(\boldsymbol{r})$ using Equation 2-3. With $n(\boldsymbol{r})$, the Kohn-Sham Equation can be solved to give $\psi_i(\boldsymbol{r})$. Equation 2-3 and 2-4 can be interactively solved until the resulting values of $\psi_i(\boldsymbol{r})$ are equal.

All DFT calculations in this dissertation were performed using Vienna *Ab-initio* Simulation Package (VASP).[42,43] The initial guess of electron density is given by the cartesian coordinates and the approximation of elements core provided by pseudopotentials. The self-consistent minimization of the electron density gives the ground state electron density as well as the corresponding ground state energy.

Optimization of the geometry by changing the atomic coordinates gives the relaxed structure that has the minimum DFT energy.

The Nudged Elastic Band (NEB) method is a widely used technique for finding the minimum energy path and locating the transition state between a reactant and a product.[44,45] With the known initial and final states of a reaction, a set of images are created by linear interpolation between the initial and final states. The method works by finding each image the lowest possible energy along the reaction pathway. A spring force is added between each two images to keep equal space with the neighboring images (Figure 2-3). The transition state is located at the saddle point of the reaction pathway and the climbing image algorithm is used to drive the convergence to the transition state.[45] This method works by the climbing up of one image that is closest to the saddle point, which does not feel the spring forces along the band.

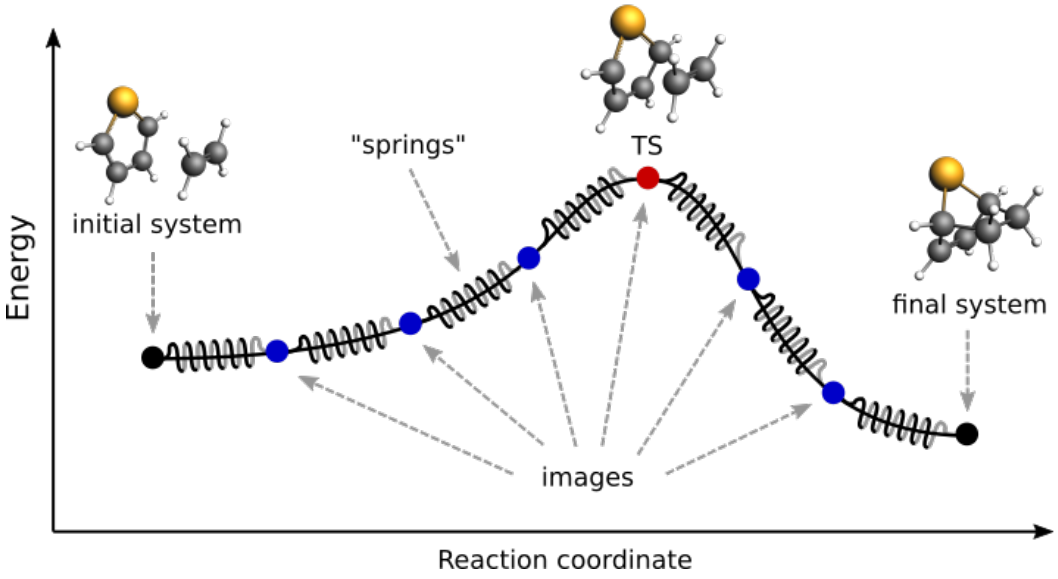

Figure 2-3. The representation of a reaction path computed with NEB.[46]

Though increasing the number of images between initial and final states increases the accuracy for finding the transition states, it also increases the computational cost and memory. Thus, for tough NEB calculations, the dimer method allows the search for saddle point near any initial configurations.[47] With the converging NEB calculations, the dimer calculation can be applied for the image that is closest to the saddle point. An initial guess of the direction can be provided along the dimer and the dimer calculation gives the saddle point near the image. This method is proved to be successful for the transition state calculations in this dissertation, especially the reaction system involving CO_2 and CO_3.

To assure the saddle point located by NEB or dimer calculations is the global transition state, a vibrational analysis needs to be performed and the transition state is confirmed by the existence of only one imaginary frequency.

2.2. Molecular Dynamics

The DFT calculations are limited to 0 K temperature, while the molecular dynamics (MD) take the entropy into account and calculate the kinetics at certain temperature, which predict macro scale properties of materials.[48] MD simulations solve the Newton's equation of motion

$$m_i \frac{d^2 \boldsymbol{x}_i}{dt^2} = \boldsymbol{f}_i, \tag{2-11}$$

where m_i is the particle mass, $\frac{d^2 \boldsymbol{x}_i}{dt^2}$ is the acceleration and $\boldsymbol{f}_i$ is the force, which is calculated by taking the gradient of the potential energy U

$$\boldsymbol{f}_i = -\frac{\partial}{\partial \boldsymbol{x}_i} U. \tag{2-12}$$

For a system with atoms at position $\boldsymbol{x}_i$, the potential energy U can be determined, therefore the force $\boldsymbol{f}_i$. Thus, the position of atoms can be updated by Equation 2-11 with small time steps t. Velocities can be calculated along the simulation. In an MD simulation with constant temperature, volume and number of atoms, the velocities are rescaled to keep constant temperature

$$T(t) = \sum_{i=1}^{N} \frac{m_i v_i^2(t)}{6k_B}. \tag{2-13}$$

The scaling algorithm of velocity is called the thermostat and the most commonly used methods are those developed by Nose-Hoover[49,50] and Andersen[51]. The MD simulation gives a resulting trajectory with respect to time. Other properties, such as potential energy and force can also be abstracted from the MD trajectory, enabling the analyses of properties of the system along the time scale.

The MD simulations that used DFT for the calculation of potential energies are called *ab initio* MD (AIMD). AIMD simulations presented in this dissertation are performed using the open source molecular dynamic package CP2K. [52]

Chapter 3. Mechanistic Investigation of Direct Methane Conversion to Methanol on Ni(111) and NiO(100) Surfaces

3.1. Introduction

Natural gas is one of the most abundant energy resources in U.S. and its production and consumption were projected to continue increasing according to the Annual Energy Outlook 2021.[53] In the chemical industry, natural gas is directly used for heat generation or can be applied as a feedstock to produce higher value products, such as syngas, ammonia, alkenes and alcohols, through catalytic processes.

The main component in natural gas, methane, is thermodynamically very stable. The activation of the strong C-H bonds requires an energy input of ca. 100 kcal/mol, usually associated with reaction temperatures of 900 K and higher. [54] Such high operating temperatures can cause sintering and coking the catalysts, which rapidly decreases the lifetime of the catalysts.[55,56] Another issue that current methane activation processes are facing is that, the heat management of methane combustion, partial oxidation or OCM can be difficult and require expensive building materials for the reactors to tolerate high thermal fluxes. [57] Besides, smaller amounts of methane in shale or stranded gas are expensive to transport and usually get flared. Thus, it its desired to develop processes that can upgrade stranded methane in shale gas reservoirs to higher value products at moderate temperature.

Methanol is synthesized from syngas, a mixture of CO, CO_2 and H_2, which can be obtained from methane steam reforming. Methanol is liquid at atmospheric conditions,

making it much easier to store and transport than methane. Methanol is not only a clean energy carrier, but also an essential feedstock for the production of other high value products. Existing commercialized processes for methanol production from methane involves the formation of syngas

$$CH_4(g) + H_2O(g) \rightarrow CO(g) + 2H_2(g), \qquad \Delta H = 49.3\ kcal, \tag{3-1}$$

$$\text{and } CO(g) + 2H_2(g) \rightarrow CH_3OH(g),\ \Delta H = -21.7\ kcal. \tag{3-2}$$

The overall process is energy consuming because of the endothermic steam reforming step. Moreover, the syngas route is only economical on large scale, and it is not suitable for smaller scale, modular conversion of methane. In contrast, the direct conversion of methane to methanol using oxygen (shown in Equation 3-3) releases heat and is a desirable pathway for the upgrade of stranded methane via

$$CH_4(g) + \frac{1}{2}O_2(g) \rightarrow CH_3OH(g), \qquad \Delta H = -30.7\ kcal. \tag{3-3}$$

One of the challenges this and related partial oxidation processes are facing is the over oxidation of methane to CO or CO_2, which lowers the product yield. Thus, suitable catalysts and processes must be developed to control the delivery of oxygen and maximize the selectivity to partially oxidized products.

Single site catalysts with limited oxygen adsorption potential have garnered interest in recent years. For example, Cu-exchanged zeolites have been investigated for the partial oxidation of methane to methanol and two types of processes were employed: the stepwise[11] and continuous[12] processes. Groothaert and coworkers reported stepwise methane to methanol conversion on Cu-ZSM-5 following a three-step cycle: an O_2-activation step, a methane to methanol reaction step, and a methanol extraction step.[11]

Kulkarni el al. have analyzed a wide range of cation-exchanged zeolites and reported the activities for the methane to methanol reaction.[58] They have theoretically identified the transition state of C-H bond activation as a methyl radical and a linear correlation of the C-H bond activation barrier and the hydrogen affinity. Moreover, Latimer et al. also calculated radical-like transition states and drew the same conclusions regarding the linear correlation between C-H bond activation barriers and hydrogen affinity for a wider range of materials, spanning zeolites, metal oxides, gold surface, gold nanoparticle, graphene nanosheet, etc.[88]

In the step-wise process, water is required to promote the desorption of methanol. Recently, Engedahl and coworkers have performed first-principles study of direct methane to methanol conversion on Cu-dimers in Cu-SSZ-13.[59,60] They have first shown that Z[Cu_2O] and Z[$Cu_2(OH)$] are relevant copper dimer structures.[59] While their micro-kinetic model results indicate that neither of the two sites are active for the reaction under dry conditions. To be able to activate the reaction, a high partial pressure of methane including water is needed.[60] Moreover, Dinh et al. have shown that the dimeric Cu motif as the active site for the continuous partial methane oxidation, with the surface-bound C_1 species as the reaction intermediate of the C-H bond activation.[12]

Alternatively, selective partial oxidation can be achieved by a judicious choice of oxidants, for instance, halogens and H_2O_2. Olah et al. achieved selective catalytic monohalogenation of methane over supported solid acids (e.g., FeO_xCl_y/Al_2O_3, $TaOF_3/Al_2O_3$, and $NbOF_2/Al_2O_3$) and platinum group metals (Pt/Al_2O_3 and $Pd/BaSO_4$) at temperatures between 180 and 250°C.[8] Hammond and colleagues reported that

methane can be oxidized to methanol on iron copper zeolite (Fe-Cu-ZSM-5) with aqueous hydrogen peroxide at 50°C.[61]

Another mechanism to accomplish controlled delivery of oxidants is provided by electrochemical cells. For instance, Mustain and coworkers combined O_2 and CO_2 to generate carbonate (CO_3) ions on the cathode and used the resulting CO_3 as oxidant to convert methane to methanol on the anode.[62,63] The key advantage of Mustain's work is the prevention of methane overoxidation due to the separation of CH_4 and O_2 feeding, as well as the control of CO_3^{2-} delivery by tuning the electrical current.

To gain a mechanistic understanding of the methane to methanol reaction on the anode we performed density functional theory (DFT) calculations of carbonate-assisted activation of methane on Ni(111) and NiO(100) surfaces. We chose Ni(111) as a starting point, because Ni-based catalysts have been widely studied for methane steam reforming and are among the most commonly used catalysts in industry.[64] We then extended our investigation to the NiO(100) surface, which is a better approximation of the NiO/ZrO_2 catalyst used by Mustain. Before discussing the effect of applied electric fields in the electrochemical cell on the energetics of reaction intermediates and transition states in Chapter 4, we first focus on the reaction mechanisms in this chapter.

3.2. Methods

3.2.1. Computational Methods

All periodic density functional theory (DFT) calculations were performed using the Vienna *Ab-initio* Simulation Package (VASP).[42,43] Spin-polarization was turned on for all calculations to describe the ferromagnetism of Ni and anti-ferromagnetism of NiO.[65] A dipole correction was applied in the *z*-direction normal to the surface. Electron

exchange-correlation was described by the BEEF-vdW functional,[41] and the energy cut-off for the plane wave basis set was set to be 540 eV. The partial occupancies for each band were determined by Gaussian smearing with a width of k_bT = 0.1 eV.[66] The self-consistent field cycle was terminated when the change in total energy was lower than 10^{-7} eV and the ionic force convergence criterion was set to below 0.02 eV/Å.

As gas phase reference energies, we used those of CH_4, H_2 and CH_3OH. Calculations of gas phase energies were carried out using the Γ-point only, a dipole correction in all three directions and a decreased smearing width of 0.01 eV. The energy of gas phase O_2 was needed to determine the Hubbard parameter U of NiO(100) surface. It was derived from the gas phase energies of H_2O and H_2, and the experimental data of the heat of formation of H_2O, since standard DFT gives large errors for the energy of the O_2 molecule.[67,68]

Transition metal oxides, such as NiO, experience strong on-site Coulomb repulsion amongst 3d electrons due to the narrow d band width and electron localization. Spin-polarized DFT calculations in the standard generalized gradient approximation (GGA) usually fail to describe these materials correctly. To address this issue, the DFT+U method by Dudarev et al. was applied to the calculations of NiO(100).[69,70] The value of effective Hubbard parameter U_{eff} was fit to 5.4 eV by matching the computational and experimental data for the redox reaction energy of NiO to NiO_2.[70] Our U_{eff} value is in good agreement with prior work, which used U_{eff} values of ca. 6.3 eV.[71,72] The small difference can be attributed to the different exchange correlation functional used here.

The binding energy of an adsorbate was defined as

$$E_{binding} = E_{slab+adsorbate} - \left(E_{slab} + E_{reference\ gas\ phase\ species}\right), \quad (3\text{-}4)$$

where E_i are calculated total electronic energies at each applied electric field.

The activation barrier of each elementary step was calculated by locating transition states using the climbing image nudged elastic band (NEB)[44,45] and the Dimer method.[47] The climbing image NEB algorithm maps the entire minimum energy path, including the saddle point, between the initial and final states by optimizing all intermediate images simultaneously. For difficult pathways the estimated transition state from the NEB calculation can be further refined using the Dimer method, which optimizes only the transition state image and usually results in a lower computational cost. By analyzing the normal modes of vibration of all transition states, we confirmed them as first order saddle points showing a single imaginary frequency along the reaction coordinate. All reported energies and enthalpy of reaction (ΔH) are approximated using electronic energies and neglect zero point energy correction and heat capacity contributions. Vibrational analyses were performed in the harmonic oscillator approximation and a positive and negative displacement of 0.01 Å along all three Cartesian vectors was used to construct the mass-weighted Hessian.

3.2.2. Model Description

3.2.2.1. Ni(111) surface

All models were built using the Atomic Simulation Environment (ASE).[73] The lattice constant (LC) of fcc-nickel was optimized to be 3.477 Å, which is within 1.4% error of with the experimental value (3.524 Å).[74] To investigate the surface catalytic properties, a four-layer Ni(111) slab with $p(3\times3)$ unit cell was built, corresponding to

an adsorbate surface coverage of 1/9 ML. The bottom two layers were fixed to the positions of the bulk phase, while the top two layers were free to relax. A 10 Å vacuum was added within two slabs along the *z*-direction to avoid the interaction between repeated slabs when performing the periodic calculations. This vacuum spacing is comparable to values from the literature (10 Å[75], 11 Å[76] and 12 Å[77]). A Monkhorst-Pack mesh of (4×4×1) *k*-points was used to approximate the Brillouin Zone.[75,77] To describe the ferromagnetism of nickel, we assigned an initial magnetic moment of 0.8 μ_B to each Ni atom, which is ca. 1.2 times that of the experimental magnetic moment of nickel, 0.656 μ_B.[78] The magnetic moment converged to 0.66 μ_B and is in consistent with the experimental data.

3.2.2.2. NiO(100) surface

The optimal LC of NiO was determined to be 4.236 Å, within 0.7% error of the experimental value of 4.264 Å.[79] To select a representative surface model, we considered the low index NiO(100) and NiO(111) surfaces, both of which have been studied experimentally and computationally in the past.[71,72] The surface free energies (γ) of (2×2) unit cells of non-polar NiO(100) and the polar Ni-terminated and O-terminated NiO(111) surfaces were calculated as

$$\gamma = \frac{1}{2A}[e_{slab}N - e_{bulk}N], \tag{3-5}$$

where, A is the area of the surface in the unit cell, e_{slab} is energy per atom in the slab, e_{bulk} is energy per atom in bulk NiO and N is the total number of atoms in a unit cell. We identified NiO(100) as the preferred, low surface energy termination, which is consistent with the calculations done by Yao and coworkers.[80]

Given NiO's anti-ferromagnetic nature, alternating spin directions for neighboring Ni atoms need to be specified. The specification may be a) atom-wise, resembling a checkerboard pattern, b) row-wise, or c) layer-wise. To avoid any magnetic defects in the structure, an even number of repeat units, i.e., rows or layers, is needed. We tested all three possible spin specifications for surface unit cells ranging from (2×2) to (4×4) and the row-wise pattern consistently resulted in the lowest surface free energy. We chose the (3×2) unit cell with a row-wise pattern of spin specification, corresponding to a 1/6 ML coverage of adsorbates, as best compromise between efficiency and accuracy. Similar to the Ni(111) surface, we used a NiO(100) slab with four layers where only the bottom two layers were fixed. A vacuum of 12 Å along the *z*-direction was added between each slab and a Monkhorst-Pack mesh of (8×12×1) *k*-points was used to approximate the Brillouin Zone. The structure of Ni(111) and NiO(100) models are shown in Figure A1.

3.3. Results Discussion

Our mechanistic investigation focuses on the anode reaction, where methane reacts with carbonate ions (CO_3^{2-}) transferred through the electrolyte from the cathode. The overall anode reaction is

$$CH_4 + CO_3^{2-} \rightarrow CH_3OH + CO_2 + 2\ e^-,$$

which we can rewrite in two separate steps as

$$CO_3^{2-} + * \rightarrow CO_3* + 2\ e^-$$

$$CH_4 + CO_3* \rightarrow CH_3OH + CO_2$$

where the asterisk represents a surface site and X* denotes the adsorbed species X. Upon adsorption of the CO_3^{2-} ion to the surface its electrons are transferred and the resulting

surface species is indistinguishable from CO_3* formed from CO_2 and ½ O_2, allowing us to assume a charge neutral reference state in our DFT calculations. This implies that the relevant elementary steps for methane activation and methanol formation can be studied from the reaction $CH_4 + CO_3^* \rightarrow CH_3OH + CO_2$, which assumes that CO_3* exists in pre-adsorbed form on the surface. To examine the role of carbonate in the conversion from methane to methanol we consider two possible reaction mechanisms:

Mechanism 1	Mechanism 2
CO_3-assisted methane activation	O-assisted methane activation
	$CO_3^* + * \rightarrow CO_2^* + O^*$
$CH_4(g) + CO_3^* + * \rightarrow CH_3^* + HCO_3^*$	$CH_4(g) + O^* + * \rightarrow CH_3^* + OH^*$
$HCO_3^* + * \rightarrow OH^* + CO_2^*$	
$CH_3^* + OH^* \rightarrow CH_3OH^* + *$	$CH_3^* + OH^* \rightarrow CH_3OH^* + *$
$CO_2^* \rightarrow CO_2(g) + *$	$CO_2^* \rightarrow CO_2(g) + *$
$CH_3OH^* \rightarrow CH_3OH(g) + *$	$CH_3OH^* \rightarrow CH_3OH(g) + *$

We refer to the above two pathways CO_3- and O-assisted methane activation mechanisms. The difference between the two mechanisms is the role of CO_3. In the CO_3-assisted mechanism, CO_3 activates methane directly, while in the O-assisted mechanism CO_3 serves as a deliverer of an oxygen atom, which assists in the activation of methane. Both mechanisms compete with the direct dissociation of methane, which we also included as reference in our DFT calculations on Ni(111) and NiO(100) surfaces.

3.3.1. Mechanistic Study of Methane conversion to methanol on Ni(111)

3.3.1.1. Binding energies and adsorption geometries

We sampled possible binding geometries of nine surface intermediates on Ni(111). The most favored adsorption geometries and binding energies of the reaction intermediates and corresponding binding energies (eV) are summarized in Figure 3-1.

CH_4 and CO_2 are physisorbed to the surface and other species are chemisorbed. The preferred adsorption site for CH_3, O, OH and H is the fcc site. CO_3 binds to the surface with two of its oxygen atoms in bridge site positions and the third oxygen atom pointing out into the vacuum. HCO_3 has its two oxygen atoms binding to top sites and the OH group pointing away from the surface. CH_3OH binds to the surface through the oxygen atom of its OH group with the CH_3 tail group away from the surface. The calculated adsorption configurations are in agreement with the work previously done by Che,[81] Wang,[82] and Kubicki.[83]

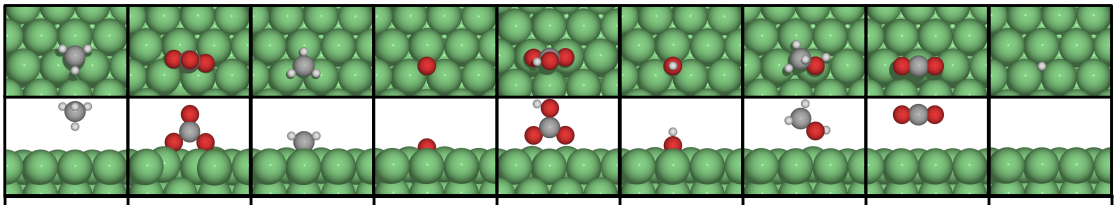

CH_4	CO_3	CH_3	O	HCO_3	OH	CH_3OH	CO_2	H
-0.10	-0.84	0.71	-0.98	-1.49	-1.23	-0.32	-0.68	-0.31

Figure 3-1. Most favored adsorption geometries and binding energies (eV) of the nine possible reaction intermediates on the Ni(111) surface. The green, grey, red and white spheres represent Ni, C, O and H atoms respectively.

3.3.1.2. Potential energy diagram

Figure 3-2 shows the potential energy diagrams with the corresponding activation barriers of reaction mechanisms 1 (CO_3-assisted) and 2 (O-assisted) on the Ni(111) surface. The red and blue curves correspond to the CO_3- and O-assisted mechanisms, respectively, with the grey curve showing the direct methane activation as reference. Black numbers underneath the curves are absolute values indicating the energies of each state, while bold, italic, colored numbers above the curves are relative values showing the activation barriers for each elementary step. The detailed reaction enthalpy and activation barriers for all elementary steps are summarized in Table A1. The

configurations of initial, transition and final states of all elementary steps are summarized in Figure 3-3 with the green, grey, red and white spheres represent Ni, C, O and H atoms respectively, and the * denoting active sites have been omitted for clarity.

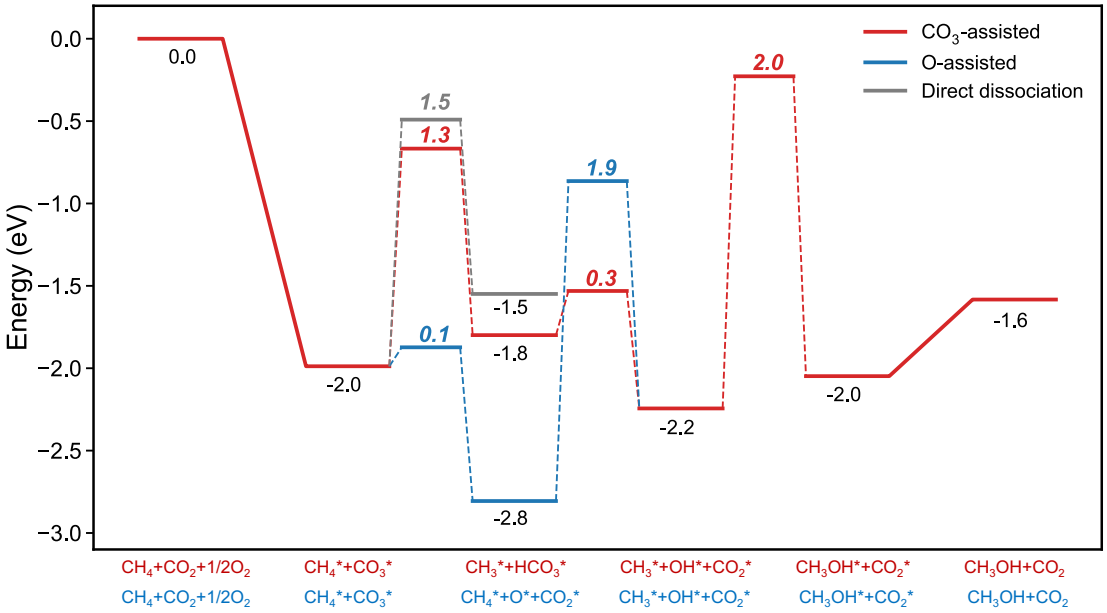

Figure 3-2. Potential energy diagram of both reaction mechanisms on Ni(111). The CO_3- and O-assisted mechanisms are shown as red and blue curves. The direct methane dissociation is shown in grey as a reference.

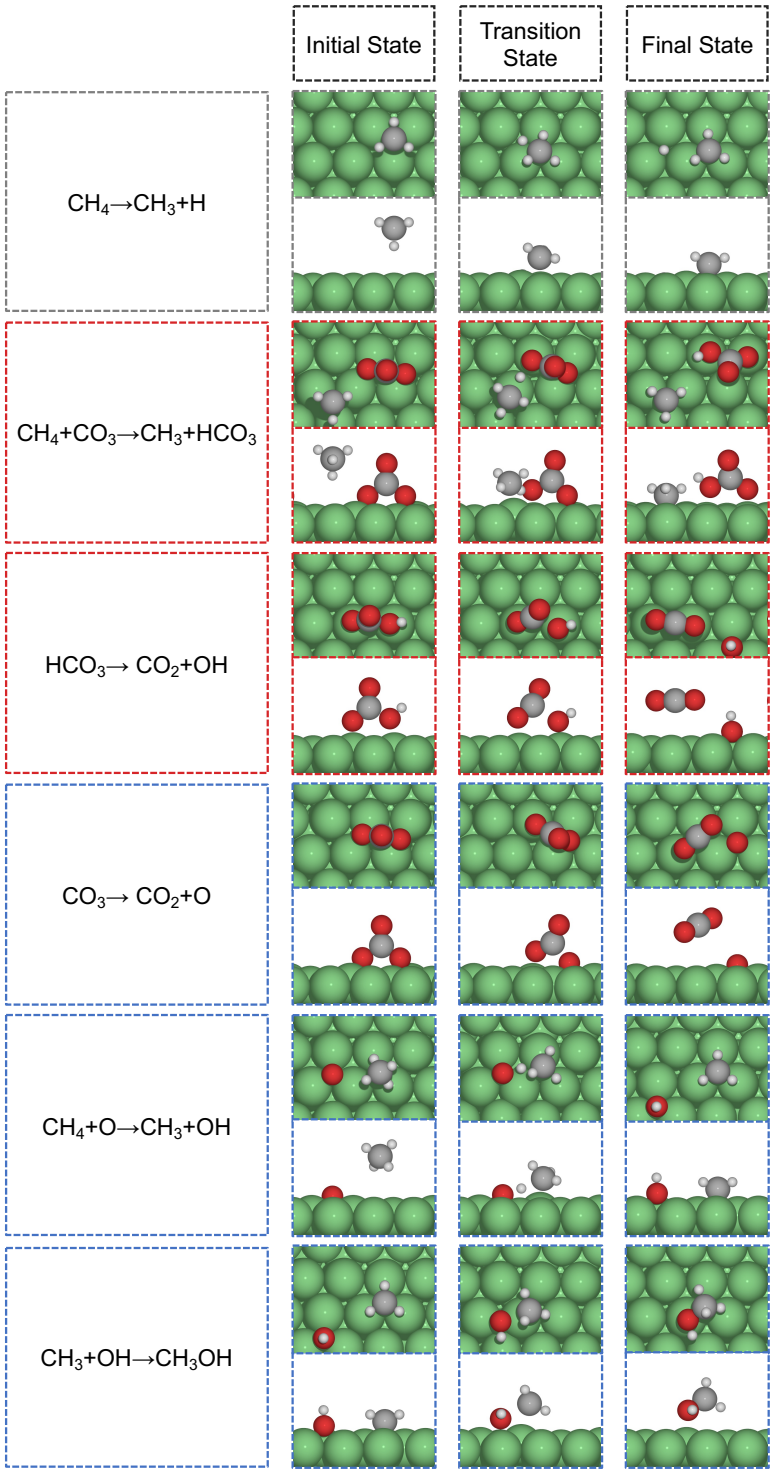

Figure 3-3. Top and side views of initial, transition and final states of elementary steps of direct methane dissociation (grey framed), CO_3-assisted (red framed) and O-assisted (blue framed) methane activation on Ni(111).

In the CO_3-assisted mechanism, a hydrogen atom is transferred from methane to CO_3 with an activation energy barrier of 1.3 eV. The following step of C-O bond cleavage in HCO_3 has a much smaller barrier of 0.3 eV. In the O-assisted mechanism, the C-O bond cleavage in CO_3 has a barrier of only 0.1 eV, but the subsequent O-assisted methane activation step has a large barrier of 1.9 eV. Compared with the reference mechanism of direct methane dissociation on clean Ni(111) requiring a barrier of 1.5 eV, we can conclude that CO_3 can help lower the activation barrier of methane activation, while the presence of O inhibits methane activation. However, the promotion by CO_3 is limited by its competing decomposition to O and CO_2, which is thermodynamically and kinetically more favorable. Regardless of the details of C-H bond activation, both mechanisms have to go through the methanol formation step, which requires an activation barrier of 2.0 eV, the highest value encountered along the potential energy diagram.

Overall, the potential energy diagram for the Ni(111) surface does not suggest any obvious activity towards direct methane conversion to methanol. Instead, methane conversion in Ni is more likely to proceed via traditional mechanisms involving the sequential dehydrogenation of CH_4 and formation of CO_x. Ni is certainly active for methane steam reforming to produce syngas[64] which can be used in the production of methanol over Cu/ZnO[84], Pd/CeO_2[85] or Pd/$ZeAl_2O_4$[86], but these processes are outside the scope of this thesis. Next, we turn our attention to methane activation on NiO(100) in the presence of CO_3.

3.3.2. Mechanistic Study of Methane conversion to methanol on NiO(100)

3.3.2.1. Binding energies and adsorption geometries

The adsorption configurations and corresponding binding energies (eV) of the reaction intermediates on NiO(100) surface are summarized in Figure 3-4. Same as Ni(111), CH_4 and CO_2 are physiosorbed and others are chemisorbed to NiO(100) surface. CH_3, OH and CH_3OH adsorb to the top of nickel atom while H adsorb to oxygen atom. CO_3 and HCO_3 bind to the top of nickel atoms through two oxygen atoms and O adsorbs to the bridge site between two nickel atoms.

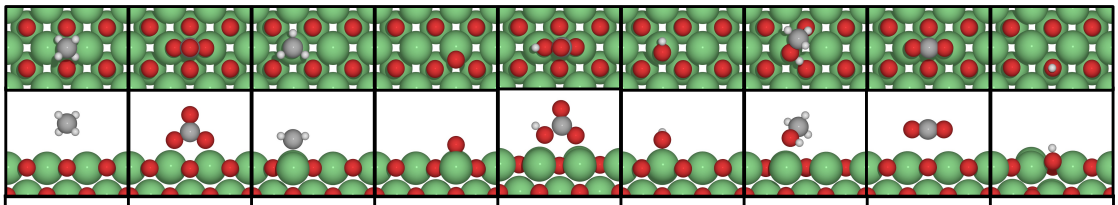

CH_4	CO_3	CH_3	O	HCO_3	OH	CH_3OH	CO_2	H
-0.15	1.05	1.72	2.02	-0.55	0.53	-0.55	-0.78	0.74

Figure 3-4. Most favored adsorption geometries and binding energies (eV) of the nine possible reaction intermediates on the NiO(100) surface. The green, grey, red and white spheres represent Ni, C, O and H atoms respectively.

3.3.2.2. The strong Lewis acid-base interaction

Results show that, the co-adsorbed CH_3 and OH are much more stable than the infinitely separated CH_3 and OH by a 1.7 eV difference. The adsorbate CH_3 prefers to bind to a Ni atom as shown in Figure 3-4 while it tends to bind to an O atom when co-adsorbe with OH. Figure 3-5 shows the Bader charge analysis results of infinitely separated CH_3 and OH, (a) and (b), and the co-adsorbed CH_3 and OH (c). These results show the Bader charge of each atom, which relative difference are indicated in the color

bars. Though the Bader charge does not reflect the real charge of the atom, it gives indication whether an atom is oxidized or reduced. The result shows that the nickel atom is reduced when CH_3 is adsorbed to the surface (Figure 3-5a) and the oxygen atom from OH is oxidized when it is adsorbed (Figure 3-5b). This indicates that the total energies of infinitely separated CH_3 and OH are contributed by two parts, the adsorption of the species and the oxidation state change of nickel or oxygen atom. When CH_3 and OH are co-adsorbed (Figure 3-5c), the paired Lewis acid and base do not cause the oxidation state change of nickel or oxygen atoms, which further stabilize the adsorption of CH_3 and OH. Similar Lewis acid-base interaction between H and OH on TiO_2(110) has been studied and reported by Xiao.[87] To eliminate the contribution of the oxidation state change of atoms to the total energy, it is desired to keep the surface charge neutral. Thus, co-adsorption energies were used to plot the potential energy diagrams instead of the binding energies of infinitely separated adsorbates.

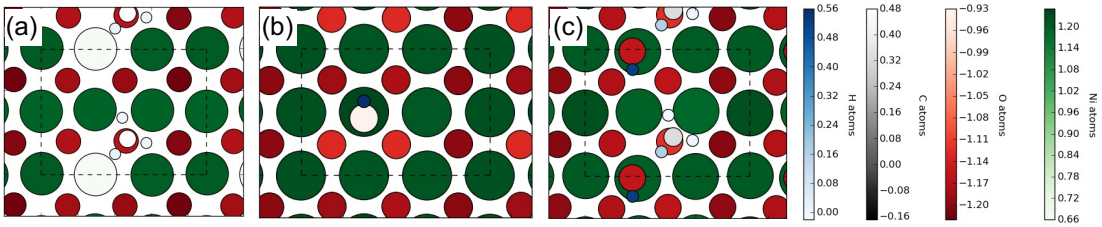

Figure 3-5. Bader charge analysis results of infinitely separated CH_3 (a) and OH (b) and the co-adsorbed CH_3 and OH (c). The color bars show the change of Bader charge for each atom.

3.3.2.3. Radical rebound: a different mechanism for methane-to-methanol conversion

While calculating the activation barrier of O-assisted methane activation, a direct formation of methanol was observed, shown in Figure 3-6. Unlike what happens on the

Ni(111) surface, CH_3 radical forms after the C-H bond is activated by oxygen with a 0.5 eV activation barrier (1 → TS → 2 in Figure 3-6). Latimer and coworkers have reported a linear scaling relationship between the C-H bond activation barrier and the H affinity of the active site for the methane activation via the radical-like transition state.[88] Our results show that the methane is activated by an adsorbed oxygen on NiO(100) surface via the similar transition state, though the resulting C-H bond length (1.3 Å) does not fall in the same range (ca. 2.5 Å) reported by Latimer.

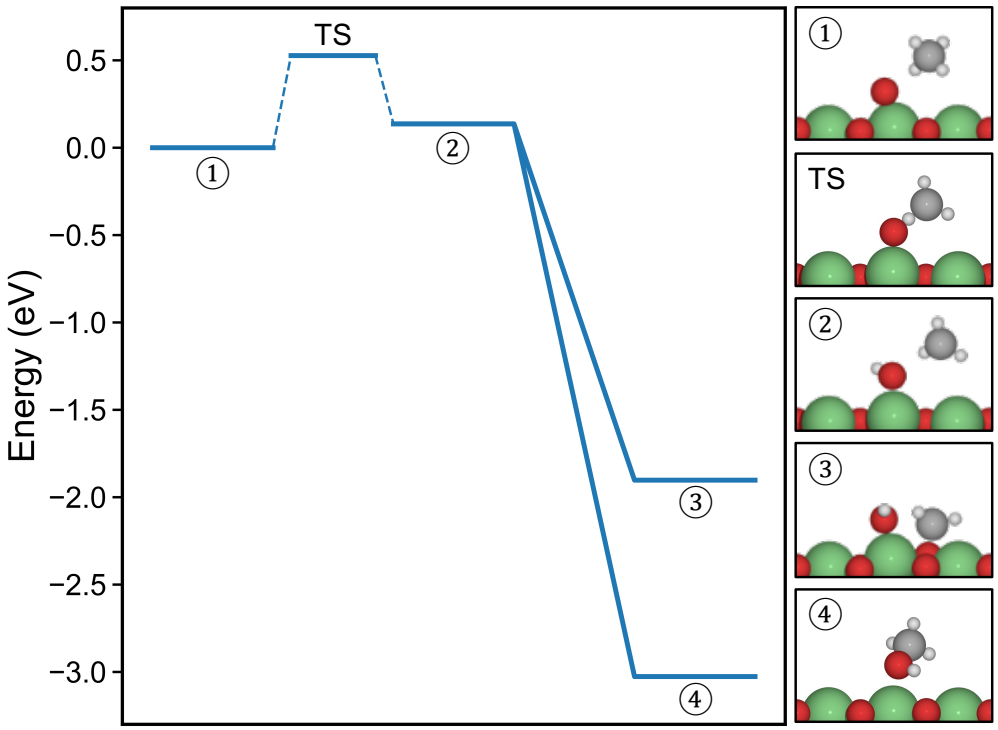

Figure 3-6. O-assisted methane activation (1 → TS → 2) forming a CH_3 radical, followed by CH_3 adsorption (2 → 3) or methanol formation (2 → 4) on NiO(100) surface. Corresponding configurations are shown to the right.

Afterwards, the C-O bond formation between CH_3 radical and OH (2 → 3) has a -3.2 eV enthalpy and the adsorption of CH_3 radical to the surface oxygen (2 → 4) has a -2.0 eV enthalpy. Results show that the CH_3 radical prefers to form methanol

spontaneously with no transition states being identified. Thus, a new mechanism was proposed for the O-assisted methane conversion to methanol:

Mechanism 3

Radical rebound mechanism

$$CO_3^* + * \rightarrow CO_2^* + O^*$$

$$CH_4(g) + O^* + * \rightarrow CH_3(rad) + OH^*$$

$$CH_3(rad) + OH^* \rightarrow CH_3OH^* + *$$

$$CO_2^* \rightarrow CO_2(g) + *$$

$$CH_3OH^* \rightarrow CH_3OH(g) + *$$

where CH_3(rad) represent the CH_3 radical and we name the newly discovered reaction pathway as the radical rebound mechanism. Since the CH_3 radical attaches to the surface OH spontaneously with no transition state identified, we assign a zero barrier for the step of 2 $\rightarrow$ 4 and then studied the CO_3-assisted and radical rebound mechanisms on NiO(100) surface. The reaction pathway mimics the radical rebound mechanism, which is originally discussed in enzymatic, homogeneous C-H functionalization reactions.[89] The mechanism describes the step of H abstraction from R-H, followed by an oxygen rebound step to form R-OH. In addition to homogeneous catalysis, methane oxidation to methanol reactions catalyzed by the mixtures of iron-containing metal-organic framework (MOF) nodes and MFI zeolites have been reported by Simons and co-workers.[90] They have demonstrated the methanol formation via radical rebound mechanism, and the subsequential transport and dehydration steps that are needed to protect the product from overoxidation.

3.3.2.4. Potential energy diagram

The potential energy diagrams with the corresponding activation barriers of CO_3-assisted (red) and radical rebound (blue) mechanisms on NiO(100) surface are shown

in Figure 3-7. The numbers show the absolute energies or relative activation barriers as indicated in Figure 3-2: black numbers underneath the curves are absolute values indicating the energies of each state, while bold, italic, colored numbers above the curves are relative values showing the activation barriers for each elementary step. The detailed reaction enthalpy and activation barriers for all elementary steps are summarized in

Table A2. The configurations of initial, transition and final states of all elementary steps are summarized in Figure 3-8, with the green, grey, red and white spheres represent Ni, C, O and H atoms respectively, and the * denoting active sites have been omitted for clarity. When calculating the transition state of methanol formation from adsorbed OH and CH_3, a second imaginary frequency in a helicopter rotation mode was encountered and we were not able to eliminate it. It was treated as the free rotation. Except for that, other transition states were confirmed to have single imaginary frequencies.

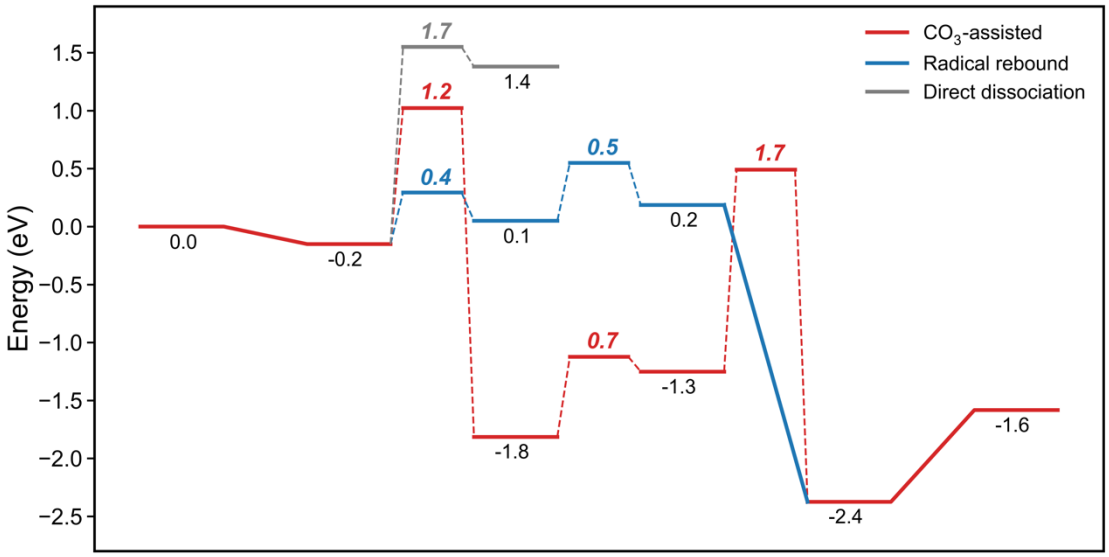

Figure 3-7. Potential energy diagram of CO_3-assisted (red) and radical rebound mechanisms (blue) mechanisms on NiO(100). The direct methane dissociation is shown in grey as a reference

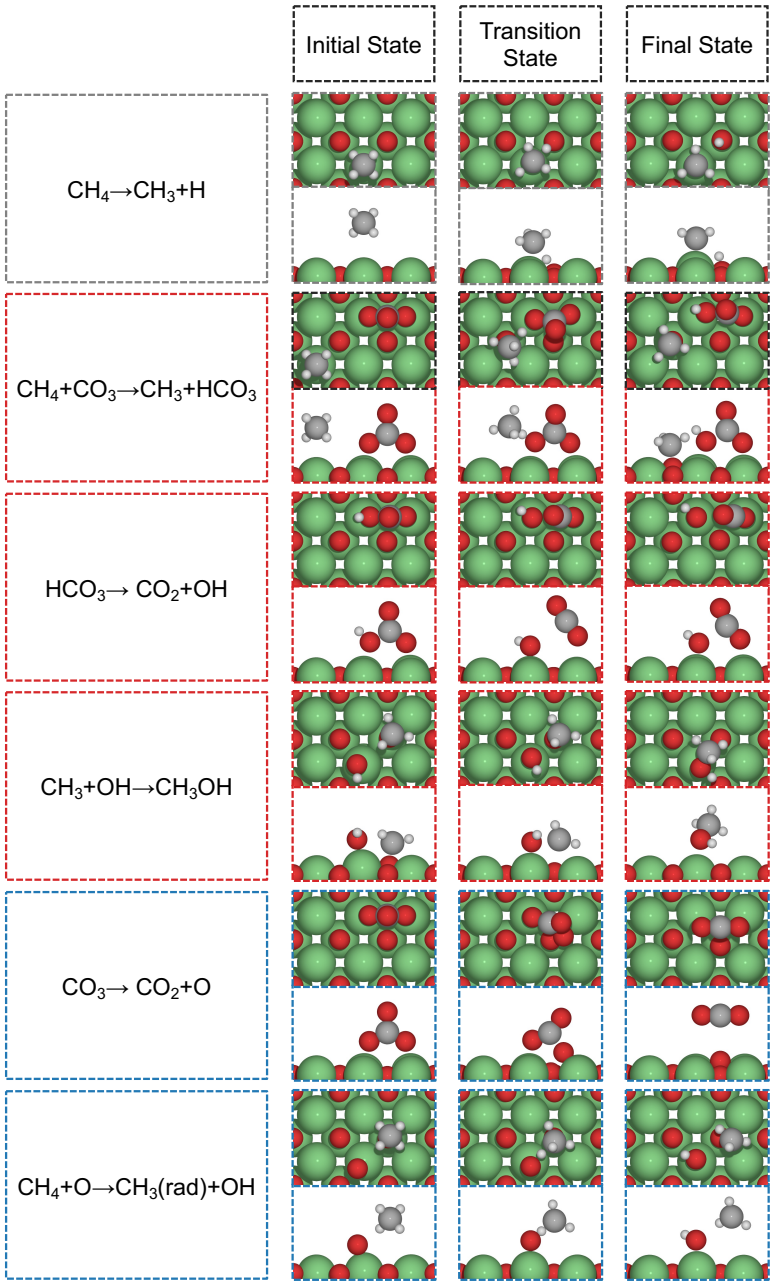

Figure 3-8. Top and side views of initial, transition and final states of elementary steps of direct dissociation (grey framed), CO_3-assisted (red framed) and radical rebound (blue framed) methane conversion to methanol on NiO(100).

Results show that on NiO(100) surface the activation barrier for methane activation by CO_3 is 1.2 eV and that for methane activation by O is 0.5 eV. Both pathways lower the methane activation barriers significantly comparing with direct methane dissociation

with a 1.7 eV barrier. Notably, CO_3 is much easier to dissociate into CO_2 and O (0.4 eV activation barrier) than to activate methane directly. The O formed afterwards is able to abstract H from methane to form OH and CH_3 radical. CH_3 radical then is easily to form C-O bond with OH, without having to go through the energy intensive methanol formation in the CO_3-assisted mechanism (1.7 eV barrier). Thus, the radical rebound mechanism has great chance do dominate over the CO_3-assisted mechanism on NiO(100) surface.

According to the results, the role of CO_3 in Mustain's experiments turns out to be the delivery of oxygen atoms from the cathode to anode.[62,63] In the experiments, the gas phase oxygen was fed to the cathode and methane was fed to the anode so that the over oxidation of methane is prevented.

3.4. Conclusion

The mechanisms of methane activation by both CO_3 and O to produce methanol on Ni(111) and NiO(100) surfaces have been studied using density functional theory calculations. Our results suggest that CO_3 and O do not help with the methane activation on Ni(111), compared with the direct methane dissociation, and the high barrier of the methanol formation step makes the reaction unlike to proceed on the Ni(111) surface. Differently, both CO_3 and O are able to lower the activation barrier for C-H bond breaking on NiO(100), and a radical rebound mechanism has been found. In the newly proposed mechanism, the formed radical-like CH_3 prefers to react with the surface OH instead of adsorb to the NiO(100) surface. The radical rebound mechanism shows great potential to dominate the methane to methanol reaction on NiO(100) surface since the fact that it does not have to go through the energy consuming step of methanol formation

from adsorbed CH_3 and OH. Our work provides an insight to the role of CO_3 for methane conversion to methanol – to deliver oxygen atoms for the activation of methane. The fact that gas phase oxygen and methane are separated is essential to prevent the over oxidation of methane. Future works will be focusing on the effect of applied electric fields on the catalytic behaviors.

Chapter 4. Effect of Applied Electric Field on the Methane-to-Methanol Conversion on NiO(100) and Rate Enhancement under Electrochemical Conditions

4.1. Introduction

As the main component of the natural gas, methane has been widely utilized as fuel to generate heat and power,[91,92] or as a feedstock for the C1 chemical cycle.[93] The activation of the strong C-H bonds of methane requires an energy input of up to 100 kcal/mol or temperatures of 900 K and higher.[54] Such high operating temperatures can cause sintering and coking the catalysts, which rapidly decreases the lifetime of the catalysts,[55,56] Another issue that current methane activation processes are facing is that, the catalysts are placed in expensive alloy tubes to tolerate the high thermal fluxes through the walls of the reactor.[57] Besides, the transportation of gas phase methane is also challenging and expensive. Thus, processes that can upgrade methane to higher value products at moderate temperature are beneficial for the utilization of methane and have been studied both experimentally and theoretically over decades.

Llorca and co-workers have shown the methane selective oxidation to formic acid with an O_2-H_2 mixture catalyzed by plasma-activated gold nanoparticles.[94] Mowbray et al. have performed DFT calculations on the methane partial oxidations and noted an improved adsorbate-surface interaction on the positively charged gold nanoparticles.[95] Sajith and colleagues have performed theoretical study of methane conversion to methanol on Pd and Au/Pd. They have reported that H_2O_2 decomposes to OH groups, which reduce the activation barrier for the hydrogen abstraction significantly.[9]

Psofogiannakis and colleagues have reported the electrooxidation of methane on a Pt(111) and the results show that the C-H bond activation of methane is the rate limiting step.[96]

Electrochemical methane activation at low temperature is emerging as a promising way to upgrade methane to higher value products. Established electrochemical routes rely on the use of solid oxide fuel cells (SOFCs) with nickel or ceria-based anodes.[97,98] However, SOFCs operate at high temperatures at which methane is fully oxidized to CO_2 and H_2O, which are not valuable products. To drive new discoveries at milder conditions, Che et al. performed both computational and experimental studies of methane steam reforming reactions (MSR) on nickel with and without electric field.[76,99] They concluded that a positive applied electric field decreases the rate constant and equilibrium constant of carbon formation on Ni; thus, preventing the formation of coke on the catalyst. Moreover, a positive external electric field lowers the potential energy diagram for MSR steps by strengthening the binding of several reaction intermediates. External electric fields can also alter the most favorable reaction mechanism and vary the rate constants and equilibrium constants of the rate limiting step.[76] For example, a negative electric field has the ability to decrease the activation barrier for the formation of methanol, which makes the catalytic process with an applied electric field a potential way to generate methanol from methane.[99]

We have previously discussed the mechanistic study of methane conversion to methanol on Ni(111) and NiO(100) surfaces according to the experiments reported by Mustain and co-workers[62,63] in Chapter 3. We have shown that the methane conversion to methanol reaction follows different mechanisms on Ni(111) and NiO(100) surfaces.

Instead of forming the surface methyl, a CH_3 radical is formed after methane activation by oxygen on NiO(100). The direct C-O bond formation of OH and CH_3 radical allows the bypass of the methanol formation from surface OH and CH_3. The radical rebound on mechanism reduces the overall activation barrier since the C-O bond formation of surface OH and CH_3 has the highest activation barrier among all elementary steps, which is consistent with Sajith's finding that the recombination of methyl and OH being the rate-determining step for the methanol formation. [9]

The limit of conventional catalytic performance is described by the Sabatier principle: the maximum reaction turnover can be achieved by the catalyst that binds to the reaction intermediate neither too strongly or weakly.[18] The optimal catalyst is ideally located at the peak of the Sabatier volcanoes which balances the rates of adsorption, surface reaction and desorption. Gopeesingh and co-workers have reported that the turnover frequency of formic acid oxidation to carbon dioxide and hydrogen can have a 10-fold increase with a dynamic square wave oscillation between open circuit and positive potential.[20] Shetty et al. have shown that dynamic catalyst stimuli such as light, vibrations, strain and electronic manipulations are able to achieve rate enhancement by accelerating elementary steps independently.[19]

We have continued our previous work on NiO(100) and performed theoretical study of methane oxidation to methanol under external electric fields. Results show that some elementary are promoted by positive electric fields and others by negative electric fields. Gopeesingh and co-workers have reported that the formic acid oxidation reaction to carbon dioxide and hydrogen can be promoted by dynamic oscillation of the applied potential.[20] Our observation of the different response to the applied electric fields shows

that the reaction has great potential to be accelerated under oscillating electrochemical potentials.

4.2. Methods

4.2.1. Computational methods

All periodic density functional theory (DFT) calculations were performed using the Vienna *Ab-initio* Simulation Package (VASP).[42,43] Since the work discussed in this Chapter is a follow up study of the mechanisms investigated in Chapter 3, all computational settings were kept identical.

To investigate the effect of applied electric fields to the reaction, the external electrostatic field was applied in the direction of the dipole correction normal to the surface and controlled via the EFIELD flag in VASP developed by Neugebauer and Scheffler.[100] Following the work of Neugebauer and Scheffler, the implementation inserts a dipole sheet at the center of the vacuum space separating two repeated slabs. The dipole sheet is positively and negatively charged at both ends, respectively, creating a positive or negative electric field. Figure 4-1a,b shows the NiO(100) slab with a negative applied electric field and the electrostatic potential is plotted to Figure 4-1c. The direction of electric field E is defined to be pointing from partially positive to partially negative in the vacuum. The slope of the electrostatic potential in the vacuum is -0.3, assuring that the -0.3 V/Å electric field was applied properly. The unit of this parameter in VASP is eV/Å, which we convert to V/Å for direct comparison with experiments. The units are related by Equation 4-1:

$$1eV/\text{Å} = -1V/\text{Å}. \tag{4-1}$$

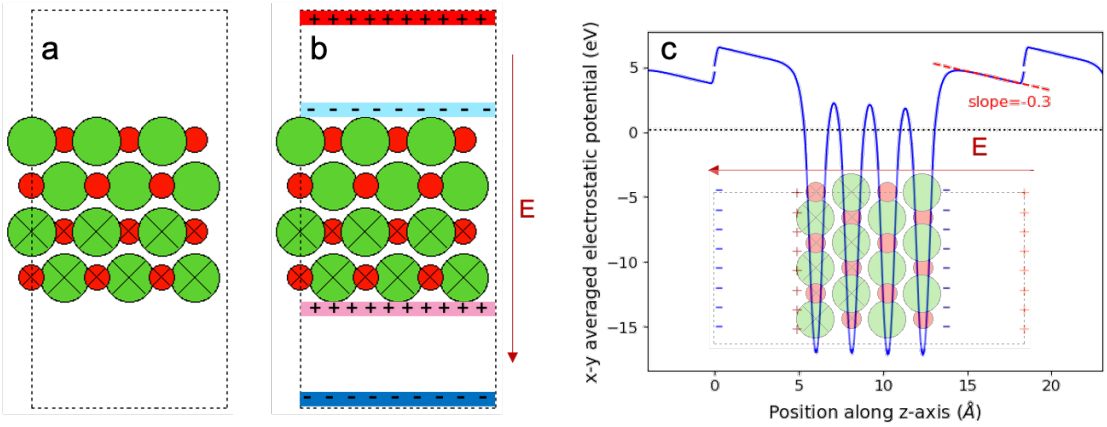

Figure 4-1. Scheme of externally applied electric field. NiO(100) (a) without applied electric field, and (b) with a negative applied electric field. (c) Electrostatic potential diagram of NiO(100) with a -0.3 eV applied electric field.

Charge density difference was calculated by taking the difference between the charge density of the slab with the adsorbate and the charge density of the slab and adsorbate alone. The isosurfaces were plotted using VESTA.[101]

4.2.2. Model Description

All models were built using the Atomic Simulation Environment (ASE).[73] The optimal lattice constant was kept the same as mentioned in Section 3.2, which is 4.236 Å. To keep the consistency, a four-layer (3×2) NiO(100) surface with a row-wise spin specification was used for all the calculations. The bottom two layers were fixed and a vacuum of 12 Å was added between slabs. A Monkhorst-Pack mesh of (8×12×1) *k*-points was used to approximate the Brillouin Zone.

4.3. Results Discussion

4.3.1. Two reaction mechanisms studied for methane conversion to methanol

According to our previous work, two mechanisms were studied: CO_3-assisted methane activation and radical rebound mechanism:

Mechanism 1

CO_3-assisted methane activation

$$CH_4(g) + CO_3^* + * \rightarrow CH_3^* + HCO_3^*$$

$$HCO_3^* + * \rightarrow OH^* + CO_2^*$$

$$CH_3^* + OH^* \rightarrow CH_3OH^* + *$$

$$CO_2^* \rightarrow CO_2(g) + *$$

$$CH_3OH^* \rightarrow CH_3OH(g) + *$$

Mechanism 2

Radical rebound mechanism

$$CO_3^* + * \rightarrow CO_2^* + O^*$$

$$CH_4(g) + O^* + * \rightarrow CH_3(rad) + OH^*$$

$$CH_3(rad) + OH^* \rightarrow CH_3OH^* + *$$

$$CO_2^* \rightarrow CO_2(g) + *$$

$$CH_3OH^* \rightarrow CH_3OH(g) + *$$

The asterisk represents a surface site and X* denotes the adsorbed species X. Carbonate serves differently in the two mechanisms: in the CO_3-assisted methane activation, CO_3 directly abstract a hydrogen atom from methane, while in the radical rebound mechanism, the role of CO_3 is to deliver oxygen atoms from cathode to anode. As discussed in our previous work, the C-O formation between OH and the CH_3 radical formed in the radical rebound mechanism is thermodynamically favored by 3.2 eV. Thus, it is assumed that the activation barrier of methanol formation in the second mechanism is negligible. Both mechanisms were studied under positive and negative electric fields and the results are discussed in the following section.

4.3.2. Effect of applied electric fields on the binding behaviors

The adsorptions of all reaction intermediates were calculated under -0.3, 0, and 0.3 V/Å applied electric fields. The adsorption configurations of reaction intermediates without applied electric fields are summarized in Figure 4-2a, green, grey, red and white spheres represent Ni, C, O and H atoms respectively. The configurations do not vary significantly with applied electric fields; however, this observation may not be universal since the limitation of the applied potential. While the configurations remain similar, the binding energies have different response to the applied electric fields, shown in Figure 4-2c. The adsorptions of HCO_3, CO_3 and OH are stabilized by a negative electric field, while the positive electric field stabilizes the adsorption of CH_3OH, H and O. The binding energies of CH_4, CO_2 and CH_3 do not show a significant response to the varying applied electric fields.

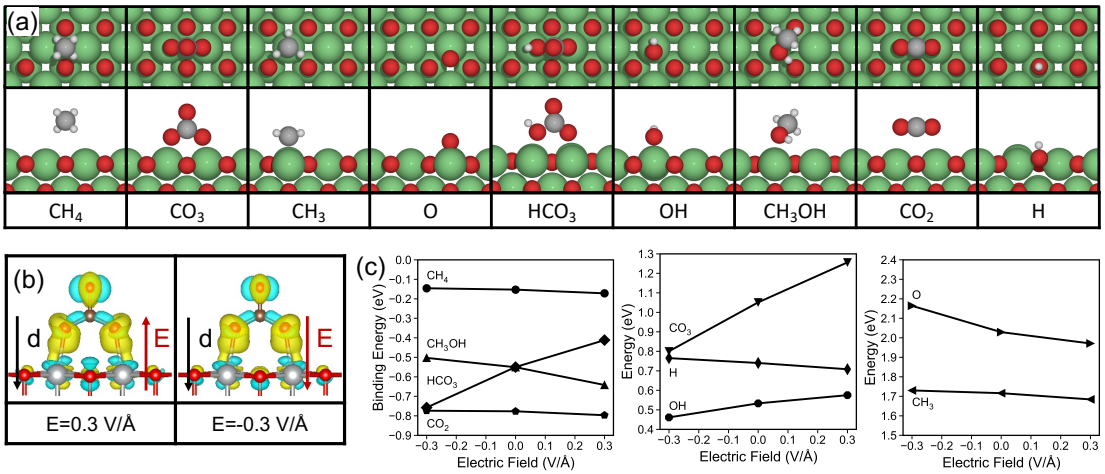

Figure 4-2. (a) Preferred adsorption configurations of reaction intermediates on NiO(100). (b) Charge density difference of adsorbed CO_3. (c) Binding energies of reaction intermediates with respect to the applied electric fields.

To further investigate the relation between applied electric fields and binding energies, we have performed the charge density difference analysis which shows the

charge density difference before and after the intermediates bind to the surface, i.e., the surface dipole moments induced by the adsorptions. Figure 4-2b shows the charge density difference of adsorbed CO_3 on NiO(100) surface at 0.3 and -0.3 V/Å applied electric fields. The yellow and blue isosurfaces indicate the charge accumulation and depletion respectively. The direction of surface dipole is defined to be pointing from partially negative to partially positive at the surface, which is opposite to the definition of direction of electric field. The results indicate that the adsorption of CO_3 induces a surface dipole moment with its positive end pointing to the surface, whose direction and magnitude do not vary significantly according to the applied electric fields. The applied electric fields affect the binding energies by interacting with the surface dipole moment in terms of a Taylor series expansion[102]

$$E_{ad} = E_{ad0} - \Delta d_{E=0} E - \frac{1}{2} \Delta\alpha_{E=0} E^2 + \cdots, \tag{4-2}$$

where E_{ad} is the binding energy, E is the applied electric field, E_{ad0} (binding energy), $\Delta d_{E=0}$ (effective dipole moment), and $\Delta\alpha_{E=0}$ (effective polarizability) are evaluated at $E = 0V/\text{Å}$. Thus, for CO_3 the effective dipole moment has a negative sign, which is consistent with the fact that its adsorption is stabilized by a negative electric field. Overall, the impact of electric field on the binding energies correspond strongly to the magnitude and the direction of their effective dipole moments induced by adsorption.

4.3.3. Potential energy diagrams with applied electric fields

To gain a systematic understanding of the impact of applied electric fields on the methane to methanol reaction, the reaction enthalpy and activation barriers of all elementary steps were calculated, with and without applied electric fields. Figure 4-3

shows the thermodynamic potential energy diagrams of the two reaction mechanisms that we have studied. Reaction enthalpies and activation barriers of all elementary steps are listed in Table 4-1, and the configurations of initial, transition and final states of all elementary steps do not show great changes to the electric fields and are summarized in Figure 4-4, with the green, grey, red and white spheres represent Ni, C, O and H atoms respectively.

The potential energy diagram in Figure 4-3 indicates that the applied electric fields have great impact on both reaction enthalpies and activation barriers. For the CO_3-assisted mechanism, a positive electric field lowers the reaction enthalpies for all three elementary steps. By switching from -0.3 to 0.3 eV electric field, the activation barrier of methanol formation step, which has the highest barrier, is reduced by 0.28 eV. However, the methanol formation is still the most energy consuming step even with positive applied electric field indicating that the CO_3-assisted mechanism is unlikely to proceed comparing with the radical rebound mechanism. For the radical rebound mechanism, both reaction enthalpies and activation barriers shown in Table 4-1 indicate that increasing the applied potential favors the decomposition of CO_3 to CO_2 and O, while it makes the methane activation by O less favored. However, due to the different energy levels of the initial states of the second step, a positive electric field still lowers the overall potential energy surface as shown in Figure 4-3.

According to the potential energy diagram, the radical rebound mechanism is supposed to dominate over the CO_3-assisted mechanism, regardless of the applied electric field that we have applied. A positive electric field promotes most of the elementary steps except for the methane activation by O. However, a positive electric

field is able to lower the overall potential energy surface of the radical rebound mechanism. Since TS5 has the highest energy level in the radical rebound mechanism, the C-H bond activation by O is assumed to be the rate determining step of the reaction.

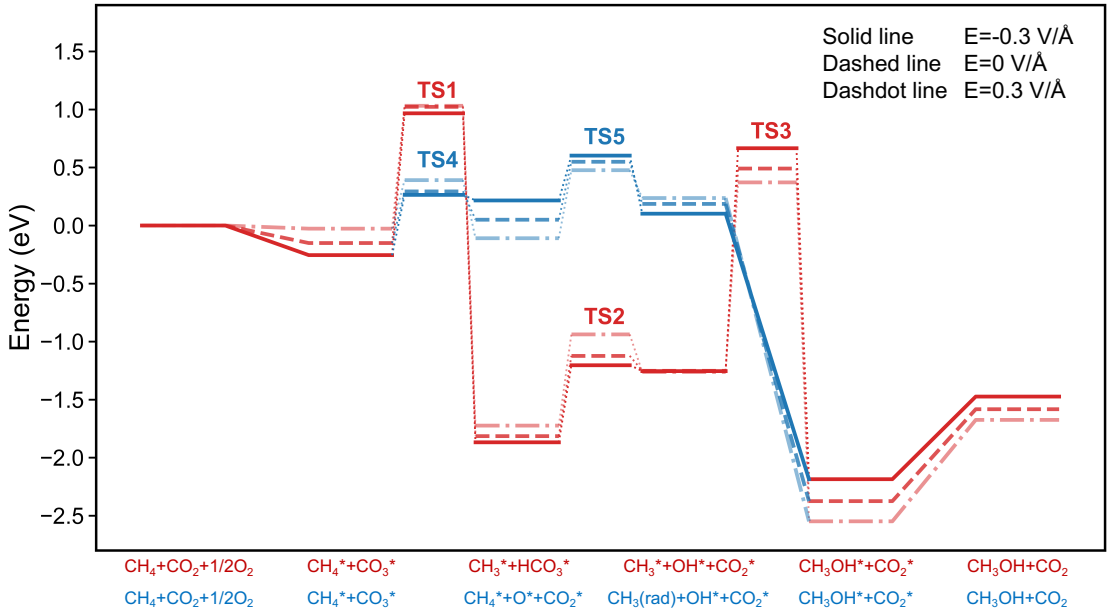

Figure 4-3. Potential energy diagram of CO_3-assisted (red curves) and radical rebound (blue curves) mechanisms. The solid line, dashed line and dashdot line represent -0.3, 0 and 0.3 V/Å applied electric fields respectively.

Table 4-1. Reaction enthalpy ΔH and activation barrier E_a of all elementary steps with -0.3, 0 and 0.3 V/Å applied electric fields. The unit for all values is eV and all species are adsorbed unless CH_3 radical (CH_3(rad)).

Applied Electric Field (V/Å)	Reaction Enthalpy ΔH (eV)			Activation Barrier E_a (eV)		
	-0.3	0	0.3	-0.3	0	0.3
$CH_4+CO_3 \rightarrow CH_3+HCO_3$	-1.61	-1.66	-1.70	1.22	1.17	1.06
$HCO_3 \rightarrow CO_2+OH$	0.61	0.56	0.46	0.66	0.69	0.79
$CH_3+OH \rightarrow CH_3OH$	-0.93	-1.12	-1.29	1.92	1.74	1.64
$CO_3 \rightarrow CO_2+O$	0.47	0.20	-0.08	0.52	0.44	0.42
$CH_4+O \rightarrow CH_3$(rad)$+OH$	-0.23	0.14	0.35	0.23	0.50	0.56

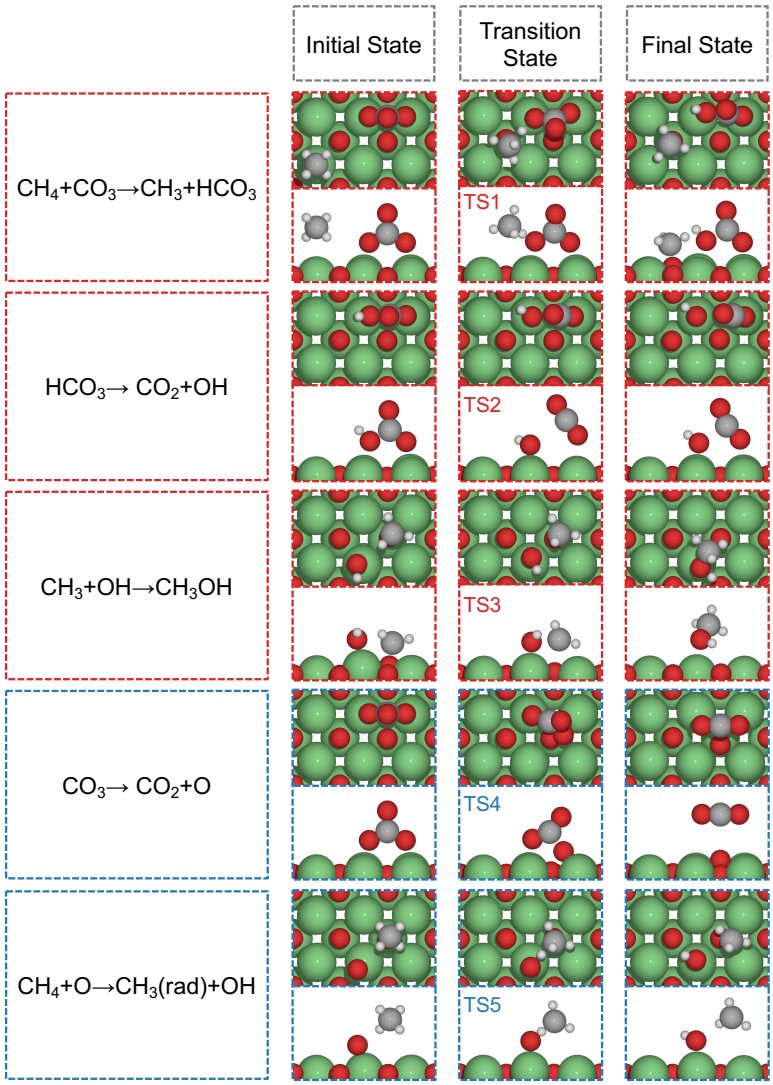

Figure 4-4. Configurations of initial, transition and final states of elementary steps of CO_3-assisted (red framed) and radical rebound (blue framed) mechanisms with the number of transition states as shown in Figure 4-3.

4.3.4. Dynamic rate enhancement using oscillating electrochemical potential

Assuming the C-H bond activation as the rate determining step, a simplified potential energy diagram is plotted as Figure 4-5a, which shows the adsorption of reactants, energy level of the transition state (TS) of C-H bond activation and the desorption of products with -0.3 (blue curve), 0 (black curve) and 0.3 (red curve) V/Å

applied electric fields. According to the potential energy diagram, switching from -0.3 (blue) to 0.3 (red) V/Å reduces the activation barrier E_a by 0.23 eV. According to the Arrhenius Equation

$$\ln k = -\frac{E_a}{RT} + \ln A, \tag{4-3}$$

where k, E_a, R, T and A are rate constant, activation barrier, universal gas constant, temperature and pre-exponential factor. Thus, the rate constants of the reaction under ±0.3 V/Å can be expressed by

$$\ln \frac{k_{0.3V/\text{Å}}}{k_{-0.3V/\text{Å}}} = -\frac{E_{a,0.3V/\text{Å}} - E_{a,-0.3V/\text{Å}}}{RT} \approx 7 \times 10^3. \tag{4-4}$$

Thus, the forward reaction rate is expected to have a ca. 4 orders of magnitude increase by switching the applied potential from -0.3 to 0.3 eV.

On the other hand, the adsorption of reactants is promoted by a negative electric field by 0.23 eV. Also, the negative electric field lower the energy requirement for products desorption by 0.16 eV. Therefore, a negative applied electric field is able to favor the process of product removal and reactants adsorption. Figure 4-5b shows the reaction cycle of the methane to methanol conversion on NiO(100). As we discussed, the rate of forward reaction (CH_4+CO_3→CH_3OH+CO_2) is enhanced by a positive potential, while the refreshment of the surface, i.e., the product removal and reactant adsorption, is favored by a negative potential.

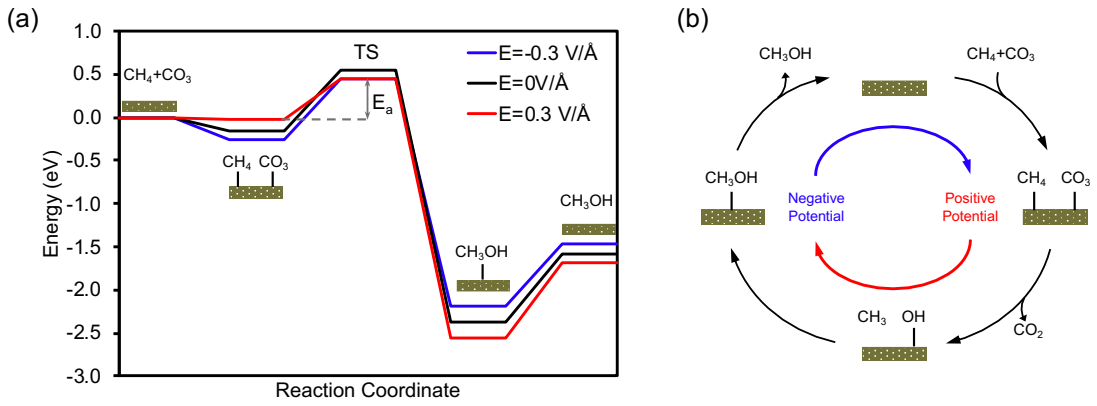

Figure 4-5. (a) Simplified potential energy diagram of methane conversion to methanol via the radical rebound mechanism on NiO(100). (b) Scheme of the methane conversion to methanol reaction cycle.

The fact that the positive and negative promotes different steps in the reaction cycle makes the reaction system capable to be accelerated by applying an oscillating electrochemical potential. Similar process has been discussed by Gopeesingh and co-workers about the electrochemical oxidation of formic acid on Pt.[20] The reaction pathway contains a non-Faradaic formic acid dehydration step and a Faradaic CO electrooxidation step. The dehydration proceeds with open circuit, while the Faradaic CO electrooxidation to CO_2 is accelerated when switching to a high potential. Their experimental results show that, by applying the oscillating potential between open circuit and 0.8 V to the catalyst, the turnover frequency has an approximately ten-fold increase comparing with the turnover frequency under steady potential.

According to our computational results, the methane to methanol conversion via the radical rebound mechanism has great potential to be accelerated by applying similar oscillating potential as Gopeesingh's work.[20] Since the reaction is partially promoted by either positive or negative electric field, an oscillating potential between positive and negative values is expected to be capable to increase the overall reaction turnover.

However, the optimal potential, frequency and time interval of the oscillation still need to be investigated in future work.

4.4. Conclusion

A computational investigation of the effect of applied electric fields to the methane conversion to methanol has been discussed. The electric fields affect the binding behaviors, reaction enthalpies and activation barriers by interacting with the surface dipole moments, which show consistent trend as discussed by Che et al.[102] Two reaction mechanisms have been studied: the CO_3-assisted methane activation and the radical rebound mechanism. Results show that applying positive electric fields is able to lower both reaction enthalpy and activation barriers of CO_3-assisted methane activation. However, the methanol formation step remain energy intensive, making the mechanism unlikely to proceed comparing with the radical rebound mechanism, which contains two steps with activation barriers ca. 0.5 eV. Notably, the positive and negative electric fields were found to promote different steps of the reaction cycle: the positive electric field accelerate the forward reaction, while the catalyst surface is cleaned and retaken by reactants under negative electric field.

Collectively, our work brings attention to the capability of an oscillation between positive and negative potentials to accelerate the methane to methanol reaction dynamically. By optimizing the applied potential and the frequency and time interval of the oscillating potentials, the reaction turnover is expected to be increased significantly. Further investigation of the proposed dynamic rate enhancement is of great interest and potential.

Chapter 5. The Investigation of Carbonate Polymorphism and Its Utility in the Interpretation of Rates of (Non)-Stoichiometric Oxygen Driven Catalytic Cycles

This chapter presents the work done by the collaboration with Xiaohui Zhao advised by Dr.Praveen Bollini and Dr. Jeffrey Rimer. Experiments including the synthesis, characterization and reaction kinetic measurements were done by Xiaohui. Our contribution is limited to the computational perspective, which includes the catalyst modeling, active sites identification, CO_2 vibrational fingerprints, the thermodynamics of the reaction and the proposed reaction cycle.

5.1. Introduction

Oxygen species plays an important role in numerous catalytic oxidations of hydrocarbons by nucleophilic attack of C-C bonds, electrophilic attack of unsaturated C-C bonds, or hydrogen abstraction.[103] Controlling the form of active oxygen opens an opportunity that enables selective catalytic oxidation on solid surface, including alkane partial oxidation,[104] olefin epoxidation,[105] hydroxylation of aromatics, etc . One promising strategy to generate active oxygen is through N_2O oxidation.[106] It has been found that over iron-modified zeolites (Fe-ZSM5), Oα can form over an Fe(II) site following $N_2O + (\ )\alpha \rightarrow O\alpha + N_2$, which exhibits high activity in stoichiometric oxidation of methane and benzene.[107,108] Analogously, O^- has been found active over partially reduced oxide catalysts in the presence of N_2O.[109-111] Lunsford and coworkers

have studied stoichiometric reactions of C_2H_6 with the O^- radical on MgO and MoO_x. Stoichiometric C_2H_6 and O^- ratio of 1 was found for MgO.[110] However, the ratio is higher than unity for MoO_x, which led to speculation that other active oxygen species exist but were undetectable by EPR.[109]

On the other hand, the active oxygen species formed by dioxygen are more complex in nature. Dioxygen adsorption on oxide surface is believed to follow Equation 5-1 by accepting electrons from the surface,[112-114] with

$$O_2 \rightarrow {O_2^-}_{ad} \rightarrow 2{O^-}_{ad} \rightarrow 2{O^{2-}}_{ad} \rightarrow 2O^{2-}_{lattice}. \quad (5\text{-}1)$$

Transition metal oxides including Co_3O_4, Fe_2O_3, CuO, and NiO exhibit complex oxygen profiles during thermal desorption. Depending on the thermodynamic stability of oxygen species, oxygen desorbed at low temperature has been assigned to ${O_2^-}_{ad}$ and ${O^-}_{ad}$, whereas oxygen desorbed at high temperature is assigned to $O^{2-}_{lattice}$. Due to the dearth of concrete identification of active oxygen species, it remains unclear what adsorbed O species are available under reaction conditions and especially which one of them is directly responsible for reaction turnover[115] — these questions are of great experimental difficulties and subject of many studies.

One catalytic system that has drawn attention is the NiO based catalyst for oxidative dehydrogenation of ethane. Lemonidou and coworkers proposed that the selectivity and activity of NiO can be rationalized by the non-stoichiometric oxygen (NSO) intrinsic to the cationic deficient nature of $Ni_{1-x}O$. It is proposed that NSO, presumably in the form of O^-, acts as the active site for ethane oxidation but is unselective to ODH reaction. Increasing Nb loadings systematically decreases the amount of oxygen desorbed during temperature-programmed oxygen desorption (TPD) measurement[116] and the electrical

conductivity of the samples,[117] both being in consistent with decreasing NSO and the associated holes (h) with Nb incorporation. Other high valence dopants exert similar effect by introducing excess electrons to reduce the positive hole concentration and consequently O^-.[118] An alternative interpretation has been provided by associating the catalytic performance with the properties of oxygen, i.e., its mobility or reducibility, which can also be modified by the nature/valence of dopants. Lemonidou and coworkers systematically studied the effect of dopants' valence state on the oxygen mobility with temperature-programmed $^{18}O_2$ isotopic oxygen exchange (TPIE). The presence of low valence cations Li^+ and Mg^{2+} were found to lower the temperature for oxygen exchange proceeding $^{18}O_2+^{16}O_{latt}$à$^{18}O^{16}O+^{18}O_{latt}$. On the other hand, the presence of higher valence cations (Al^{3+}, Ga^{3+}, Ti^{4+}, Nb^{5+}, Ta^{5+}) resulted in higher exchange temperature.[118] This result is in consistent with trend in oxygen binding energy according to DFT calculation by Mushrif and coworkers between stoichiometric NiO and Li-NiO.[119] It is suggested that the lower oxygen binding energy of NiO is favorable for C-H activation but is unfavorable for achieving high ethene selectivity.[120]

To study the role of NSO in the ODH reaction, Xiaohui has previously designed a molten salt route for the preparation of cubic NiO nanoparticles with exposed (100) facets. The cubic particle shape and its faceting does not vary with extended thermal treatment, allowing monotonic reduction in NSO density while maintaining the morphology of the sample.[121] In contrast to the trend observed for doped NiO, a positive correlation between NSO density with ethene selectivity over undoped NiO was observed. Samples after thermal treatment also show lower ethene and CO_2 formation rates per surface area, which implies that NSO may be active for both ODH and total

oxidation reactions.[121] However, the catalytic role of oxygen species remains inconclusive as current characterization techniques including O_2-TPD and H_2-TPR overestimate surface NSO density due to the involvement of bulk oxygen. The inability to exclusively identify and quantify surface oxygen has prohibited us from interpreting the detrimental effect of thermal treatment on catalytic performance over NiO samples.

Herein, we proposed to use CO_2 as a probe molecule and titrant of surface oxygen sites. CO_2 can adsorb on an oxide surface through HOMO-LUMO interaction between the electron-deficient C atom of CO_2 with and the electron-rich O site of a metal oxide.[122 - 124] DFT calculations on MgO(100) and CaO(100) shows that the CO_2 adsorption energy increases with decreasing the coordination number of O^{2-}. The stronger binding of CO_2-O_{3c} was attributed to the higher HOMO state of O_{3c}, which reduced the energy required for charge transfer from O_{3c} to CO_2.[125 - 127] Thus, the chemical environment of surface oxygen may lead to different CO_2 binding.[128-130]

Combining the experiments done by Xiaohui, we assess the properties of two oxygen sites on NiO: lattice oxygen (LO) and non-stoichiometric oxygen (NSO) by comparing the CO_2 adsorption behaviors, including their adsorption geometry, vibrational fingerprint, thermal stability, and reversibility. Together, the study provides a comprehensive interpretation of oxygen site requirement for ethane ODH reaction over NiO based catalyst and a plausible explanation towards the activity and selectivity of oxygen species.

5.2. Experimental Methods

5.2.1. Materials synthesis

Nickel (II) nitrate hexahydrate (Ni $(NO_3)_2 \cdot 6H_2O$, Sigma-Aldrich, ≥97.0%), oxalic acid dihydrate ($H_2C_2O_4 \cdot 2H_2O$, Sigma-Aldrich, ≥99.5%), and niobium (V) oxalate hydrate (Nb $(HC_2O_4)_5 \cdot xH_2O$, Alfa Aesar) were used as purchased.

NiO was prepared using a solid synthesis method. In a typical synthesis, 0.03 mol of Ni $(NO_3)_2 \cdot 6H_2O$ and 0.03 mol of $H_2C_2O_4 \cdot 2H_2O$ were grinded for 10 min using a mortar and pestle until a light blue slurry was formed. The mixture was then dried in the oven for 5 hrs and calcined in the muffle furnace (Nabertherm, LE 6/11) at 450 °C for 1 hr at 2.5 °C / min ramping rate in air. After cooling down to room temperature, the resulted solid was grinded to obtain fine powder of as synthesized NiO, and is referred as NiO. NiO sample that was prepared in the absence of $H_2C_2O_4 \cdot 2H_2O$ is referred as NiO_NT. Cubic NiO sample prepared using a molten salt synthesis route described by previous study[121] is referred as NiO_Cub. Thermal treated NiO samples were prepared by thermal treating the as-synthesized NiO in the muffle furnace at 700 or 1000 °C for 1 hr at 10 °C / min ramping rate in N_2 flow.

5.2.2. CO_2 adsorption

CO_2 adsorption isotherms were measured volumetrically using 3Flex chemisorption instrument (Micromeritics). In a typical measurement, 0.6-2 g samples were loaded in a flow-through sample tube (12 mm, Micromeritics) on a bed of quartz wool (20 mm) topped with a quartz frit. Samples were pretreated at 350 °C for 2 hrs in vacuo ($P < 6.7 \times 10^{-5}$ bar) before each measurement. To measure the amount of reversibly adsorbed

CO_2, two sequential CO_2 adsorption measurements were performed. Between two measurements, the sample was evacuated for 2 hrs to desorb CO_2. CO_2 adsorbed was reported in the unit of mol / mol $_{\text{surface Ni}}$ by taking account of the BET surface area of each sample and surface Ni density of 11.5 atom / nm^2 on (100) facet. CO_2 isotherms were fitted to the adsorption models using MATLAB nonlinear least-squares solver *nlinfit*.

FTIR spectroscopy were measured using a Nicolet 6700 FTIR Spectrometer (Thermo Scientific) with a high-temperature cell (Harrick) with BaF_2 windows (32 mm × 3 mm). Absorbance spectra were collected by a deuterated triglycine sulfate (DTGS) detector by averaging 64 scans. A background was collected at room temperature with 100 sccm N_2 flowing through the empty cell before each run. For as-synthesized NiO, sample wafer (diameter: 13 mm, thickness: 0.8 mm) was prepared by mixing 50 mg sample with 150 mg KBr (previously stored in the oven at 70 °C) and pressing at 1500 psi for 30 seconds. After loading the wafer into the cell, it was pretreated at 350 °C for 2 hrs under N_2 flow to remove surface species then cooled down to designated temperature. A spectrum was collected as baseline before CO_2 is introduced. CO_2 pressure was adjusted by changing the relative flow rate of CO_2/N_2 while keeping the total flow rate 100 cm^3 / min. Before each spectrum was recorded, CO_2/N_2 was equilibrated with the sample for 5 min or until no variation in spectra was observed. Reported spectra were subtracted by the baseline unless stated. A KBr wafer doesn't show any absorbance peak at 1000-1700 cm^{-1} with 10 kPa CO_2. During CO_2 purging experiment, CO_2/N_2 was replaced with pure N_2 flow, and the IR spectra were collected as a function of purging time.

CO_2-TPD profiles were measured with a mass spectrometer (MKS Cirrus 2) connected after a pack-bed reactor. In a typical run, the pelletized sample was loaded and pretreated at 350 °C for 2 hrs in He before cooling to 50 °C. The adsorption of CO_2 was done by introducing 100 kPa CO_2 for 10 mins followed by a 5-hr purging in He. The reactor temperature was ramped up to 700 °C in 10 °C / min. CO_2 desorption rate was monitored by mass spectrometer (m/z=44).

5.2.3. Kinetic measurements

5.2.3.1. Reactor setup

Helium, oxygen, ethane, 400 ppm CO_2/N_2, 10% CO_2/N_2, CO_2 (Matheson, UHP grade) and isotopic $^{13}CO_2$ (Sigma Aldrich, >99% atom ^{13}C) gas cylinders were used as purchased. Gas flows were controlled by mass flow controllers (MKS Instruments, GE50A) with external calibration, and the flow rates were measured with a bubble flow meter each time before reaction. All gas lines were heated above 100 °C with heating tape to avoid condensation.

The reaction setup consisted of two parallel gas lines—a pretreatment line and a reaction line—that could be interchanged using a four-port valve (VICI-Valco, 400 psi). The gas composition of each line was analyzed using a gas chromatograph (GC) (Agilent 7890B) equipped with a GS-CarbonPLOT column (30 m, 0.32 mm, 1.50 μm) whose outlet was split into a flame ionization detector (FID) and a thermal conductivity detector (TCD) with a two-way splitter (Agilent, G3184-60065). Ethane and ethene were quantified using the FID signal, and O_2 and CO_2 were quantified using the TCD (CO formation, if any, stayed below the detection limits of this study). The sample tube was heated using an insulated single-zone furnace (Applied Test Systems, Series 3210)

with a thermocouple (Omega Engineering, KMQXL-062U-15) placed at the top of the catalyst bed. The thermocouple was connected to an integrated temperature controller (Watlow, EZ-Zone PM) to control bed temperature. A pressure transducer (Omega Engineering, PX32B1-050AV) was used to record the pressure above the catalyst bed.

Prior to reaction, catalyst samples were pressed, crushed, and sieved (40–80 mesh). The pellets were then mixed with quartz sand (40–80 mesh, acid washed and calcined at 1000 °C) in a weight ratio ranging between 1:1 and 1:10. Each sample was loaded into a 4 mm inner diameter quartz tube and supported by a quartz frit. The quartz tube was mounted into the center of the furnace; the sample temperatures reported are those at the top of the catalyst bed. The reactor temperature was ramped to the reaction condition at 5 °C / min ramping rate. The reactant feed flow was analyzed by gas chromatography until it reached the target composition. After the feed flow is stabilized, the reactant was introduced to the reactor by switching the four-port valve and reanalyzed. The carbon balance ($\%C$), ethane conversion ($X_{C_2H_6}$), and ethene carbon selectivity ($S_{C_2H_4}$) were calculated using the following equations:

$$\%C = \frac{F_{C_2H_4} + F_{CO_2}/2}{F_{C_2H_6,feed} - F_{C_2H_6}}, \tag{5-2}$$

$$X_{C_2H_6} = \frac{F_{C_2H_4} + F_{CO_2}/2}{F_{C_2H_6,feed}}, \tag{5-3}$$

$$\text{and } S_{C_2H_4} = \frac{F_{C_2H_4}}{F_{C_2H_4} + F_{CO_2}/2}, \tag{5-4}$$

where F_i represents the molar flow rate of each species (ethene, CO_2, and ethane) measured at the reactor outlet, and $F_{C_2H_6,feed}$ represents the molar flow rate of ethane fed to the reactor. The factor of 2 in equations reflects the fact that two CO_2 molecules

are formed from one C_2H_6 molecule. Conversion and selectivity are reported as steady state values. Reaction runs in the absence of catalyst conducted at the corresponding ethane and oxygen residence times at 500 °C exhibited negligible ethane conversions, eliminating the need for blank tube subtractions.

5.2.3.2. ODH reaction with CO_2 cofeed

Reaction conversions were controlled below 1% such that in the absence of CO_2 cofeed, the produced CO_2 did not have prominent inhibition on reaction rates. Steady state ethene formation rates in the presence of 0.5-50 kPa CO_2 were measured by adding CO_2 to the ODH reactant. After the ODH reaction with CO_2 cofeed reached steady state, transient ethene formation rate was measured by replacing CO_2 with helium at time = 0. *In-situ* carbonate density over NSO was calculated with the predicted isotherm on NSO, where the corresponding CO_2 pressure was measured with GC. The effect of CO_2 pressure on total oxidation rate was measured under $^{12}C_2H_6/O_2/^{13}CO_2$ reaction by analyzing $^{12}CO_2$ formation rate using mass spectrometry with m/z = 44.

5.2.4. DFT calculations

5.2.4.1. Computational methods

All periodic density functional theory (DFT) calculations were performed using the Vienna *Ab-initio* Simulation Package (VASP).[42,43] The catalyst that has been studied, NiO, is the same as that discussed in Chapter 4. Thus, the computational settings were kept same. The binding energy of an adsorbate was defined as Equation 3-4.

5.2.4.2. Surface model description

As discussed in Section 3.2.2.2, NiO(100) surface was chosen for the investigation of the NiO catalyst since it has the lowest surface free energy. However, water is one of the products of the ethane ODH reaction. Thus, we have also considered the stability of NiO(100) surface with different H_2O coverage (1/3-, 1/2-, 2/3- and 1-ML) with an assumption of 20 kPa water partial pressure. The resulting phase diagram is shown in Figure A2. The results show that the free energy of H_2O covered surfaces increases with temperature and the dry NiO(100) becomes the most stable surface at 540 K. The water partial pressure is expected to be much lower than 20 kPa under ODH reaction conditions. Thus, we validated the use of dry NiO(100) as the best representation of the catalyst.

5.3. Results Discussion

5.3.1. Challenges in the accurate quantification of surface non-stoichiometric oxygen density

Active oxygen species formed by dioxygen activation on metal oxides is believed to follow Equation 5-1 by accepting electrons from the adsorbent. These oxygen species differ in charge, coordination number, spin number, and bonding energy, which make their detection technically feasible by means of infrared, Raman, and electron spin resonance (ESR) spectroscopy. However, it is challenging to directly study their catalytic roles under reaction conditions due to the short lifetime when interacting with other molecules. Exposing oxides to reactant may change the oxidation state of the catalyst, which leads to steady state oxygen concentration different from those values

measured *ex-situ*. In addition, oxide surface may accommodate multiple oxygen species, which increases the complexity of the interpretation. O_2-TPD is commonly applied to study adsorbed oxygen species over metal oxides. Transition metal oxides such as Co_3O_4, Fe_2O_3, CuO, and NiO exhibit complex oxygen profiles during thermal desorption. Based on the thermodynamic stability of oxygen species, oxygen desorbed at low temperature have been assigned to $O_2^-{}_{ad}$ and $O^-{}_{ad}$, whereas oxygen at high temperature assigned to $O_{lattice}^{2-}$. Yet, it remains questionable whether the oxygen measured are exclusively from the surface. According to our early study, the excess oxygen measured by TPD and H_2-TPR exceeds monolayer coverage on cubic NiO particles, indicating the involvement of bulk oxygen.[121] In Figure 5-1, the surface density of excess oxygen of NiO samples derived from different synthesis protocols are compared, which follows NiO <NiO_NT<NiO_Cub. On the other hand, the amount of excess oxygen per total Ni remains almost constant. Therefore, this trend in surface density of excess oxygen is predominately caused by the decreasing surface area with the increase in particle size. Value that exceeds monolayer coverage implies a greater contribution of oxygen from bulk lattice.

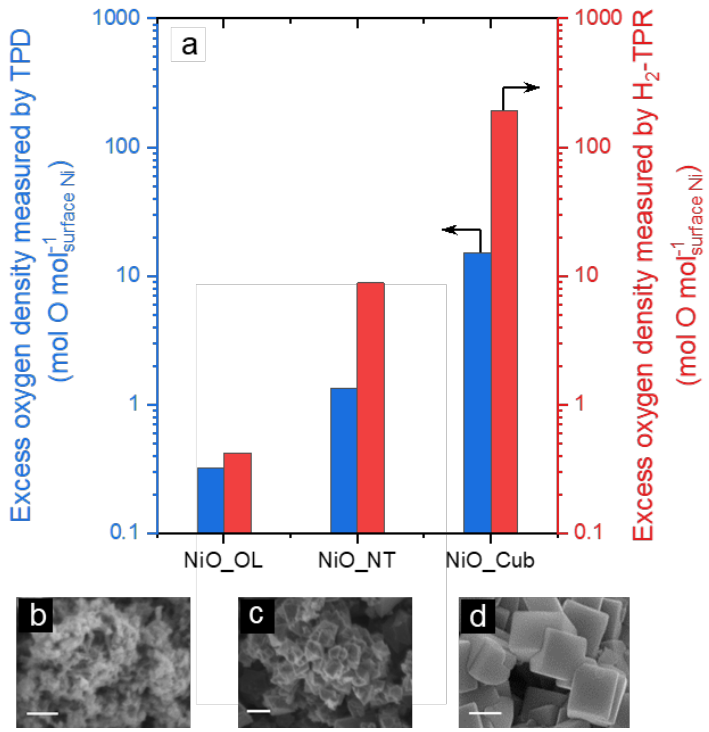

Figure 5-1. (a) Excess oxygen density measured by (left) TPD and (right) H_2-TPR of three NiO samples. SEM images of (b) NiO, (c) NiO_NT, and (d) NiO_Cub. Scale bars = 500 nm.

5.3.2. The nature of CO_2 adsorption onto NiO surfaces

We first evaluated CO_2 adsorption over NiO by measuring the equilibrium adsorption isotherms between 25 and 200 °C. As shown in Figure 5-2a, the isotherms show a two-stage uptake: at low pressure, CO_2 uptake increases immediately up to 0.05 mol mol$^{-1}_{surface\ Ni}$ surface loading, whereas at higher pressure, the uptake increases more gradually. On the other hand, increasing the adsorption temperature has little effect on the initial uptake but drastically decreases the adsorption capacity at higher pressure. To study the interaction between CO_2 and the surface, the adsorption isotherms between 25 and 200 °C were fitted to three adsorption models: Single-site Langmuir model (SSL), Toth model, and Dual-site Langmuir model (DSL). The SSL model assumes that the

adsorbent is a homogeneous surface with all sites being chemically and energetically equivalent.[131] As a modified Langmuir model, the Toth model introduces an additional parameter *n* to describe the inhomogeneity of the absorbent,[132] which is reduced to the SSL when *n*=1. The DSL model assumes Langmuir adsorption occurs collectively over two types of sites, site A and site B, with independent parameters:[133]

$$q \equiv q_A + q_B = \frac{q_{sat,A} b_A P}{1 + b_A P} + \frac{q_{sat,B} b_B P}{1 + b_B P}, \tag{5-5}$$

$$b_A = b_{A0} exp\left(\frac{E_A}{RT}\right), \tag{5-6}$$

$$\text{and } b_B = b_{B0} exp\left(\frac{E_B}{RT}\right), \tag{5-7}$$

where q_{sat}, b, and E are the monolayer adsorption capacity, adsorption parameter, and heat of adsorption of each site.

The SSL or Toth models fail to describe CO_2 uptake which is instant at low pressure and linear at high pressure, while the DSL model can successfully capture this behavior (Figure 5-2a). The fitted parameters for DSL model are summarized in Table 5-1. Plotting the CO_2 isotherm over each site using their individual fitted parameters, distinct adsorption trends were observed between site A and B (Figure 5-3). Compared with site A, which gradually evolves with pressure, the adsorption on site B shows a step change at low pressure and remains almost unchanged at high pressure once it reaches the monolayer capacity. As the increase in CO_2 uptake with pressure $\frac{dq}{dP}$ can be expressed as $q_{sat} * \frac{b}{(1+bp)^2}$ for Langmuir model, which reduced to $q_{sat} * b$ at low pressure and $q_{sat} * \frac{1}{bp^2}$ at high pressure, the greater non-linearity of adsorption on site B can be explained by higher adsorption parameters b_B over b_A at a given temperature (i.e., b_B = 13.4 kPa^{-1} and

$b_A = 1.6*10^{-3}$ kPa^{-1} at 400 K). Based on the predicted model, at 300 °C reaction temperature, CO_2 adsorption on site A becomes almost negligible, while it could adsorb and cover around 90% of site B.

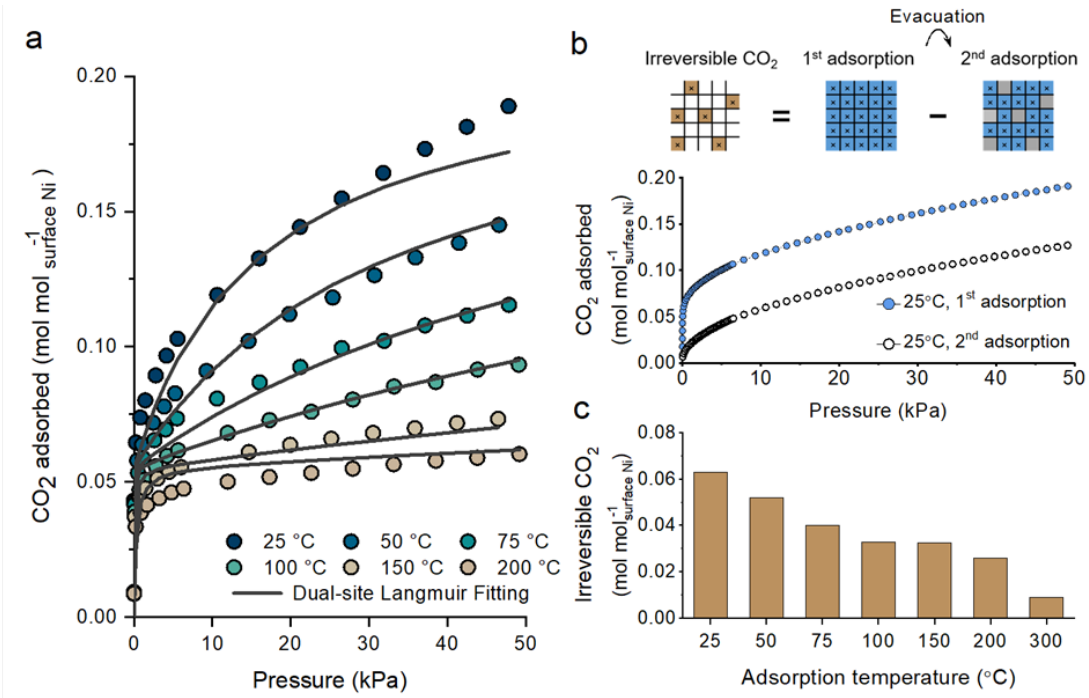

Figure 5-2. (a) CO_2 adsorption isotherms at 25-200 °C (colored dots) fitted with DSL model (solid lines); (b) Two sequential CO_2 adsorptions isotherms with 2-hr evacuation in between. (c) The amount of irreversibly adsorbed CO_2.

Table 5-1. Fitted parameters for Dual-Site Langmuir adsorption model with 95% confidence intervals.

Site A	Site B
$q_{sat,A}$ = 0.220 ± 0.006 mol mol $_{\text{Surface Ni}}^{-1}$	$q_{sat,B}$ = 0.056 ± 0.001 mol mol $_{\text{Surface Ni}}^{-1}$
$b_{A0} \times 10^7$ = 5.76 ± 1.33 kPa^{-1}	$b_{B0} \times 10^5$ = 8 ± 4 kPa^{-1}
E_A = 27.4 ± 0.07 kJ mol^{-1}	E_B = 41.1 ± 0.20 kJ mol^{-1}

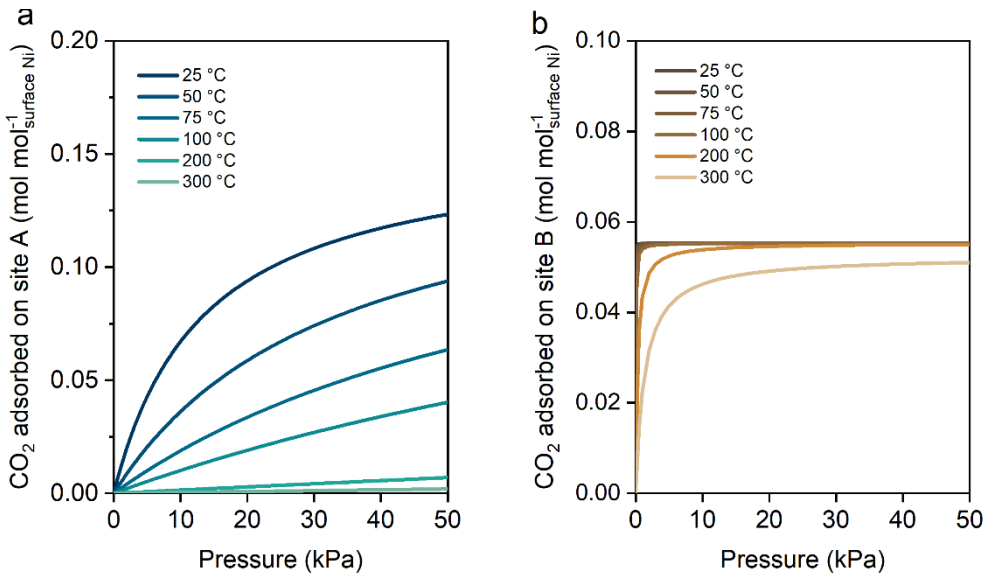

Figure 5-3. Calculated adsorbed CO_2 over (a) site A and (b) site B of NiO using the fitted parameters d8erived from the Dual-site Langmuir model at 25-300 °C.

To confirm the presence of two binding sites, we further compared the reversibility of adsorbed CO_2 with a sequential adsorption separated by a 2-hr evacuation period at 25-300°C (Figure 5-2b, c). Assuming that no irreversibly adsorbed CO_2 desorbs during the surface evacuation, its amount can be estimated as the difference between the first and the second adsorption isotherm (Figure 5-2b). At 25 °C, the reversible and irreversible CO_2 each corresponds to the predicted adsorption on site A and B, suggesting that CO_2 might adsorb reversibly to site A and irreversibly to site B. As temperature increases, a fraction of CO_2 adsorbed to site B starts to desorb, resulting in the adsorption on the decrease of calculated irreversibly adsorbed CO_2 (Figure 5-2c). Thus, the irreversibly adsorbed CO_2 under high temperature does not represent the amount of site B. Overall, the Dual-Site Langmuir model accurately describes equilibrium CO_2 adsorption over NiO. The identity of two adsorption sites will be investigated in next section.

5.3.3. Identification of the two sites for CO_2 adsorption

5.3.3.1. Calculated CO_2 adsorptions and the corresponding vibrational fingerprints

CO_2 adsorption on oxide surfaces forms species such as carbonates, carbonyls, bicarbonates, etc., which give rise to C-O vibrations in the 1000-1600 cm^{-1} range. To assign vibrational frequencies to various possible CO_2 configurations, we use DFT to calculate vibrational fingerprints on realistic surface terminations of NiO(100). To this end, we considered the surface free energy of dry NiO(100) as well as that with 1/3-, 1/2-, 2/3-, and 1-ML H_2O coverage (detailed calculations and results are shown in Appendix). The free energy of H_2O covered surfaces increases with temperature; assuming 20 kPa of water, the most stable NiO coverage shifts from 2/3-ML H_2O covered surface to the dry NiO(100) surface at 540 K. The partial pressure of water under ODH reaction conditions is expected to be lower than 20 kPa, suggesting that the dry NiO(100) surface is the best representation of the catalyst for further investigations of CO_2 adsorption and estimations of C-H bond activation.

Five possible adsorption sites were studied to characterize CO_2 adsorption on NiO(100) (Figure 5-4): (a) stoichiometric NiO(100), (b) NiO(100) with an oxygen adatom bridging two nickel atoms ($NiO+O_{ad}$), (c) NiO(100) with a Ni vacancy ($NiO-Ni_v$), (d) $NiO-Ni_v$ with an oxygen adatom on top of an adjacent nickel atom ($NiO-Ni_v+O_{ad}$), and (e) NiO(100) with an O vacancy ($NiO-O_v$). The Bader charge analyses of these five surface terminations are shown in the bottom row of Figure 5-4, with the red and green spheres represent oxygen and nickel atoms respectively, and the Ni and O

vacancies are indicated as black and red dashed circle. The color scales indicate the Bader charge of oxygen and nickel atoms. The lighter red and lighter green colors relative to NiO represent the oxidized oxygen atoms and the reduced nickel atoms, respectively. The results suggest that surface defects affect the charge distribution across the surface: 1) the oxygen adatom falls close to the lattice oxygen on the stoichiometric NiO (Figure 5-4b) and causes a localized charge deficiency which changes the formal valence of the oxygen adatom and the neighboring lattice oxygen; 2) the formation of a nickel vacancy, i.e., from (a) to (c), creates a charge deficiency distributed across the NiO-Ni_v surface, causing a slight oxidation of all surface oxygen atoms; 3) on NiO-Niv, the oxygen adatoms sits on the top of nickel atom near the nickel vacancy (Figure 5-4d), causing a charge deficiency localized to the oxygen adatom; 4) an oxygen vacancy, i.e., from (a) to (e), results in a charge excess which is localized around the oxygen vacancy, resulting in the partial reduction of surrounding nickel atoms.

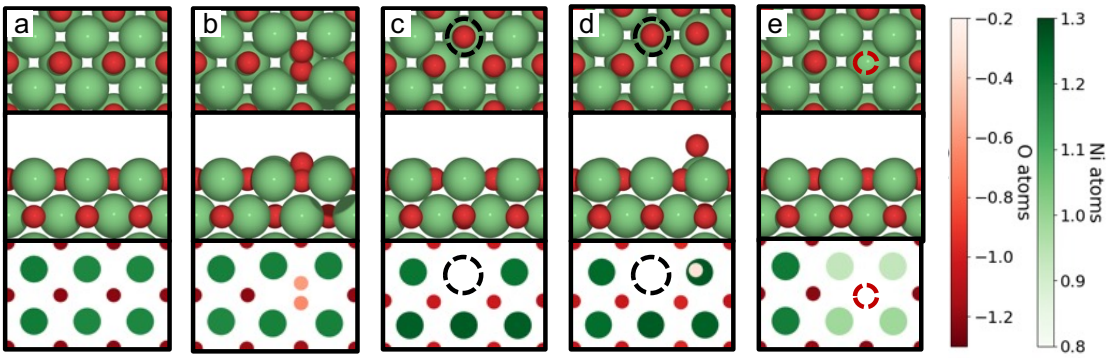

Figure 5-4. The top (first row) and side (second row) views of configurations and corresponding Bader charge analysis (third row) of five NiO surfaces: (a) NiO, (b) NiO+O_{ad}, (c) NiO-Ni_v, (d) NiO-Ni_v+O_{ad}, and (e) NiO-O_v.

The most stable adsorption geometries of CO_2 on these five sites of NiO(100) are shown in Figure 5-5. The corresponding binding energies (ΔE_{ad}) and harmonic vibrational frequencies are summarized in Table 5-2. On the stoichiometric NiO surface,

CO_2 forms a bent structure and binds via its carbon atom with a zero binding energy. The 1679 cm^{-1} vibrational frequency is associated with the asymmetric stretching (ν_{as}) of adsorbed CO_2, while the 1199 cm^{-1} peak corresponds to the symmetric stretching (ν_s). CO_2 has a similar adsorption configuration with the lattice oxygen on the NiO-Ni_v surface, but with a much stronger binding energy of -0.94 eV. The 1610 and 1222 cm^{-1} vibrational frequencies correspond to the asymmetric and symmetric stretching of adsorbed CO_2. On surfaces with O adatoms, CO_2 forms a carbonate (CO_3), and the existence of Ni vacancies lowers the binding energy of CO_2 from -0.44 eV to -1.33 eV. On NiO+O_{ad}, the vibrational frequencies of 1388, 1293, and 1051 cm^{-1} correspond to the asymmetric stretching of carbon and two oxygen atoms attached the surface, asymmetric stretching of CO_3 and symmetric stretching of CO_3, respectively. On NiO-O_v, CO_2 forms a bent structure with one of its C-O bonds filling the O vacancy, which tends to break into a lattice oxygen and adsorbed CO. The 1424 cm^{-1} vibrational frequency corresponds to the stretching of C-O bond involving the top oxygen (O_1), while the 1040 cm^{-1} vibration corresponds to the stretching of C-O bond involving the oxygen that occupies the vacancy (O_2). Our results are consistent with the 'carbonate-like' and the 'carboxylate-like' structures reported by Kumar et al. on Cr_2O_3, with vibrational frequencies in the same range as our calculated values.[134]

According to our calculations, CO_2 binds more strongly with O adatoms than lattice oxygen, regardless of the presence of Ni vacancies. The stronger binding may be attributed to a stronger C-O bond as suggested by the shorter C-O bond length with O_{ad} on NiO+O_{ad} or NiO-Ni_v+O_{ad} (ca. 1.30 Å) compared to the bond length with lattice oxygen on NiO or NiO-Ni_v (ca. 1.50 Å). Moreover, the formation of carbonate forms

an additional O-Ni bond that does not exist when CO_2 binds to a lattice O. The presence of a Ni vacancy can further stabilize the binding of CO_2, with and without O adatoms. We attribute the stronger C-O bond to the increased overlap between the 2*p* states of O and C, as shown in the surface density of states plotted in Figure A3 and Figure A4.

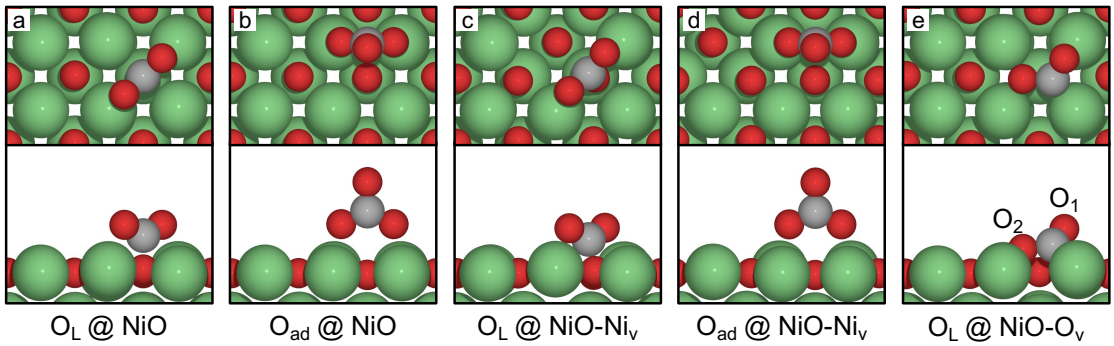

Figure 5-5. Geometries of adsorbed CO_2 on: (a) lattice oxygen, (b) oxygen adatom, on NiO, (c) lattice oxygen, (d) oxygen adatom, on NiO with nickel vacancy, and (e) lattice oxygen on NiO with oxygen vacancy.

Table 5-2. Calculated binding energies (ΔE_{ad}) and vibrational frequencies (cm^{-1}) of CO_2 on NiO(100) surfaces. Values in parentheses provide the closest experimental FTIR frequencies.

Adsorption site	ΔE_{ad} (eV)	Asymmetric (ν_{as})	Symmetric (ν_s)
O_L @ NiO	0.0	1679	1199
O_{ad} @ NiO	-0.44	1388, 1293	1051
O_L @ NiO-Ni_v	-0.94	1610 (1618)	1222 (1211)
O_{ad} @ NiO-Ni_v	-1.33	1410 (1550), 1290 (1314)	1060 (1003)
O_L @ NiO-O_v	-0.58	1424[a], 1040[b]	

[a] $\nu_{C\text{-}O1}$ corresponding to the asymmetric stretching mode between C and top O (O_1)
[b] $\nu_{C\text{-}O2}$ corresponding to the asymmetric stretching mode between C and O in the vacancy (O_2).

5.3.3.2. FTIR results of CO_2 adsorption over NiO

Experimentally, carbonate speciation was probed using *in-situ* FTIR spectra in the presence of gas phase CO_2. NiO sample was pretreated at 350 °C for 2hrs under N_2 prior to CO_2 adsorption to remove the associated surface species.

When 10 kPa CO_2 was exposed to NiO sample at 50 °C, six peaks were observed, which were denoted in Figure 5-6. As temperature increases from 50-300 °C, the set of peaks centered at 1618, 1376, 1211 cm^{-1} (black triangles) gradually decrease and concurrently disappear above 200 °C. The other set of peaks centered at 1550, 1314, 1003 cm^{-1} (violet spheres) also decrease but remain above 200 °C. Two sets of peaks which evolve differently with temperature suggest that they belong to two CO_2 species. The set of peaks with absorbance at 1618 and 1211 cm^{-1} correspond well with C-O asymmetric stretching (1610 cm^{-1}) and symmetric stretching (1222 cm^{-1}) predicted for the bent O-C-O structure formed over O_L @ NiO_Ni_v (Table 5-2). The other set of peaks with absorbance at 1314 and 1003 cm^{-1} match with asymmetric and symmetric C-O bond stretching predicted for the carbonate formed over O_{ad} @ NiO_Ni_v. Following this assignment, the two species formed by CO_2 adsorption each belongs to the chemisorbed CO_2 over lattice oxygen site and bridging carbonate over oxygen adatom, most likely in the presence of Ni vacancies. The observation that the carbonate species being more stable at high temperature than chemisorbed CO_2 is self-explanatory and can be further supported by the DFT results that CO_2 bind more strongly to O_{ad} @ NiO_Ni_v (-1.33 eV) than to O_L @ NiO_Ni_v (-0.94 eV).

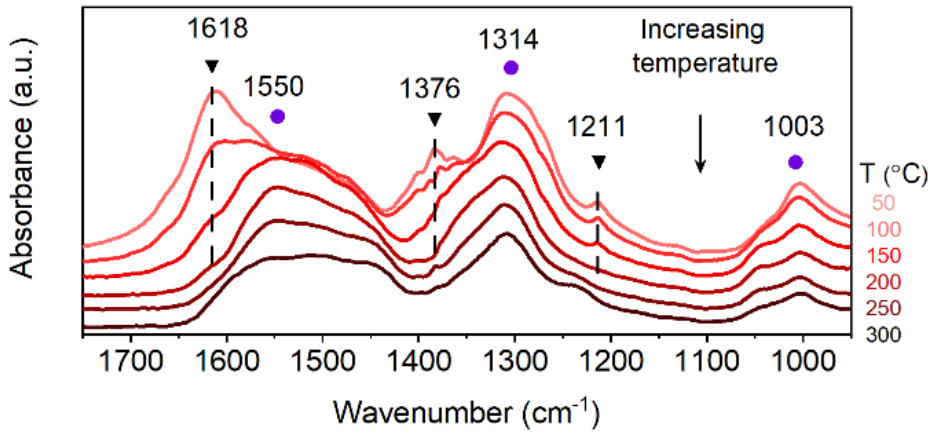

Figure 5-6. FTIR spectra of NiO with 10 kPa CO_2 at 50-300 °C. The dashed lines are for guidance of the disappearance of peaks labeled by the black triangle.

We further characterized CO_2 adsorption on two sites with increasing CO_2 pressure (Figure 5-7). At 50 °C, the peak(s) area corresponds to lattice oxygen-derived CO_2 species (1618, 1376, 1211 cm^{-1}) increase more linearly with pressure than that corresponds to oxygen adatom-derived ones (1550, 1314, 1003 cm^{-1}). At 200 °C, lattice oxygen-derived CO_2 species become imperceptible even at elevated pressure; on the other hand, oxygen adatom-derived carbonate is evident, whose increment with pressure becomes more linear than it is at 50 °C. The response of CO_2 adsorption on lattice oxygen and oxygen adatom to pressure and temperature characterized by FTIR each follows the predicted isotherms over site A and site B (Figure 5-3).

Collectively, we assigned the binding sites as lattice oxygen and NSO site. At low temperature, both lattice oxygen and NSO are responsible for CO_2 adsorption: CO_2 coverage on lattice oxygen increases with pressure while CO_2 saturates over NSO site even at low pressure due to its higher binding energy and adsorption parameter. The adsorption capacity of lattice oxygen decreases with increasing temperature and

becomes negligible at 300 °C that is relevant to ethane oxidation reaction. On the other hand, the adsorption capacity of NSO only decreases slightly from its monolayer coverage, which make it the only adsorption site for CO_2 at 300 °C.

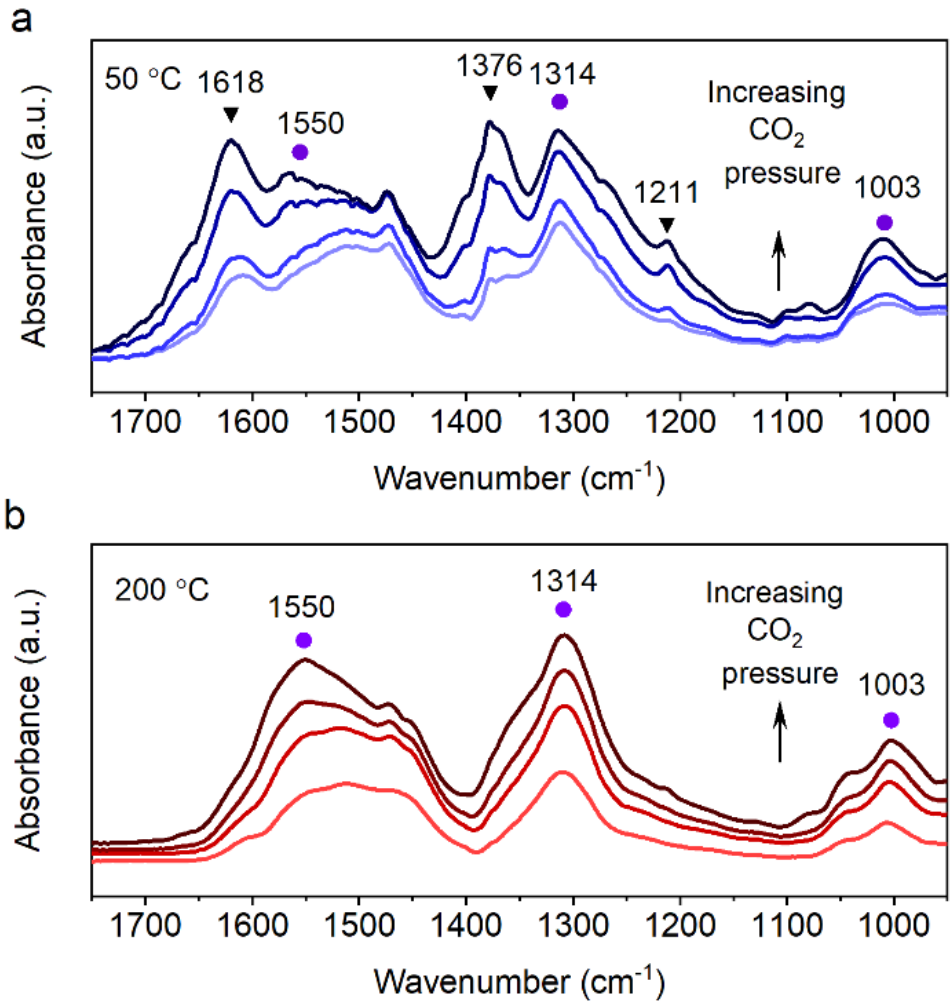

Figure 5-7. FTIR spectra of NiO with 2 to 100 kPa CO_2 at (a) 50 °C and (b) 200 °C. Sets of peaks corresponding to adsorption onto lattice and oxygen adatoms are identified using black triangles and violet spheres, respectively.

Oxygen non-stoichiometry of metal oxides is closely related to the presence of cationic vacancies or constituent cations with mixed valency. The equilibrium oxygen-content increases with oxygen chemical potential, and is in general found to be lower at higher temperature under a fixed oxygen partial pressure.[135,136] For pure NiO, non-

stoichiometric oxygen measured by O_2 desorption in vacuo [137] or thermal desorption[121, 138] monotonically decreases with increasing temperature at which the sample is prepared. The effect of temperature on non-stoichiometry of metal oxide is also reflected by its change in color.[139-141] In our previous study, we have found that NiO samples calcined at 400-1000 °C showed a color change from black to greenish-yellow corresponding to a gradually lowered absorbance within the 500–600 nm visible spectrum according to UV-vis spectroscopy. [121] Together, the results confirm that NSO density on NiO decreases with increasing annealing temperature. To test if NSO density characterized by CO_2 adsorption follows similar trend with increasing temperature, we further compared FTIR spectra of CO_2 over as-synthesized NiO and NiO samples after thermal treatment at 700 and 1000 °C (NiO_{700} and NiO_{1000}). Considering the difference in BET surface area of NiO samples after thermal treatment, the measured IR absorbance of each sample is normalized by sample surface area loaded in the cell and reported on the y axis (Figure 5-8). For better visualization, the spectra are further deconvoluted into peaks attributed to CO_2 adsorbed on lattice oxygen (~1618, 1376 cm^{-1}) and NSO (~1550, 1314 cm^{-1}). Compared to CO_2 adsorbed on lattice oxygen (grey peaks) which remains relatively constant with thermal treatment, CO_2 adsorbed on NSO (grey peaks) decreases significantly over NiO_{700} and becomes negligible over NiO_{1000}. This observation is in qualitative agreement with TPD, H_2-TPD, and UV-vis characterization that we performed earlier, revealing a close to stoichiometric composition after thermally treating NiO at 1000 °C. [121]

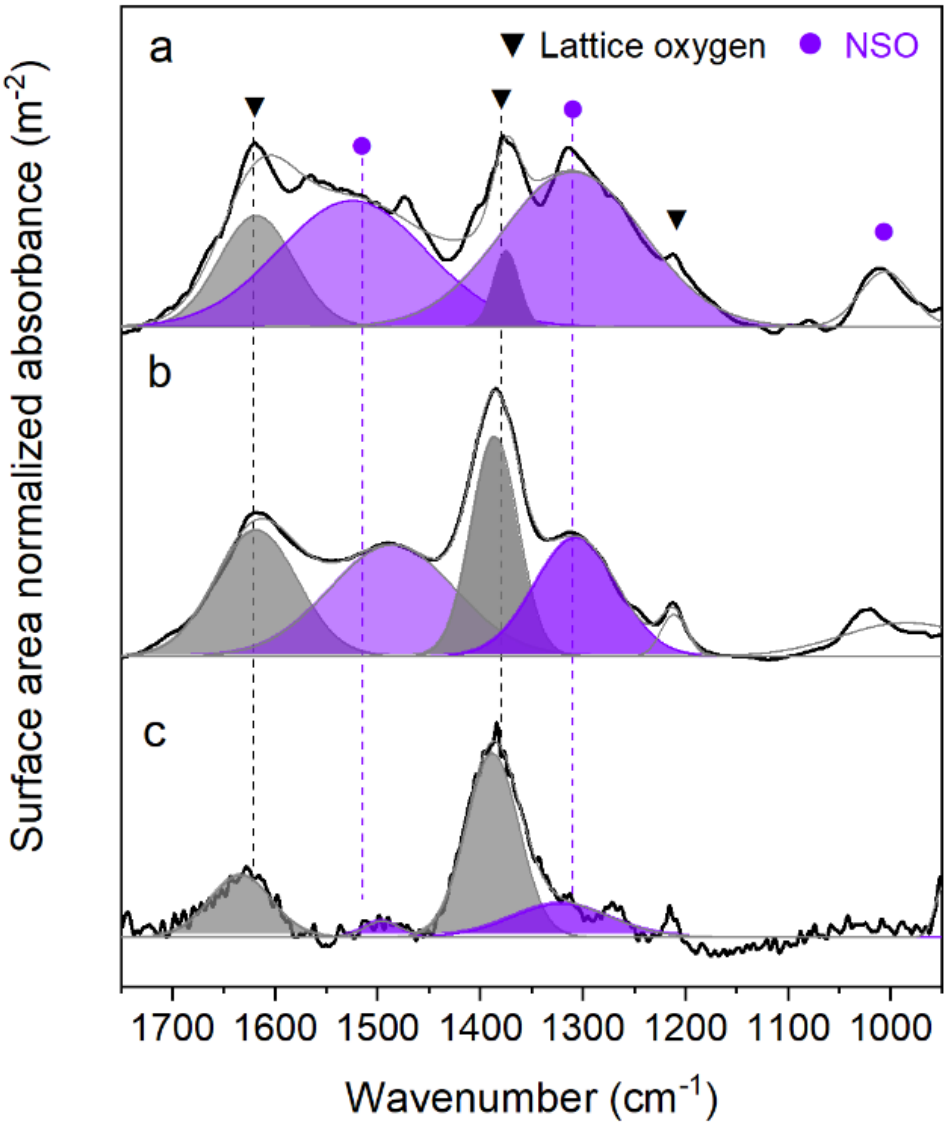

Figure 5-8. Deconvoluted FTIR spectra of CO_2 adsorption on (a) as-synthesized NiO, (b) NiO700, and (c) NiO1000 at 50 °C. Absorbance for each sample is normalized by the total surface area of sample loaded in the FTIR pellet.

5.3.3.3. Irreversible CO_2 adsorption enabling quantification of extra-lattice oxygen

The reversibility of CO_2 adsorptions on two sites was studied using FTIR by comparing the spectra before and after purging CO_2 (Figure 5-9). At 50 °C, adsorbed

CO_2 over lattice oxygen (1618, 1376, and 1211 cm^{-1}) quickly desorbs once gaseous CO_2 is removed, which is consistent with the result reported by Ueno and coworkers, who measured the decrease in absorbance of peak 1383 cm^{-1} vs purging time *t*.[142] In comparison, carbonate formed over NSO remains almost intact even after 15 hrs purging. The results confirm our interpretation in section 5.3.2 regarding the distinct reversibility of CO_2 adsorptions on two sites at low temperature. Desorption of CO_2 becomes favorable as temperature increases, such that at 200 °C, most CO_2 desorbs from NSO after purging (Figure 5-9b). Combining current results and the irreversible carbonate quantified in Figure 5-2c, we infer that below 50 °C, irreversible CO_2 is solely originated from NSO, while reversible CO_2 is solely originated from lattice oxygen. It further implies that CO_2-TPD which measures the desorption of irreversible CO_2 under increasing temperature could provide an approximation of surface NSO density. CO_2 desorption profiles of NiO samples are shown in Figure 5-10. A broad desorption peak at 50-250 °C was observed for all samples, which coincides with the expected desorption temperature of irreversible carbonate. The amount of CO_2 desorbed as integrated peak area is 0.081 mol CO_2 mol $_{\text{surface Ni}}^{-1}$ for NiO, which is close to 0.067 mol CO_2 mol $_{\text{surface Ni}}^{-1}$ of the irreversibly adsorbed CO_2 determined by CO_2 chemisorption. As summarized in Table 5-3, CO_2 desorption decreases for thermally treated NiO samples, which is consistent with the trend in NSO density characterized by volumetric CO_2 adsorption and FTIR spectra of NSO (Figure 5-8).

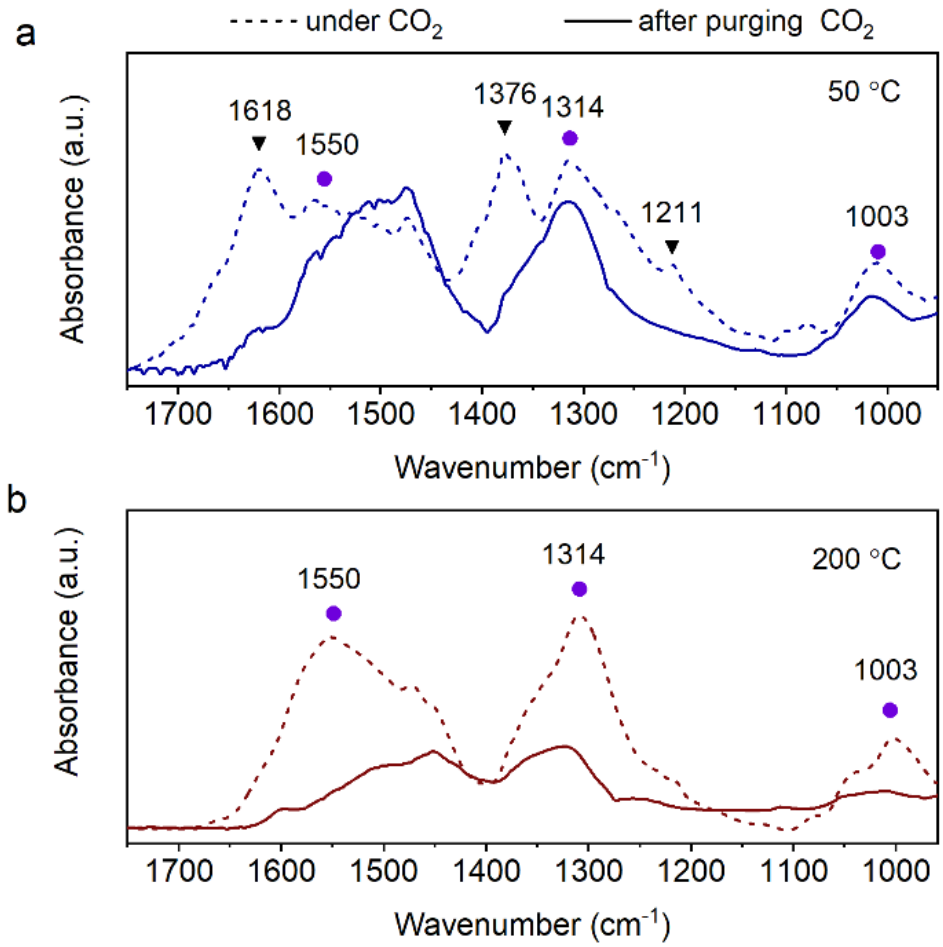

Figure 5-9. FTIR spectra of NiO with (dashed line)100 kPa CO_2 and (solid line) after 15 hrs purging in inert flow at (a) 50 °C and (b) 200 °C.

Table 5-3. Lattice oxygen and non-stoichiometric oxygen densities quantified by CO_2 adsorption/desorption.

	Surface area (m^2/g)	Lattice oxygen (mol mol $_{surface\ Ni}^{-1}$)[a]	Non-stoichiometric oxygen (mol mol $_{surface\ Ni}^{-1}$)	
			CO_2 chemisorption[b]	CO_2-TPD[c]
NiO	48	0.226	0.067	0.081
NiO_{700}	6.2	0.32	0.044	0.070
NiO_{1000}	1.1	n.a.*	n.a.*	0.015

a. Calculated saturation capacity of site A with DSL model.
b. The amount of irreversible carbonate measured during two sequential adsorptions at 25 °C; c. CO_2 desorption peak at 50-300 °C during CO_2-TPD.
* Adsorbed CO_2 is below the detection limit.

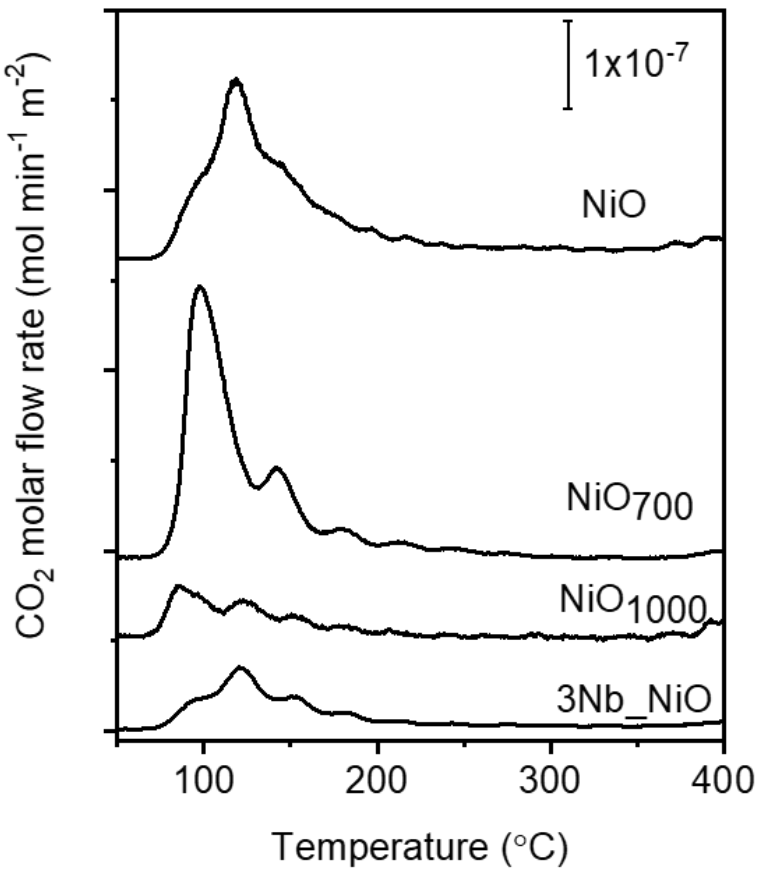

Figure 5-10. Temperature programmed CO_2 desorption profiles of (from top to bottom) NiO, NiO700, NiO1000, 3% Nb-NiO. The amount of CO_2 desorbed are summarized in Table 5-3.

5.3.4. The roles of non-stoichiometric oxygen in NiO-catalyzed ethane oxidation

5.3.4.1. The rates of partial and total ethane oxidation on oxygen species in nickel oxide

Under ethane oxidation over NiO catalysts, ethene forms via partial oxidation of ethane while CO_2 forms via total oxidation of ethane and ethene (Figure 5-11). Since we only focus on the primary ethane oxidations, the extent of secondary ethene oxidation is minimized by restricting ethane conversion below 3%. Cofeeding ethene with ethane and O_2, we observed only a slight increase in CO_2 formation rate, which confirms the limited ethene conversion to CO_2 at reaction-relevant condition. Therefore, the measured ethene and CO_2 formation rate shall each represent partial and total oxidation of ethane only. CO was not detected in the reactor effluent.

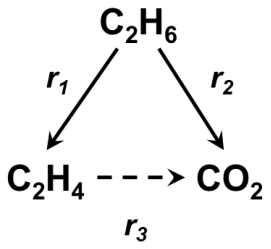

Figure 5-11. Proposed reaction network of ethane oxidation in the presence of O_2 with negligible extent of secondary reaction in current study.

In section 5.3.2, the adsorption capacities of CO_2 over lattice oxygen and NSO evolve differently with temperature, such that it exclusively adsorbs on NSO site under reaction temperature. This has led to potential use of CO_2 as an *in-situ* probing molecule for NSO, whose adsorption under reaction condition may be predicted by the Dual-site Langmuir model over site B (NSO) that is developed in section 5.3.2.

To validate the assumption, we first measured FTIR spectra of CO_2 adsorption with C_2H_6-O_2-CO_2 at 300 °C and found it replicated the shape of spectra of that with only CO_2 in present (Figure A5). No additional peak was observed, indicating that no other CO_2-derived species, i.e., bicarbonate forms on the surface. We then measured FTIR spectra of CO_2 adsorption at 300 °C under CO_2-O_2 flow and found that the spectra remained unchanged with increasing O_2 in the mixture (Figure A6). The observation suggests that NSO density is invariant to O_2 pressure, which coincides with O_2 desorption profiles that remain almost the same before and after exposing NiO samples to reaction condition or pure O_2 flow.[121] Therefore, NSO site density q_{sat} of 0.056 mol mol $_{\text{Surface Ni}}$ $^{-1}$ that is obtained by pure CO_2 adsorption can be used to estimate NSO site density under reaction. Another remaining question is whether the pure CO_2 Dual-site Langmuir model could quantitatively describe CO_2 adsorption under multicomponent gas mixture of CO_2-O_2-C_2H_6. If C_2H_6 or O_2 also adsorbs on NSO, the competitive adsorption will lead to lower CO_2 isotherm than that with only CO_2 presents. CO_2 isotherm under multicomponent adsorption can be estimated by ideal adsorbed solution theory (IAST) if adsorption isotherm of each component is available.[133, 143 , 144] Unfortunately, neither C_2H_6 nor O_2 adsorption isotherm is available over NiO. To limit multicomponent adsorption on NSO which makes CO_2 adsorption for NSO site count less reliable, we kept C_2H_6 and O_2 pressure constant while studying CO_2 cofeed over a wide range of CO_2 pressure.

In addition, since CO_2 adsorption occurs reversibly over NSO site under reaction temperature (Figure 5-9), we expect that after removing CO_2 from the reactant stream, carbonate will desorb as CO_2 from the surface and re-expose NSO site.

The introduction of 2 to 10 kPa CO_2 leads to a systematic decrease in ethene formation rate from 0.033 to 0.015 mol mol $_{Surface\ Ni}^{-1}$ (Figure 5-12). When CO_2 is turned off from the reactant flow at time 0, the ethene formation rate instantly recovers and gradually reaches the level before CO_2 is not cofed after 400 min. The exposed NSO density during purging was calculated by subtracting Langmuir isotherm of CO_2 measured at the reaction effluent from total NSO surface density predicted by DSL model. The recovery of ethane partial oxidation rate corresponds well with NSO re-exposed by removing CO_2. Total oxidation of ethane is also evaluated by cofeeding $^{13}CO_2$ with $^{12}C_2H_6$ and O_2. Figure 5-13 shows that CO_2 formation rate follows similar decay as ethene formation rate with increasing CO_2, indicating that CO_2 inhibition presents for both reactions.

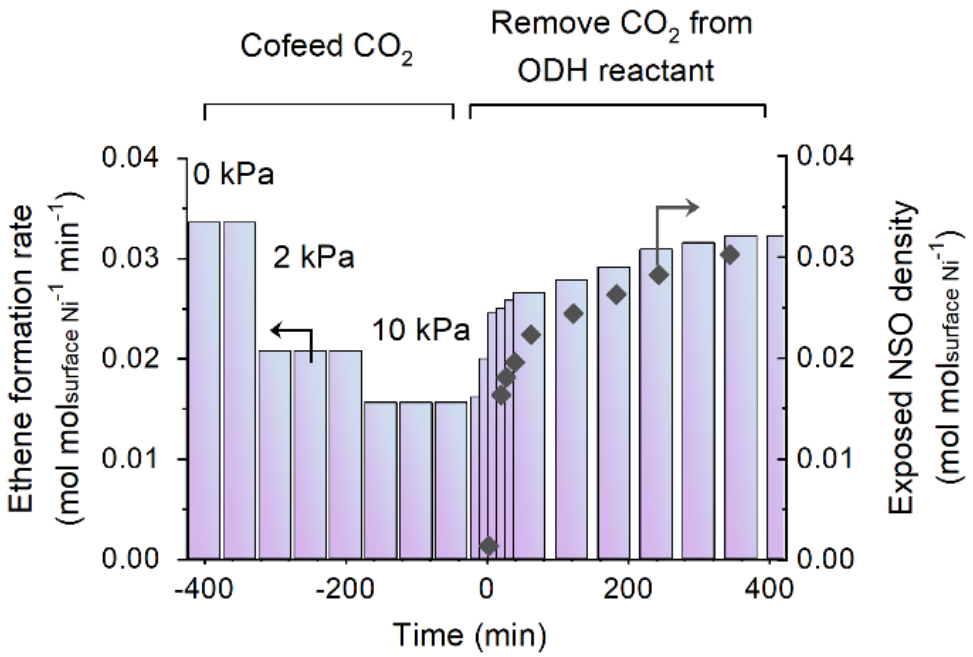

Figure 5-12. Ethene formation rate (histograms, left y-axis) as a function of CO_2 cofeed pressure and time. Transient NSO density (diamond symbols, right y-axis) after turning off CO_2 is plotted to the right y axis.

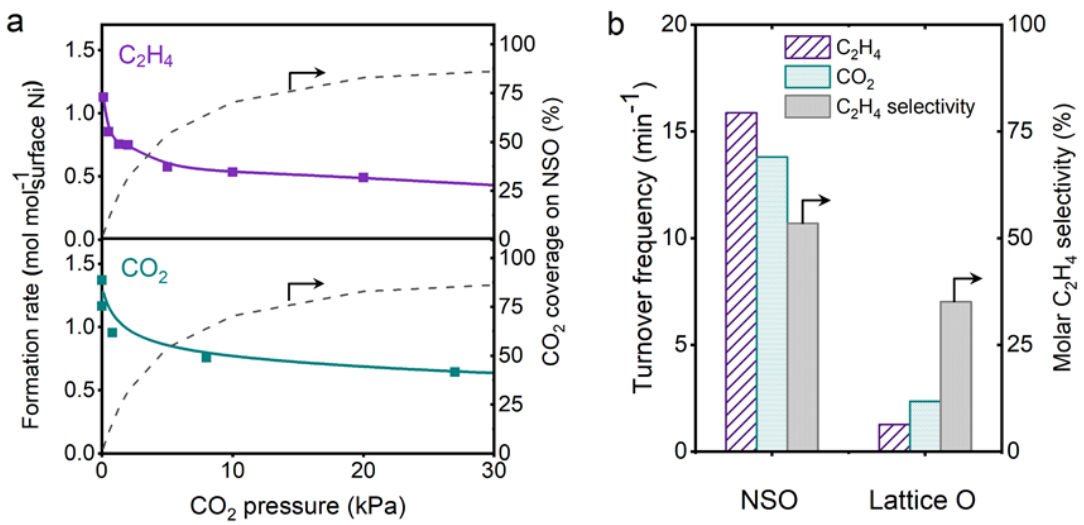

Figure 5-13. (a) Formation rate of C_2H_4 and CO_2 with increasing CO_2 pressure, with CO_2 coverage plotted to the right y-axis. (b) Estimated turnover frequency of two sites towards C_2H_4 and CO_2, with molar C_2H_4 selectivity plotted to the right y-axis.

As a common by-product of reactions involving hydrocarbon, the inhibitory effect of CO_2 on selective and unselective oxidation reaction has been widely identified under oxidative coupling of methane (OCM) catalysts such as Li/MgO[145-147] and La_2O_3,[148-150] which has been attributed to the formation of carbonate species or carbonated phase that poisons the active sites. Chu and coworkers compared the activity of La^{3+}–O^{2-} and La^{3+}–CO_3^{2-} pair sites for methane activation using DFT calculation and found that the calculated energy barriers of La^{3+}–O^{2-} structures range from 134 to 192 kJ/mol, which are consistently lower than their carbonate counterparts.[151]

The inverse correlation between reaction rates and the calculated carbonate coverage on NSO site suggest that the inhibitory effect of CO_2 over NiO is caused by the formation of carbonate that titrates active NSO site. The inhibition is reversible once carbonate is desorbed and re-exposes the active site. Notably, neither partial and total oxidation can be eliminated even with 30 kPa CO_2 cofeed to titrate 90% NSO (Figure

5-13a). The residual activity at higher CO_2 cofeed might be explained by 1) a CO_2-titrated NSO structure with reduced activity or 2) a second active site whose presence is not affected by CO_2 under reaction condition. The activities of multiple oxygen species, including non-stoichiometric oxygen and lattice oxygen are widely discussed for metal oxide catalysts. Lemonidou and coworkers proposed that NSO and lattice oxygen work synergically in the ethane partial oxidation cycle over NiO, with NSO activates the first C-H bond of ethane, followed by lattice oxygen subtracting the second β-H to form ethene.[17] However, our result indicates that as the plausible second active site, lattice oxygen catalyzes the reaction even when NSO is unavailable. This interpretation is consistent with the activity of cubic NiO_{1000} for ethene and CO_2 formation, whose NSO is eliminated after thermal treating the sample at 1000 °C.[121]

5.3.4.2. Identity of active sites for ethane oxidation reaction cycle on NiO(100)

Over NiO catalyst, Yao and coworkers have reported a kinetic isotope effect $k_{C\text{-}H}/k_{C\text{-}D}$ of 2.2[152] for CO_2 formation, and Skoufa and coworkers reported $k_{C\text{-}H}/k_{C\text{-}D}$ of 2.9[153] for ethane conversion. These significant kinetic isotope effects suggest that rate limiting steps of ODH and total oxidation of ethane both involve C-H bond breaking, which has also been found for ODH and total combustion of propane over vanadium oxide catalysts.[154]

To pinpoint the contributions of surface oxygens in the presence of Ni vacancies to ethane ODH, we calculated the thermodynamics of consecutive C-H bond activation over NiO-Ni_v, NiO-Ni_v+O_{ad}, and NiO-Ni_v+CO_3, which represents the NSO site when titrated by CO_2. Surface models without Ni vacancy were shown to bind CO_2 less

strongly and did not agree as well with the FTIR in section 5.3.3.2; hence, we limit our discussion of these sites and report the corresponding C-H bond scission enthalpies in Table 5-4 with enthalpies on other sites mentioned in section 5.3.3.1 and corresponding configurations summarized in Table A3 and Figure A7. This is supported by the work done by Mushrif and coworkers that NiO catalyst with Ni vacancy has a higher activity for methane C-H bond activation than the stoichiometric NiO.[119] Moreover, using the reaction enthalpy of C-H bond activation as indicator for catalytic activity is supported by the linear trend between the activation barrier and the reaction energy of methane dissociation observed by Mushrif and coworkers[119], and the report by Latimer et al. relating the C-H activation barrier to the binding strength of H in the final state.[88]

Table 5-4. Reaction enthalpy ΔH (eV) of ethane C-H bond scission over NiO-Ni_v, NiO-Ni_v+O_{ad} and NiO-Ni_v+CO_3.

Site	Reaction Enthalpy ΔH (eV)	
	$C_2H_6 \rightarrow C_2H_5 + H$	$C_2H_5 + H \rightarrow C_2H_4 + 2H$
NiO-Ni_v	-1.85	0.66
NiO-Ni_v+O_{ad}	-3.88	0.53
NiO-Ni_v+CO_3	-1.87	-0.27

Figure 5-14 shows the thermodynamic potential energy diagram for C-H bond scission over surface oxygen, oxygen adatom and carbonate near a nickel vacancy and the corresponding adsorption geometries are depicted in Figure 5-15. The violet curve in Figure 5-14 shows that the first C-H bond scission catalyzed by a NSO near a Ni vacancy is strongly exothermic with -3.9 eV. In contrast, C-H bond activation by lattice oxygen on NiO-Ni_v (black), or carbonate (blue) is much less exothermic and releases only ca. -1.9 eV. Assuming that the first C-H bond activation is rate controlling and

follows the well-established Brønsted–Evans–Polanyi (BEP) relations,[155,156] the NSO site near a Ni vacancy can be expected to be most active.

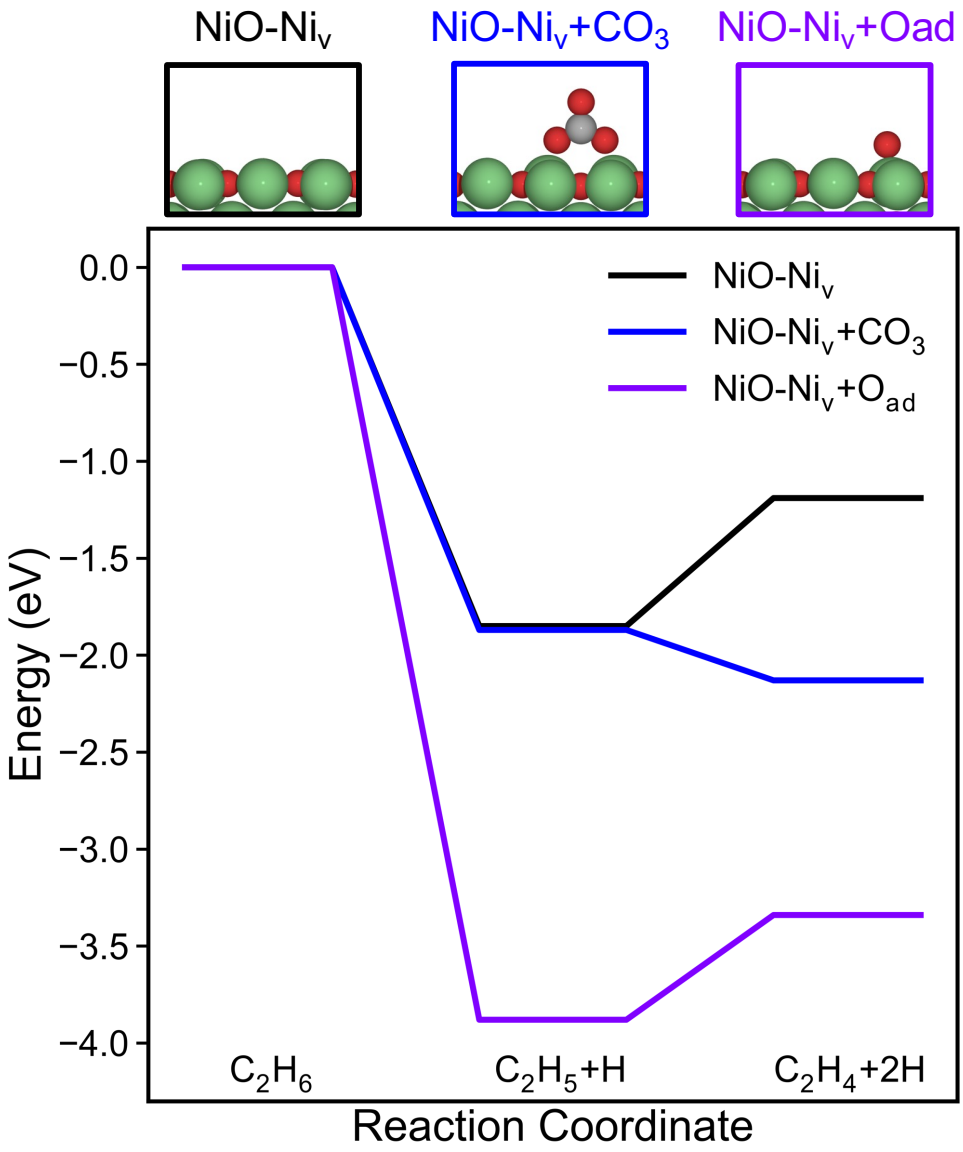

Figure 5-14. Potential energy diagram of C-H bond scission activated by the lattice oxygen near a nickel vacancy (black line), the NSO near a nickel vacancy (violet line), and the carbonate (blue line).

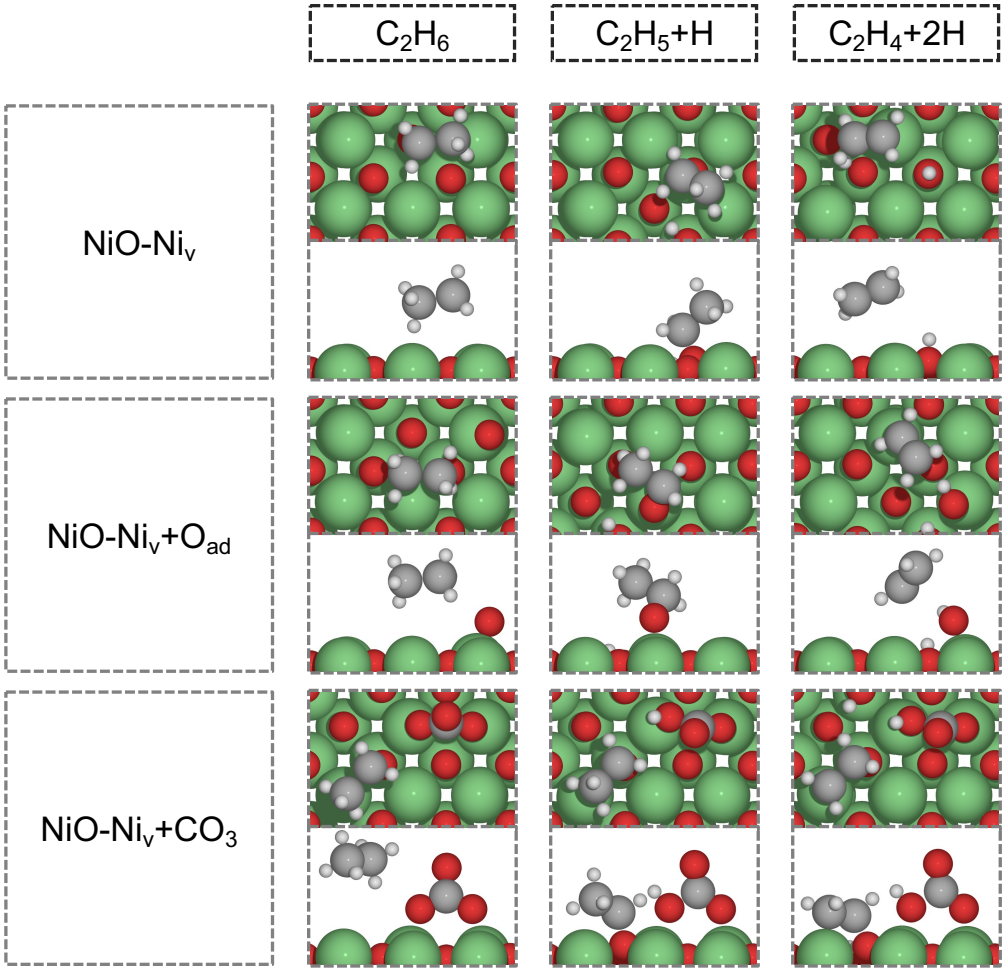

Figure 5-15. Top and side views of ethane C-H bond scission configurations on NiO-Ni_v, NiO-Ni_v+O_{ad} and NiO-Ni_v+CO_3.

The catalytic role of lattice oxygen and surface carbonate in H abstraction has been evaluated over reducible metal oxides both experimentally and computationally. The appearance of ^{16}O in CO_2 and H_2O persists for 15 min after switching the reactant flow from $C_2H_6/^{16}O_2$ to $C_2H_6/^{18}O_2$ over $Ni^{16}O$ catalyst, which is consistent with reactions proceeding a Mars-van Krevelen-like mechanism with oxygen provided by the catalyst.[157] Dinse and co-workers studied the role of lattice oxygen over vanadium oxide catalysts. C_2H_4, CO and CO_2 were formed after exposing fully oxidized VO_x to ethane, while pre-reducing the catalyst led to less product formation. The initial activity of the

catalyst has been attributed to lattice oxygen whose density decreases after pre-reducing the sample.[158] However, over NiO catalysts, ethane oxidation cannot persist without O_2 due to the facile and complete reduction from oxide to metallic Ni in pure C_2H_6 under reaction relevant temperature.[120]

The computational results imply three plausible active sites: NSO, surface carbonate, and lattice oxygen. The former two sites are interconvertible through CO_2 adsorption/desorption, whose surface densities sum up to be 0.056 mol mol $_{\text{surface Ni}}^{-1}$. Lattice oxygen density is 0.220 mol mol $_{\text{surface Ni}}^{-1}$ which is not affected by CO_2. We could then define the difference between turnover frequencies of NSO and carbonate site to be the reduction in rate per CO_2 adsorbed on NSO as

$$Turnover\ frequency_{\ NSO,C2H4} - Turnover\ frequency_{\ Carbonate,C2H4} = \frac{Decrease\ in\ C_2H_4\ formation\ rate(relative\ to\ no\ CO_2\ cofeed)}{Decrease\ in\ exposed\ NSO\ density(relative\ to\ no\ CO_2\ cofeed)}. \quad (5\text{-}8)$$

On the other hand, when CO_2 is removed from the reactant stream, its pressure inside the reactor and in turn the carbonate coverage on NSO also evolves with purge time on stream (Figure A8). If we assume that the adsorption equilibrium is reached at any time during purging, we could also define the difference between the transient turnover frequency of NSO and carbonate site to be the increase in rate per CO_2 desorbed from NSO as

$$Transient\ turnover\ frequency_{\ NSO,C2H4} - Transient\ turnover\ frequency_{\ Carbonate,C2H4} = \frac{Increase\ in\ C_2H_4\ formation\ rate\ (relative\ to\ CO_2\ cofeed)}{Increase\ in\ exposed\ NSO\ density\ (relative\ to\ CO_2\ cofeed)}. \quad (5\text{-}9)$$

We also assume equal turnover frequency between carbonate and lattice oxygen.

The ODHE rates measured by CO_2 cofeeding were used to calculate the turnover frequencies by Equation 5-8, while the rates measured by CO_2 purging were used to calculate the transient turnover frequencies by Equation 5-9. Since CO_2 is produced as a total oxidation product, even when CO_2 is not cofed, carbonate coverage on NSO site will be non-zero and increase along the bed. To take that carbonate coverage on the NSO into account, we have estimated the average carbonate coverage in the absence of CO_2 cofed by considering the average CO_2 pressure inside the reactor to be half of that measured at the reactor outlet. The exposed NSO density in the absence of CO_2 cofeed is then calculated by subtracting the average carbonate coverage from the total NSO density. As shown in Figure 5-16, both measurements result in similar NSO turnover frequencies, which are 0.4, 2, and 16 min^{-1} at 280, 320, and 375 °C, respectively. Moreover, the calculated turnover frequencies remain constant under each temperature. We also evaluate the case where NSO and lattice oxygen are the only two active sites whereas the resultant carbonate shows no activity to reaction turnovers. The resultant turnover frequencies of NSO is similar to the results in Figure 5-16. The similarity between two cases can be explained by the relatively low carbonate density compared to lattice oxygen and the low carbonate activity compared to NSO, which render carbonate contribution to the overall rate insignificant compared to the other two sites. Therefore, whether NSO-derived carbonates are active or not does not affect the calculated TOF values as long as that carbonate and lattice oxygen are almost equally active.

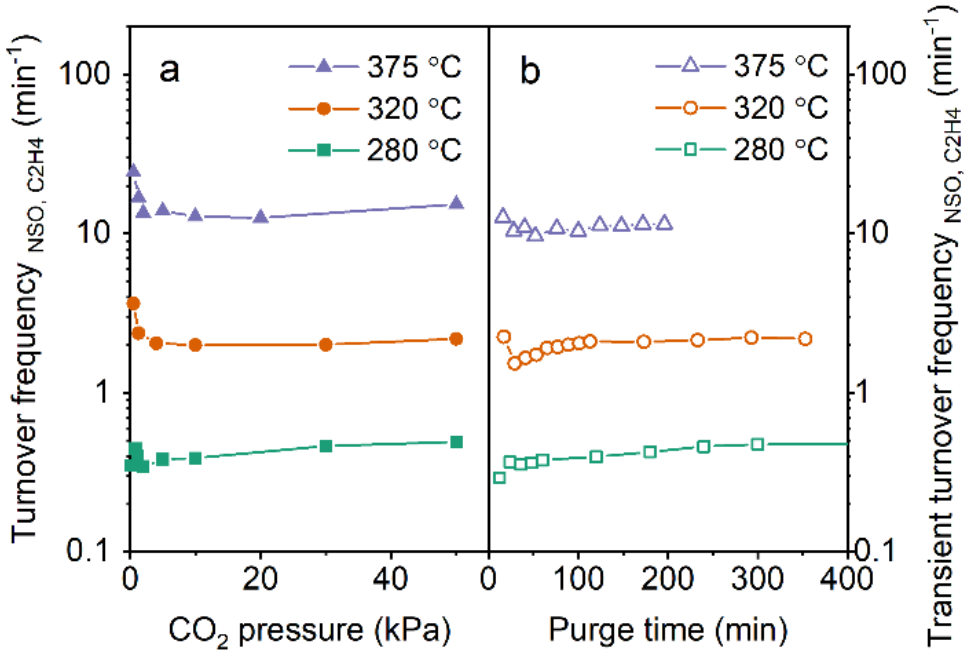

Figure 5-16. (a) Ethene turnover frequency evaluated by CO_2 cofeed. (b) Transient ethene turnover frequency evaluated by removing CO_2 from the reactant stream.

In Figure 5-13b, the turnover frequencies of NSO and lattice oxygen toward both partial and total oxidation at 375 °C are compared. Both reactions have significantly higher rate on NSO than lattice oxygen, which is consistent with NSO being the more thermodynamically favored site for C-H activation. The ethene selectivity under ethane oxidation is 52% over NSO, which is slightly higher than 38% of lattice oxygen. ODHE with CO_2 cofeed were further measured over NiO_{700} and NiO_{1000}, and the surface area-normalized ethene formation rates are plotted in Figure 5-17. We assumed that NSO was predominantly available with no CO_2 cofeed. NSO-related activity, which is represented by the maximum reduction in rate with CO_2 titration decreases from 0.025 mol mol $_{\text{surface Ni}}^{-1}$ min^{-1} for NiO to 0.005 mol mol $_{\text{surface Ni}}^{-1}$ min^{-1} for NiO_{700} and NiO_{1000}, whereas lattice oxygen-related activity, which is represented by the residual rate that is

unaffected by CO_2 remains relatively constant (0.01 mol mol $_{surface\ Ni}^{-1}$ min^{-1} for NiO and NiO_{700}, 0.005 mol mol $_{surface\ Ni}^{-1}$ min^{-1} for NiO_{1000}). The decrease in NSO-related rate with increasing thermal treatment is consistent with the increase in NSO surface density measured by FTIR (Figure 5-8), as well as CO_2 chemisorption and CO_2-TPD results summarized in Table 5-3 if we assume the NSO turnover frequency remains relatively constant for each sample.

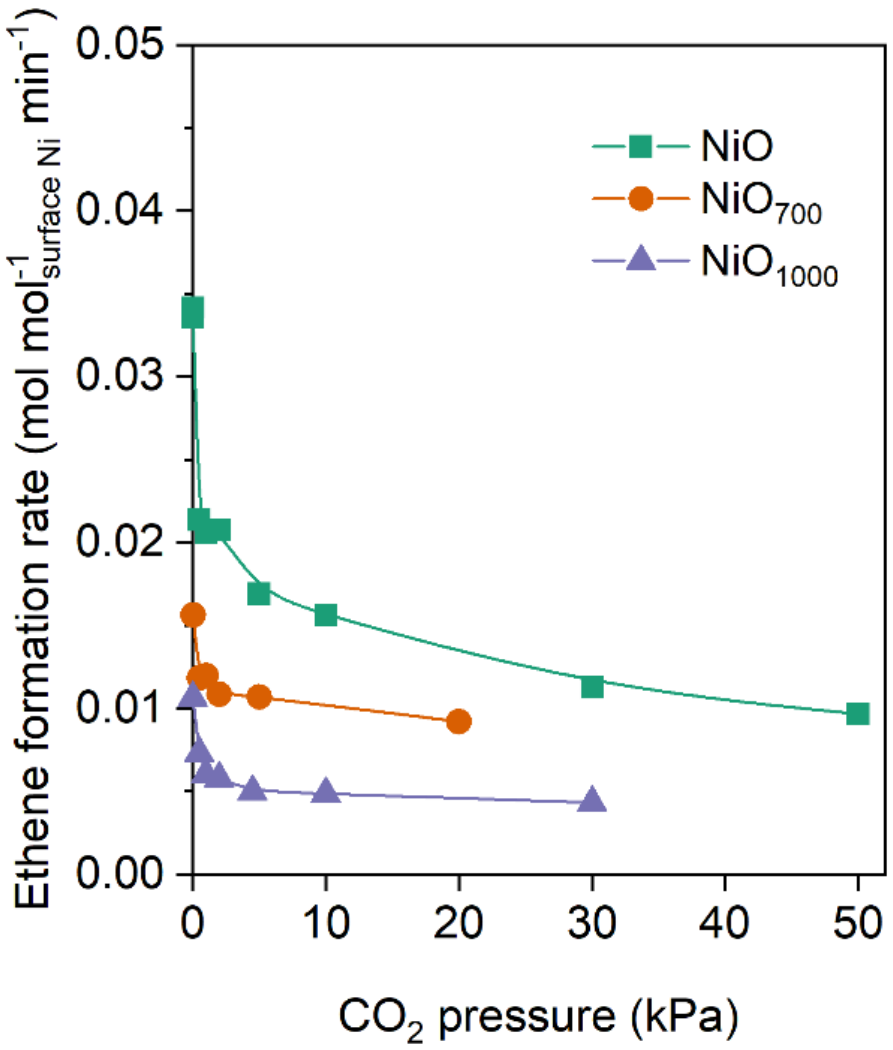

Figure 5-17. Formation rate of C_2H_4 during ethane oxidation with increasing CO_2 cofeeding pressure. 280 °C,10 kPa C_2H_6/10 kPa O_2/0.5-50 kPa CO_2.

The calculated heats of C-H bond activation in Figure 5-14 are consistent with the experimental results shown in Figure 5-13. With CO_2 cofeed, the formation rates of C_2H_4 and CO_2 decrease due to the titration of NSO, which is the most active site for the ODH and total oxidation reaction. The residual rate shown in Figure 5-13 is the result of the reaction activated by lattice oxygen, which is less active for ODHE reaction but has much higher site density than NSO.

Based on the experimental results and the reaction thermodynamics calculated by DFT, we were able to propose a schematic mechanism for the ODHE reaction on NiO(100) with Ni vacancy and the process of NSO titration by CO_2, shown in Figure 5-18. Ethane ODHE proceeds via a Mars-van Krevelen-like mechanism over NSO and lattice oxygen. Either oxygen species can abstract two H atoms from C_2H_6 and leave the surface as H_2O following the steps represented by red arrows and the indicated reaction enthalpy ΔH as in Figure 5-18a. The steps shown in blue correspond to the adsorption and dissociation of O_2. When NSO is available (the Ni_v+O_{ad} surface), the dehydrogenation of ethane can proceed a strongly exothermic step with -3.38 eV enthalpy, resulting in the Ni_v surface without NSO. The subsequent dehydrogenation step using lattice oxygen is exothermic by -1.7 eV and leaves an O vacancy near the Ni vacancy (the Ni_v+O_v surface). A further dehydrogenation step using lattice oxygen would be endothermic by 0.81 eV, whereas the dissociative adsorption of O_2 to heal the O vacancy and regenerate the NSO near Ni vacancy is thermodynamically favorable with ΔH = -0.17 eV. The regeneration of NSO closes the top catalytic cycle, the NSO cycle, in Figure 5-18a. Alternatively, the ODHE reaction can proceed via the lattice oxygen cycle (LO cycle), which is characterized by two ethane dehydrogenation steps

using lattice oxygen where the second step is endothermic. The resulting double oxygen vacancy is healed and the cycle is closed by strongly exothermic O_2 dissociation to regenerate the Ni vacancy surface. While the NSO and LO cycles have dehydrogenation step on the Ni_v surface in common, the availability of NSO is expected to lead to a higher activity because it avoids the endothermic step in the LO cycle. Thus, when the concentration of NSO site is lowered as CO_2 pressure increases, i.e., titration with CO_2, as depicted in Figure 5-18b, the reaction is forced to follow the LO pathway and the overall ODHE reaction slows down. However, further investigation is still needed to fully prove and understand the mechanism.

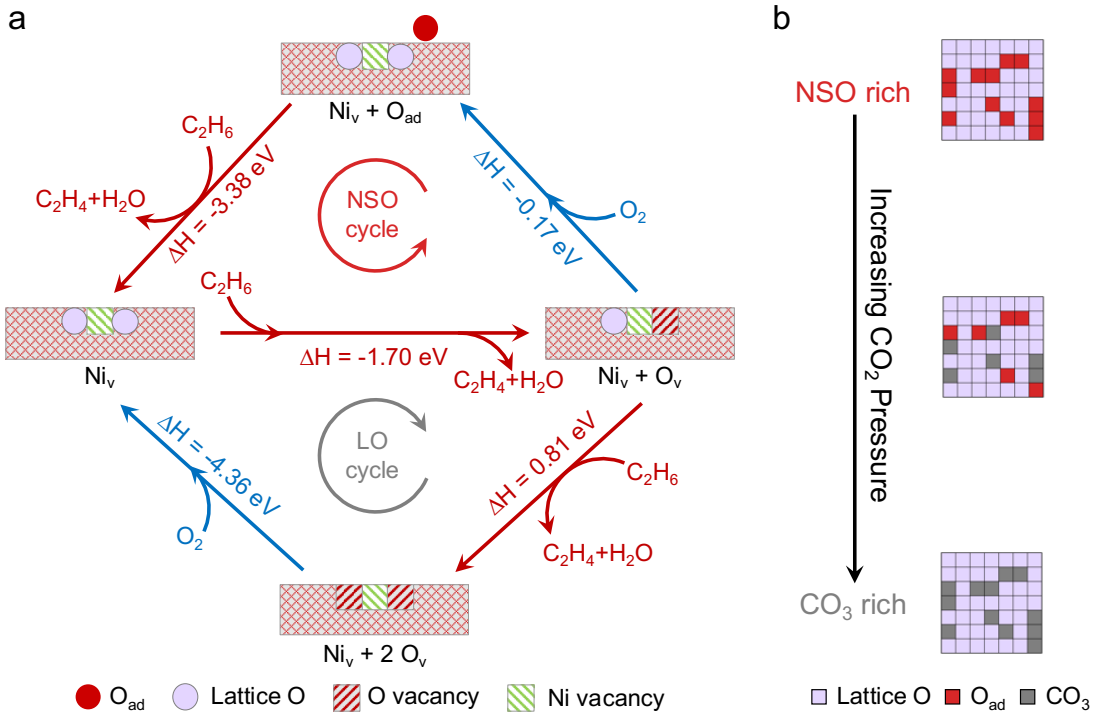

Figure 5-18. (a) Proposed mechanism of the ODH reaction with and without the availability of O_{ad} as NSO. (b) The titration of NSO sites with increasing CO_2 pressure with LO sites not affected under reaction condition.

5.4. Conclusion

As discussed in this chapter, we used a quantitative analysis of CO_2 adsorption to investigate the catalytic role of different oxygen sites on NiO catalysts during oxidative dehydrogenation of ethane (ODHE). Two surface oxygen species were evidenced by CO_2 equilibrium adsorption isotherms, Fourier-transform infrared spectroscopy (FTIR) measurements and reversibility assessments. DFT calculations of CO_2 adsorption over stoichiometric NiO(100) surface and surfaces with nickel and oxygen vacancies show a stronger CO_2 binding to O adatoms than lattice oxygens, and the adsorption is favored over NiO with a Ni vacancy compared to surfaces with stoichiometric termination or oxygen vacancy defects. The predicted vibrational frequencies of adsorbed CO_2 formed over O adatom and lattice oxygen site on NiO with a Ni vacancy match well with the two groups of peaks in the experimental FTIR spectra, which have different responses to temperature, inferring a strongly adsorbed CO_2 to non-stoichiometric oxygen (NSO) and a weakly one to the lattice oxygen.

In addition, leveraging CO_2 as probe molecule with specificity for NSO under reaction condition, we have demonstrated for the first time the activity of NSO in both ODHE and total oxidation. The decrease of reaction rates subjected to CO_2 cofeed corresponds with the decrease of NSO surface density under steady state and transient conditions, whereas residual rates can be attributed to surface lattice oxygen or the formation of surface carbonate species that are less active. These observations are further supported by DFT calculations on three sites. Non-stoichiometric oxygen is the most favorable for C-H activation of ethane, followed by lattice oxygen and surface carbonate. Based on these results, we have proposed a reaction cycle that the ODHE

reaction proceeds among the NSO and lattice oxygen on NiO(100) with Ni vacancy, and the active sites are regenerated by dissociative adsorption of O_2 molecules. With NSO being titrated, the reaction cycle may proceed on sites that are less active, such as the lattice oxygen and oxygen vacancy. The shift of active sites makes the further investigation of the comprehensive reaction mechanisms of great interest.

Collectively, a structural-catalytic relation of oxygen under C-H bond activation has been established, with NSO being more active and selective for ethane oxidation than lattice oxygen. This relation rationalizes the detrimental effect of thermal annealing on ethene selectivity and activity by reducing the non-stoichiometric oxygen surface density. This finding provides more insights into metal oxide surfaces and could help guide future developments in metal oxide catalysts towards tailored oxygen functionality.

Chapter 6. Structure and Wettability of CH_3- and CF_3-Terminated *n*-Alkyl Xanthic Acid Self-Assembled Monolayers: Odd-Even Effects Addressed by Surface Dipole

This chapter presents the work done by the collaboration with Hung-Vu Tran from Dr. Randall Lee's group. Experiments including the synthesis, characterization and reaction kinetic measurements were done by Hung. Our contribution is limited to the computational perspective, including the molecular dynamic simulation of the SAMs and analysis of the tail group tilt angle.

6.1. Introduction

Self-assembled monolayers (SAMs) are highly ordered materials of (organic) molecules that bond to a surface, which are widely used for surface modification.[21,24-28] Organic Fluorinated polyethylene was found to be much less wettable than polyethylene,[159] indicating its application in the production of lubricants, cookware, antiadhesives and building materials. Fluorinated SAMs is one of the analogies of the fluorinated polyethylene. With the nature of the highly ordered structure of SAMs, the fluorinated SAMs are of great interest for the design of wettability controlling materials.

Lee et al. have performed the contact angle measurements to probe the wettability of SAMs prepared from alkanethiols and the CF_3-terminated alkanethiols.[160] Choosing nonpolar, polar protic and polar aprotic solvents as the test liquids, they have brought the idea that the wettability of SAMs are affected by the dipole-dipole interaction

between the liquids and the surface. The oriented CF_3 tail group generates a strong dipole at the interfacial and the dipole-dipole interaction depends on the orientations of the CF_3 group,[161] which have a parity dependence on the number of carbon atoms in the carbon chain, referred to as the odd-even effect. They have continued to this work and reported the contact angle measurements on SAMs of alkanethiols with increasing degree of fluorination.[162] Results suggest that the contact angle for nonpolar liquids increases with the degree of fluorination due to the weaker dispersive interaction between the liquids and the SAMs.[163] However, for polar protic and polar aprotic liquids, the contact angles exhibit a minima at the first introducing of fluorination, which is attributed to the presence of CF_3-CH_2 dipoles. As the degree of fluorination increases, the contact angles increase and converge to a maximum since the CF_3-CH_2 are buried into the monolayer and away from the interface between the liquids and the SAMs. The larger odd-even effect shown in CF_3-terminated SAMs than the CH_3-terminated SAMs also confirms the dipole-oriented effects on the wettability.

Other than alkanethiols, Lee and colleagues have also reported the investigation of SAMs with different organic molecules, such as dithiolcarboxylic acids and alkyl xanthic acids.[164] The results of contact angles of hexadecane show that the SAMs generated from alkyl xanthic acids have larger odd-even effect than those generated from alkanethiols, but similar to those generated from dithiolcarboxylic acids. The measurements of SAMs remaining fractions over time also indicate the stability if SAMs being: alkanethiols SAMs > dithiolcarboxylic acids SAMs > alkyl xanthic acids SAMs.

To gain a geometric understanding of SAMs at atomic level, we have performed molecular dynamic simulations to simulate the formation of alkyl xanthic acids SAMs on Au(111). Though the length of carbon chain was limited due to the computational efficiency, and odd-even effect was observed for the orientation of the tail groups. Combining the results of contact angle measurements, our results indicate the dipole-oriented effects on the wettability of alkyl xanthic acids SAMs.

6.2. Methods

6.2.1. Computational methods

The molecular dynamic simulations were performed using CP2K.[52] A DZVP-MOLOPT-GTH basis set and GTH-PBE pseudopotentials were used with a plane wave basis set with the energy cutoff of 500 Ry. The cutoff value was optimized by performing a series of single point calculations of gold surface and the optimized value was obtained until the energy shows no change to the increasing cutoff value. BEEF-vdW functional was used to describe the exchange-correlation. The self-consistent field cycle was terminated when the change in total energy was lower than 10^{-4} Hartree.

The molecular dynamic simulations were performed at constant temperature, volume and number of atoms (NVT), with Nose-Hoover thermostat being used.[49,50] The temperature was kept at room temperature, which is equivalent to the experimental condition of the growth of alkyl xanthic acids SAMs. Only alkyl xanthic acids molecules were allowed to relax and in each MD run, 5000 steps of 1 fs timesteps, 5 ps in total, were calculated and the resulting trajectories as well as the temperatures and potential energies along time were written, which can be further analyzed according to the

purpose of research. The example settings for the MD simulations are shown in the Appendix.

6.2.2. Model Description

All alkyl xanthic acids SAMs models were built using the Atomic Simulation Environment (ASE).[73] The lattice constant (LC) of ccp-gold was optimized to be 4.155 Å, which is within 2% error with the experimental measured value.[165] Considering the condensed structure of SAMs, a four-layer $\sqrt{3} \times \sqrt{3}$ Au(111) surface. A vacuum of 24 Å was added between slabs, assuring there is no interaction between the long carbon chain and neighboring slabs. Models of SAMs with CH_3-$(CH_2)_n$-OS_2 with n = 8-15 were built with initial guess of geometries sampled in Figure 6-1. The CF_3-$(CH_2)_n$-OS_2 were obtained by replacing the CH_3 tail group of converged CH_3-$(CH_2)_n$-OS_2 SAMs by CF_3, which helps increase the computational efficiency.

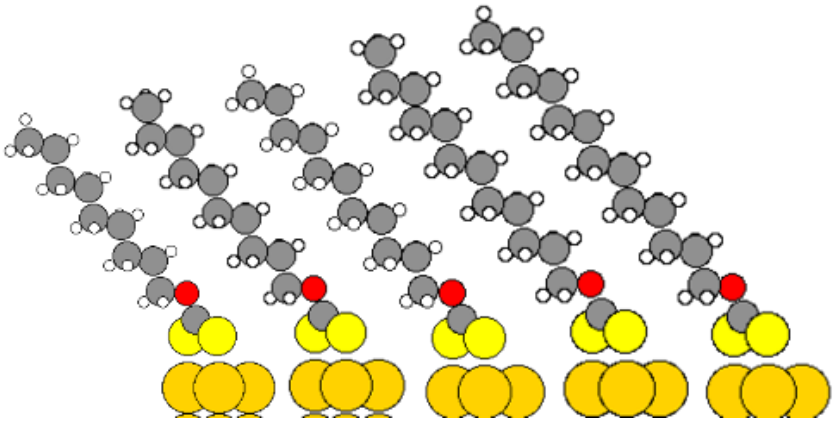

Figure 6-1. Initial guess of CH_3-$(CH_2)_n$-OS_2 SAMs geometries with n = 8-12.

6.3. Results Discussion

6.3.1. The temperature fluctuation

Though the MD simulations of a canonical system are performed at constant temperature, volume and number of atoms, temperature can be fluctuating along time caused by the spontaneous energy exchanges between the system and the thermostat.[166] The temperature fluctuation can be expressed by Equation 6-1[166]:

$$\langle (\Delta T)^2 \rangle = \frac{kT_0^2}{Nc_v^0}, \tag{6-1}$$

where $\Delta T = T - T_0$ is the deviation from the thermostat temperature T_0, c_v^0 is the constant-volume specific heat at temperature T_0, k is Boltzmann's constant and N is the number of particles. The brackets $\langle ... \rangle$ represents the time averaged value.

Figure 6-2 shows the temperature fluctuation in MD simulations of CH_3-$(CH_2)_8$-OS_2 and CH_3-$(CH_2)_{14}$-OS_2 SAMs. Results show that the simulations with larger number of particles (Figure 6-2b) has less averaged deviation from the thermostat temperature than that shown in Figure 6-2a, which is consistent with Equation 6-1.

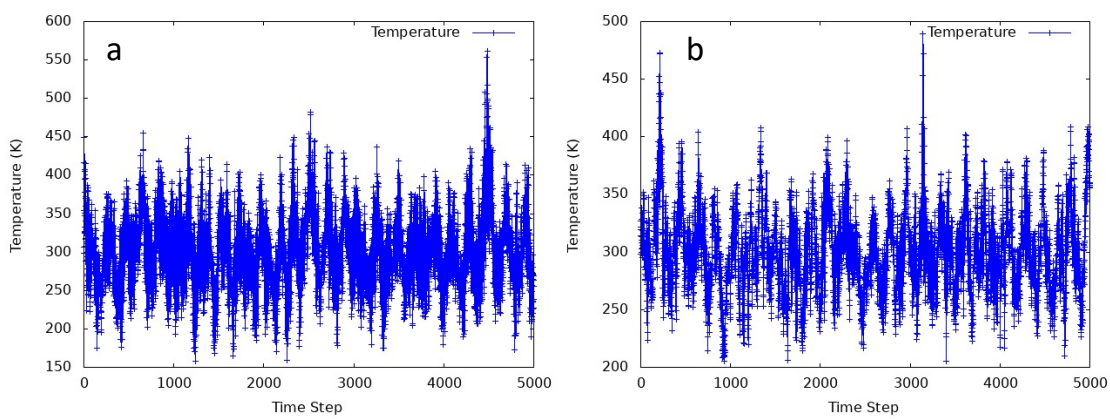

Figure 6-2. Temperature fluctuation of (a) CH_3-$(CH_2)_8$-OS_2 and (b) CH_3-$(CH_2)_{14}$-OS_2 SAMs.

6.3.2. Tilt angle of tail group of CH_3-$(CH_2)_n$-OS_2 SAMs

As shown in Figure 6-3a, three angles were monitored in the MD simulations: the angle between the line connecting O and tail C atoms and the surface normal, θ_1; the angle between the carbon skeleton and the surface normal, θ_2; and the angle between the tail C-C bond and the surface normal, θ_3. Figure 6-3b shows the resulting angles along time for CH_3-$(CH_2)_8$-OS_2 SAMs. The angles monitored along time for other CH_3-$(CH_2)_n$-OS_2 SAMs are summarized in Figure A9. The angle θ_1 is found to be less fluctuating than the other two angles due to the long distance between O and tail C atoms, and the fluctuation is smaller as the length of carbon chains increases. The angle θ_2 and angle θ_3 are fluctuating around a certain value, meaning that the time averaged values are capable for the analyzation for the angles according to different number of CH_2 units.

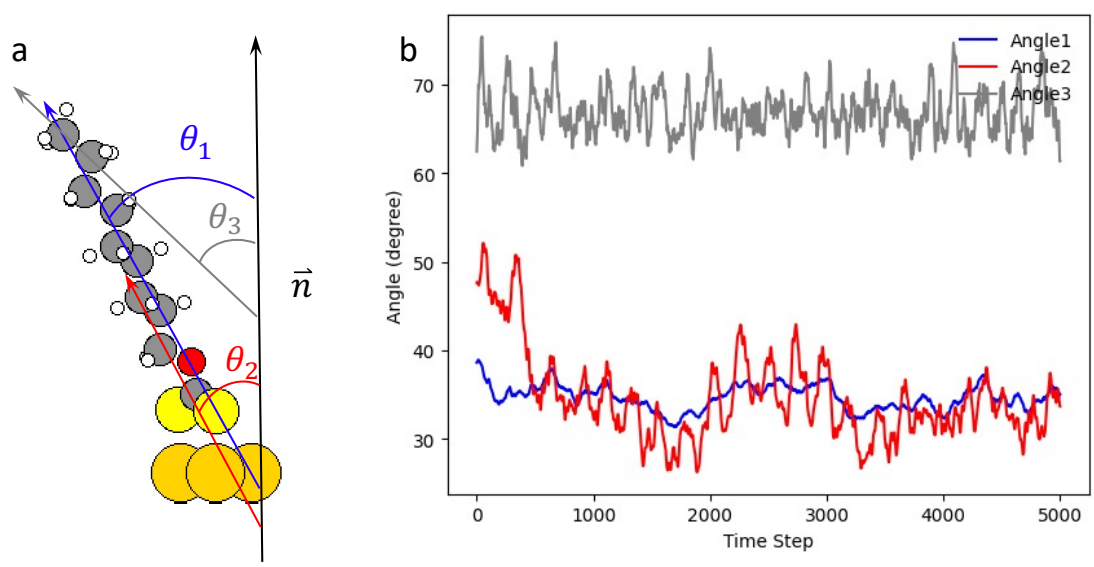

Figure 6-3. (a) The schemetic measurements of three angles: θ_1 (blue), θ_2 (red) and θ_3 (grey). (b) A sample result of θ_1 (blue), θ_2 (red) and θ_3 (grey) monitored along time for CH_3-$(CH_2)_8$-OS_2 SAMs.

Figure 6-4 shows the time averaged angles with respect to the number of CH_2 units. Compared with the relatively constant angle θ_1 and θ_2, the angle θ_3, which is the tilt angle of the tail CH_3 group exhibits an odd-even effect according to the carbon chain length. For CH_3-$(CH_2)_n$-OS_2 SAMs with n = odd, the angle θ_3 is ca. 50° except for an outlier at n=13; for CH_3-$(CH_2)_n$-OS_2 SAMs with n = even, the angle θ_3 is ca. 70°. The resulting geometries of the CH_3-$(CH_2)_n$-OS_2 SAMs give a good starting point of CF_3-$(CH_2)_n$-OS_2 SAMs. By replacing CH_3 by CF_3, the initial guess of CF_3-$(CH_2)_n$-OS_2 SAMs already have the oriented tail group according to the odd-even effect, which can significantly shorten the time needed to find the geometries around the global stable geometries.

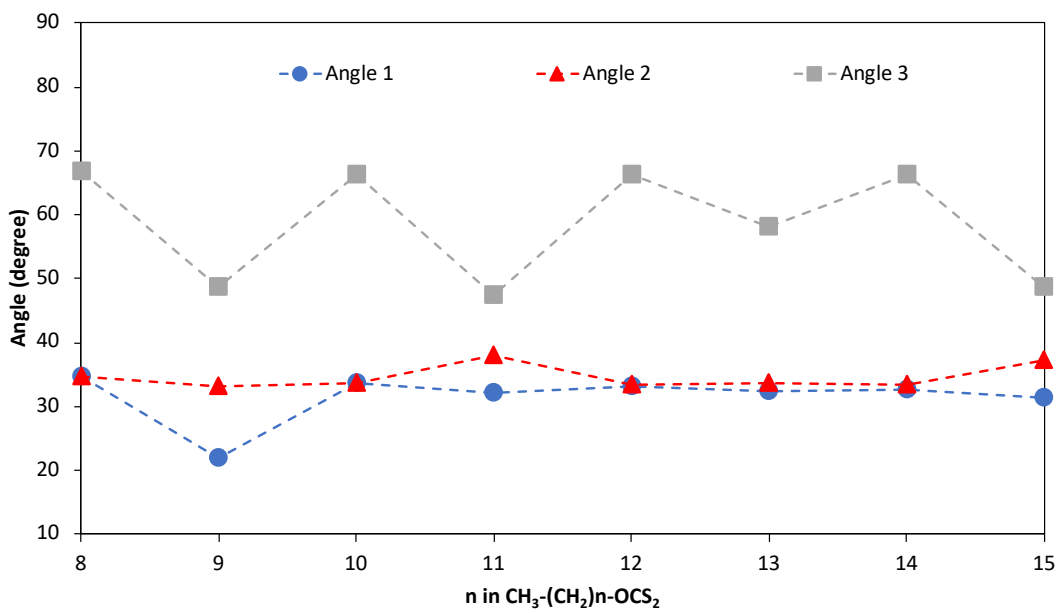

Figure 6-4. Time averaged angle θ_1 (blue), θ_2 (red) and θ_3 (grey) with respect to the number of CH_2 units in CH_3-$(CH_2)_n$-OS_2 SAMs.

6.3.3. Tilt angle of tail group of CF_3-$(CH_2)_n$-OS_2 SAMs

Same measurements of angles discussed in Section 6.3.2 were performed for CF_3-$(CH_2)_n$-OS_2 SAMs followed by the calculation of time average. The angles measured for each SAM are presented in Figure A10 and the time averaged angle θ_1 and θ_2, the angle θ_3 with respect to the number of CH_2 units are shown in Figure 6-5. Similar to what has been observed for CH_3-$(CH_2)_n$-OS_2 SAMs (Figure 6-4), the angle θ_1 and θ_2 are relatively constant while the angle θ_3 exhibits a larger odd-even effect. For CF_3-$(CH_2)_n$-OS_2 SAMs with n = odd, the angle θ_3 is ca. 20° and for CF_3-$(CH_2)_n$-OS_2 SAMs with n = even, the angle θ_3 is ca. 60°. According to the results shown in Figure 6-4 and Figure 6-5, the CF_3-terminated SAMs are able to double the tail group tilt angle difference due to the odd-even effect of the CH_3-terminated SAMs (from 20° to 40°). With the strong dipole generated by the CF_3 tail group,[161] the CF_3-$(CH_2)_n$-OS_2 SAMs are expected to have larger odd-even effect for the wettability of the materials since the surface dipole moment is the actual dipole generated by the CF_3 tail group projected to the surface normal.

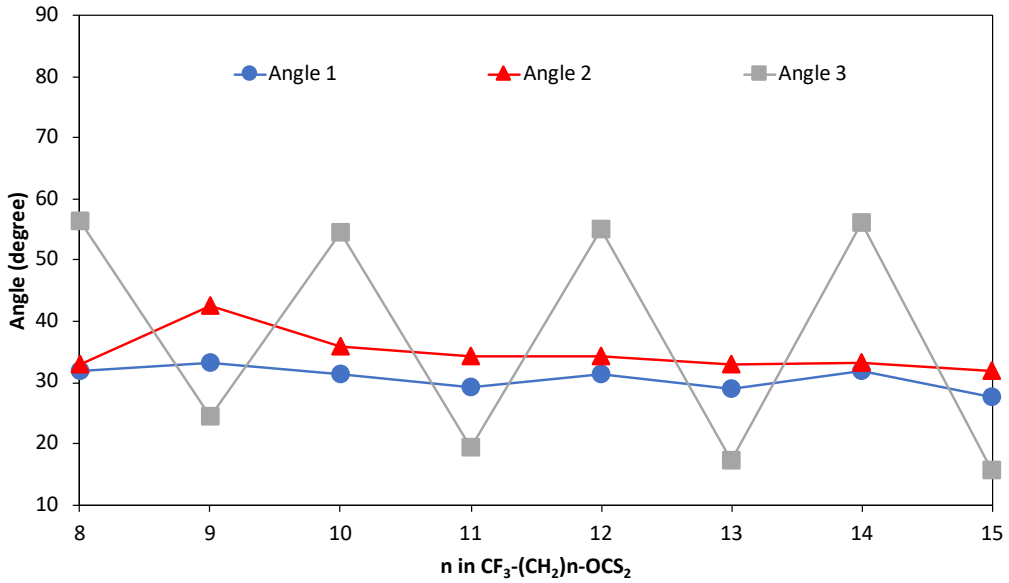

Figure 6-5. Time averaged angle θ_1 (blue), θ_2 (red) and θ_3 (grey) with respect to the number of CH_2 units in CF_3-$(CH_2)_n$-OS_2 SAMs.

6.4. Conclusion

A molecular dynamic simulation of the formation of CH_3- and CF_3-terminated *n*-alkyl xanthic acid self-assembled monolayers were performed and discussed in this chapter. With the relatively constant tilt angle of the carbon skeleton, the tilt angle of the tail groups CH_3 and CF_3 have strong dependence on the number of CH_2 units in the carbon chain due to its zigzag structure.

The tail groups of SAMs that have odd number of CH_2 units are more parallel to the surface, while the SAMs that have even number of CH_2 units have tail groups that are more perpendicular to the surface. Thus, the surface dipole moment, which is the projection of the dipole generated by the tail group to the surface normal, will exhibit an odd-even effect. The wettability, which can be affected by the dipole moment at the SAMs-liquid interface, of CF_3-terminated *n*-alkyl xanthic acid SAMs are expected to

have larger odd-even dependence on the number n since the difference between the tilt angles with odd and even *n* is larger than that of the CH_3-terminated *n*-alkyl xanthic acid SAMs.

Further investigation could be in the field of tuning the head groups,[164] the degree of fluorination[163] and the buried fluorinated segments,[32] which can bring a comprehensive understanding of the odd-even effect of SAM properties driven by the surface dipole.

Chapter 7. Perspective and Scope for Future Work

Throughout the dissertation, I have shown the attempts to activate the C-H bond of hydrocarbons using nickel oxide. While a reaction pathway with mild activation barrier for methane activation being presented and the active sites for ethane oxidation being identified, there is still a lot to be investigate, such as the reaction kinetics and the implementation of the dynamic rate enhancement. Moreover, the kinetic of ethane ODH reaction on NiO(100) needs to be studied to further complete the reaction mechanism, which will shed light on the selectivity towards aim products and guide the design of catalysts by tuning the surface oxygen species. Besides, due to the huge number of organic molecules, with different head and tail groups and the degree of modification, that can be used to form SAMs, the computational screening of the SAMs can be easily applied according to the strategy discussed in this dissertation and will help reduce a lot of the experimental work.

7.1. Microkinetic Modeling of Methane Conversion to Methanol

While the methane conversion to methanol is unlikely to proceed on Ni(111) based on the discussion in Chapter 3, the thermodynamics of the two mechanisms studied indicate that the reaction system is perfect for applying a microkinetic modeling.[167] As shown in Table 7-1, the CO_3-assisted mechanism has lower activation barrier for the first step, while the second step of O-assisted mechanism has lower activation barrier than that of CO_3-assisted mechanism, indicating a competition between the two mechanisms. The common step, which is the methanol formation, has the highest activation barrier among all elementary steps.

Table 7-1. Reaction Enthalpy ΔH (eV) and Activation Barrier E_a (eV) of elementary steps of CO_3- and O-assisted methane conversion to methanol on Ni(111).

Reaction	Reaction Enthalpy ΔH (eV)	Activation Barrier E_a (eV)
$CH_4(g) + CO_3* + * \rightarrow CH_3* + HCO_3*$	0.19	1.32
$HCO_3* + * \rightarrow OH* + CO_2*$	-0.44	0.27
$CO_3* +* \rightarrow CO_2* + O*$	-0.82	0.16
$CH_4(g) + O* + * \rightarrow CH_3* + OH*$	0.56	1.94
$CH_3* + OH* \rightarrow CH_3OH* + *$	0.20	2.02

Performing a microkinetic modeling calculation to the reaction system will help with the understanding of the coverage of the reaction intermediates, the rate determining step as well as the temperature dependence of the reaction rate of the two competing reaction mechanisms.

In addition to the temperature dependence, the methane electrooxidation on NiO(100) discussed in Chapter 4 can also have a microkinetic modeling analysis, which use the electric potential as the descriptor rather than temperature. Due to the increasing computational cost with higher applied electric fields in DFT calculations, the microkinetic modeling could bring insight on the change of surface species, rate determining step and reaction rate with respect to the applied potential. However, this needs to be done carefully since the potential dependence is based on the linear relationship between the binding energies and the applied potential as shown in Equation 4-2, which holds true as long as the adsorption geometry, i.e., the surface dipole moment, does not change. Thus, the potential dependence should be performed within the applied potentials that do not cause the geometry change.

7.2. Optimization of Dynamic Rate Enhancement of Methane Conversion to Methanol

As discussed in Chapter 4, the methane conversion to methanol on NiO(100) shows great potential to be dynamically accelerated by applying an oscillating potential between positive and negative potentials, leaving the optimal frequency and amplitude of the oscillation being untouched. According to Gopeesingh's work, an optimal frequency of oscillation exists (Figure 7-1), which matches with the kinetics of the surface reaction.[20] Such oscillation frequency is called catalytic resonance.

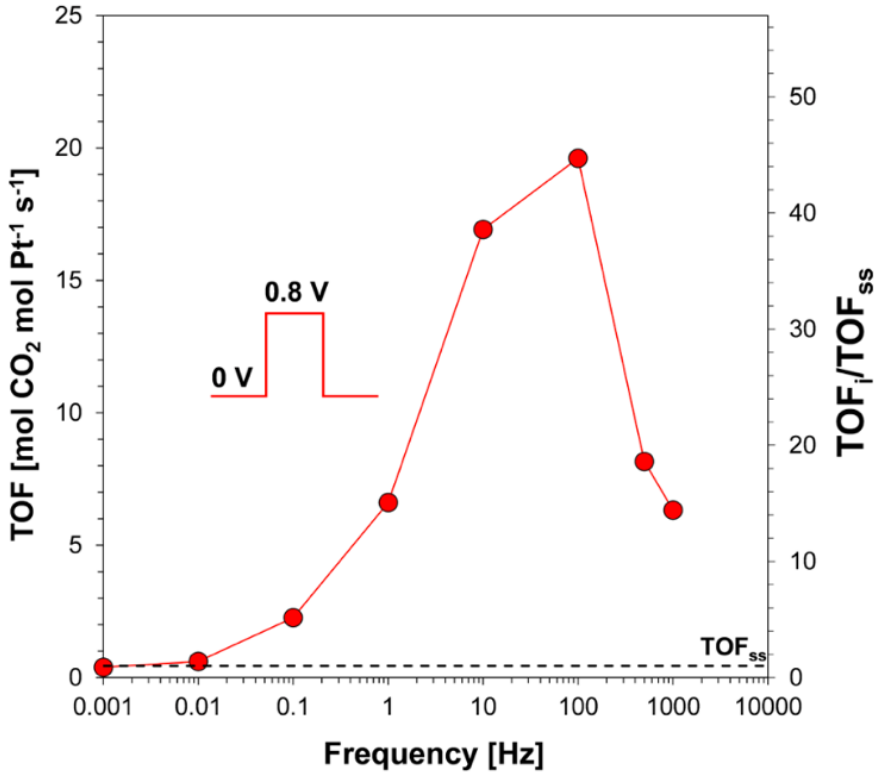

Figure 7-1. Time-averaged turnover frequency of dynamic formic acid electrooxidation on Pt with square wave applied potentials. TOF_{SS} is the steady-state reaction rate at fixed applied potential of 0.8 V.[20]

Accordingly, both experimental and computational investigations of the electrochemical methane conversion to methanol on NiO(100) are expected to provide an insight to the optimal frequency and applied potential of the oscillation which exhibits the highest rate enhancement. The approach can be further normalized for other catalytic processes that are partially accelerated by different applied electric fields.

7.3. Kinetic Study of Ethane ODH Reaction and its Side Reactions

While the active sites identified and corresponding thermodynamics of the ethane ODH reaction discussed in Chapter 5, the kinetics of the reaction remain untouched. The competing reaction, which is the CO_2 formation, also needs to be investigated. Lemonidou et al. have proposed that the adsorption site of ethyl group plays an important role in the selectivity towards ethene: the ethyl adsorbed to a metal atom will have its β-H abstracted by the neighboring O and produce ethene; while the ethyl adsorbed to an O atom will have the C-C bond scission and produce CO_2 eventually (Figure 7-2). [17] However, according to our results the most stable configurations of activated ethane were obtained when ethyl adsorbs to the oxygen atoms (Figure 5-15). Thus, the calculations of the activation barriers of both ethene and CO_2 formation are essential for the understanding of the activity and selectivity of different oxygen species. The results are expected to be valuable for guiding the design of ODH catalysts by tuning the surface to have more exposed sites that favor the ethene formation reaction and suppress the CO_2 formation reaction.

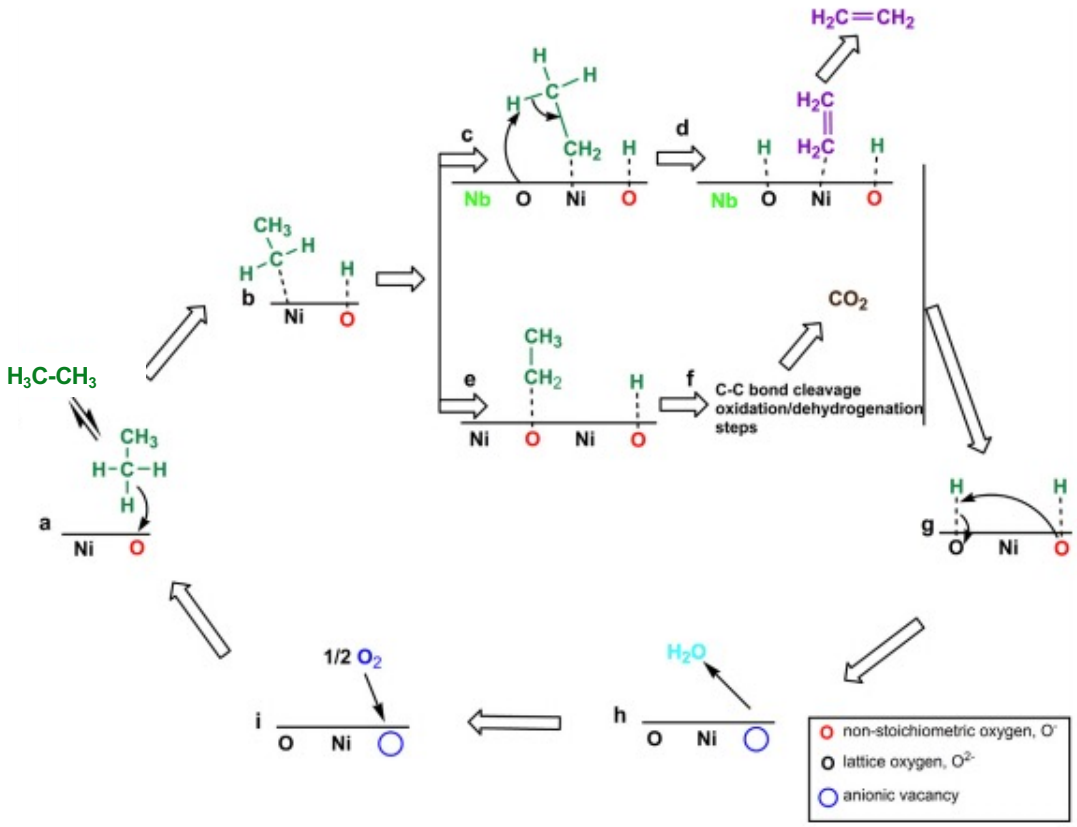

Figure 7-2. Proposed reaction mechanism for ethane ODH over NiO-based catalysts.[17]

7.4. Computational Screening of Self-Assembled Monolayers

The self-assembled monolayers can be modified by tailoring the head or tail groups or a segment of the organic molecules, resulting in a massive work of synthesis, characterization and property analyzation for the design of one SAMs with desired properties. For instance, with different head groups, the contact angles of hexadecane on SAMs exhibit the odd-even effect differently (Figure 7-3).

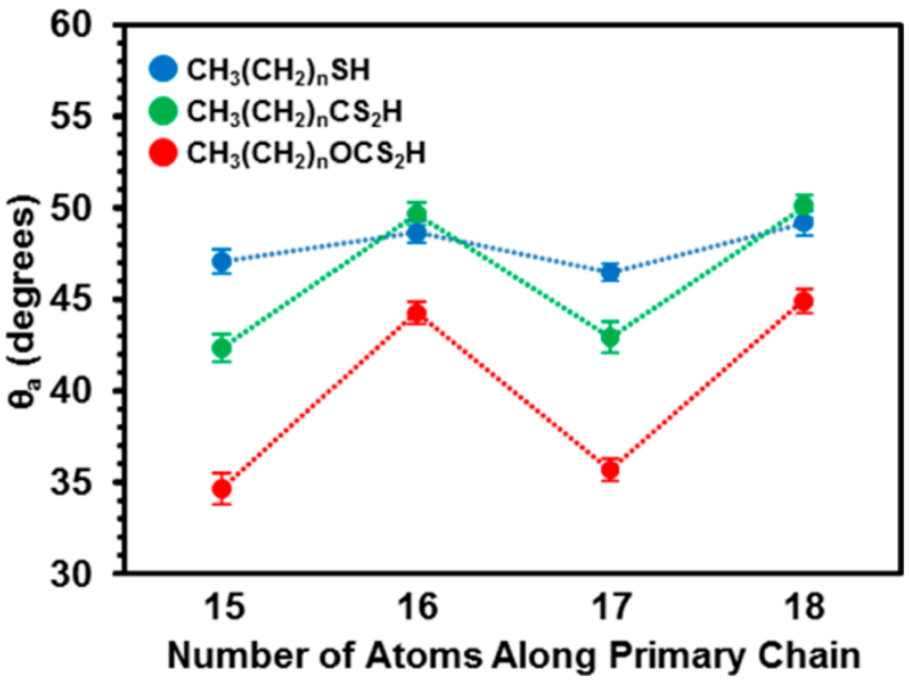

Figure 7-3. Contact angle of hexadecane on SAMs generated from n-alkanethiols (blue), dithiocarboxylic acids (green) and *n*-alkyl xanthic acids (red). The x-axis represents the total number of atoms in the chain's backbone.[164]

Computational screening of SAMs is a promising strategy to guide the SAMs design. As shown in Figure 6-4 and Figure 6-5, the tilt angle of the carbon skeleton remains constant for SAMs with more than ten CH_2 units. Thus, the tail group will have similar orientation depending on the odd-even number of the CH_2 units, due to the zigzag structure of the carbon chain. Therefore, the SAMs with longer carbon chains are predictable based on the results for SAMs with shorter carbon chains, saving a huge amount of computational time.

The approaches of MD simulations and the analyzation of the angles of the SAMs discussed in Chapter 6 can be utilized for organic SAMs and are expected to provide guidance for the design of SAMs with specific properties.

References

[1] Aasberg-Petersen, K., Dybkjær, I., Ovesen, C. V., Schjødt, N. C., Sehested, J., & Thomsen, S. G. (2011). Natural gas to synthesis gas–catalysts and catalytic processes. *Journal of Natural gas science and engineering*, *3*(2), 423-459.

[2] Rostrup-Nielsen, J. R. (2002). Syngas in perspective. *Catalysis today*, *71*(3-4), 243-247.

[3] Enger, B. C., Lødeng, R., & Holmen, A. (2008). A review of catalytic partial oxidation of methane to synthesis gas with emphasis on reaction mechanisms over transition metal catalysts. *Applied Catalysis A: General*, *346*(1-2), 1-27.

[4] Bradford, M. C. J., & Vannice, M. A. (1999). CO2 reforming of CH4. *Catalysis Reviews*, *41*(1), 1-42.

[5] Keller, G. E., & Bhasin, M. M. (1982). Synthesis of ethylene via oxidative coupling of methane: I. Determination of active catalysts. *Journal of Catalysis*, *73*(1), 9-19.

[6] Hinsen, W., & Baerns, M. (1983). Oxidative Coupling of Methane to C2 Hydrocarbons in the Presence of Different Catalysts. *ChemInform, 14*.

[7] Zavyalova, U., Holena, M., Schlögl, R., & Baerns, M. (2011). Statistical analysis of past catalytic data on oxidative methane coupling for new insights into the composition of high-performance catalysts. *ChemCatChem*, *3*(12), 1935-1947.

[8] Olah, G. A., Gupta, B., Felberg, J. D., Ip, W. M., Husain, A., Karpeles, R., Lammertsma, K., Melhotra A. K., & Trivedi, N. J. (1985). Electrophilic reactions at

single bonds. 20. Selective monohalogenation of methane over supported acidic or platinum metal catalysts and hydrolysis of methyl halides over. gamma.-alumina-supported metal oxide/hydroxide catalysts. A feasible path for the oxidative conversion of methane into methyl alcohol/dimethyl ether. *Journal of the American Chemical Society*, *107*(24), 7097-7105.

[9] Sajith, P. K., Staykov, A., Yoshida, M., Shiota, Y., & Yoshizawa, K. (2020). Theoretical study of the direct conversion of methane to methanol using H2O2 as an oxidant on Pd and Au/Pd surfaces. *The Journal of Physical Chemistry C*, *124*(24), 13231-13239.

[10] Smeets, P. J., Woertink, J. S., Sels, B. F., Solomon, E. I., & Schoonheydt, R. A. (2010). Transition-metal ions in zeolites: coordination and activation of oxygen. *Inorganic chemistry*, *49*(8), 3573-3583.

[11] Groothaert, M. H., Smeets, P. J., Sels, B. F., Jacobs, P. A., & Schoonheydt, R. A. (2005). Selective oxidation of methane by the bis (μ-oxo) dicopper core stabilized on ZSM-5 and mordenite zeolites. *Journal of the American Chemical Society*, *127*(5), 1394-1395.

[12] Dinh, K. T., Sullivan, M. M., Narsimhan, K., Serna, P., Meyer, R. J., Dincă, M., & Román-Leshkov, Y. (2019). Continuous partial oxidation of methane to methanol catalyzed by diffusion-paired copper dimers in copper-exchanged zeolites. *Journal of the American Chemical Society*, *141*(29), 11641-11650.

[13] Muñoz Gandarillas, A. E., Van Geem, K. M., Reyniers, M. F., & Marin, G. B. (2014). Influence of the reactor material composition on coke formation during ethane steam cracking. *Industrial & Engineering Chemistry Research*, *53*(15), 6358-6371.

[14] Oyama, S. T., & Somorjai, G. A. (1990). Effect of structure in selective oxide catalysis: oxidation reactions of ethanol and ethane on vanadium oxide. *Journal of Physical Chemistry*, *94*(12), 5022-5028.

[15] Le Bars, J., Vedrine, J. C., Auroux, A., Pommier, B., & Pajonk, G. M. (1992). Calorimetric study of vanadium pentoxide catalysts used in the reaction of ethane oxidative dehydrogenation. *The Journal of Physical Chemistry*, *96*(5), 2217-2221.

[16] Heracleous, E., & Lemonidou, A. A. (2006). Ni–Nb–O mixed oxides as highly active and selective catalysts for ethene production via ethane oxidative dehydrogenation. Part I: Characterization and catalytic performance. *Journal of Catalysis*, *237*(1), 162-174.

[17] Skoufa, Z., Heracleous, E., & Lemonidou, A. A. (2015). On ethane ODH mechanism and nature of active sites over NiO-based catalysts via isotopic labeling and methanol sorption studies. *Journal of Catalysis*, *322*, 118-129.

[18] Sabatier, P. (1920). *La catalyse en chimie organique*. Paris et Liege: Librairie polytechnique.

[19] Shetty, M., Walton, A., Gathmann, S. R., Ardagh, M. A., Gopeesingh, J., Resasco, J., & Dauenhauer, P. J. (2020). The catalytic mechanics of dynamic surfaces:

stimulating methods for promoting catalytic resonance. *ACS Catalysis*, *10*(21), 12666-12695.

[20] Gopeesingh, J., Ardagh, M. A., Shetty, M., Burke, S. T., Dauenhauer, P. J., & Abdelrahman, O. A. (2020). Resonance-promoted formic acid oxidation via dynamic electrocatalytic modulation. *ACS Catalysis*, *10*(17), 9932-9942.

[21] *Self Assembled Monolayers*, https://www.gelest.com/applications/self-assembled-monolayers/

[22] Schwartz, D. K. (2001). Mechanisms and kinetics of self-assembled monolayer formation. *Annual review of physical chemistry*, *52*(1), 107-137.

[23] Schreiber, F. (2000). Structure and growth of self-assembling monolayers. *Progress in surface science*, *65*(5-8), 151-257.

[24] Laibinis, P. E., Whitesides, G. M., Allara, D. L., Tao, Y. T., Parikh, A. N., & Nuzzo, R. G. (1991). Comparison of the structures and wetting properties of self-assembled monolayers of n-alkanethiols on the coinage metal surfaces, copper, silver, and gold. *Journal of the American Chemical Society*, *113*(19), 7152-7167.

[25] Chaki, N. K., & Vijayamohanan, K. (2002). Self-assembled monolayers as a tunable platform for biosensor applications. *Biosensors and Bioelectronics*, *17*(1-2), 1-12.

[26] Segev, L., Salomon, A., Natan, A., Cahen, D., Kronik, L., Amy, F., Chan, C. K., & Kahn, A. (2006). Electronic structure of Si (111)-bound alkyl monolayers: Theory and experiment. *Physical Review B*, *74*(16), 165323.

[27] Yu, H., Webb, L. J., Heath, J. R., & Lewis, N. S. (2006). Scanning tunneling spectroscopy of methyl-and ethyl-terminated Si (111) surfaces. *Applied physics letters*, *88*(25), 252111.

[28] Arefi, H. H. (2015). *A microscopic study of structural and electronic properties of functionalized silicon surfaces based on first-principles* (Doctoral dissertation, University College Cork).

[29] Tao, F., & Bernasek, S. L. (2007). Understanding odd− even effects in organic self-assembled monolayers. *Chemical reviews*, *107*(5), 1408-1453.

[30] Arefi, H. H., Nolan, M., & Fagas, G. (2015). Role of the Head and/or Tail Groups of Adsorbed−[Xhead group]–Alkyl–[Xtail group][X= O (H), S (H), NH (2)] Chains in Controlling the Work Function of the Functionalized H: Si (111) Surface. *The Journal of Physical Chemistry C*, *119*(21), 11588-11597.

[31] Zenasni, O., Marquez, M. D., Jamison, A. C., Lee, H. J., Czader, A., & Lee, T. R. (2015). Inverted Surface Dipoles in Fluorinated Self-Assembled Monolayers. *Chemistry of Materials*, *27*(21), 7433-7446.

[32] Marquez, M. D., Zenasni, O., Rodriguez, D., Yu, T., Sakunkaewkasem, S., Toro Figueira, F., Czader, A., Baldelli, S., & Lee, T. R. (2019). Burying the Inverted Surface Dipole: Self-Assembled Monolayers Derived from Alkyl-Terminated Partially Fluorinated Alkanethiols. *Chemistry of Materials*, *32*(3), 953-968.

[33] Kohn, W. (1999). Nobel Lecture: Electronic structure of matter—wave functions and density functionals. *Reviews of Modern Physics*, *71*(5), 1253.

[34] Burke, K. (2012). Perspective on density functional theory. *The Journal of chemical physics*, *136*(15), 150901.

[35] Freeman, A. J., & Wimmer, E. (1995). Density functional theory as a major tool in computational materials science. *Annual Review of Materials Science*, *25*(1), 7-36.

[36] Sholl, D., & Steckel, J. A. (2011). *Density functional theory: a practical introduction*. John Wiley & Sons.

[37] Lusk, M. T., & Mattsson, A. E. (2011). High-performance computing for materials design to advance energy science. *MRS Bulletin*, *36*(3), 169-174.

[38] Kohn, W., & Sham, L. J. (1965). Self-consistent equations including exchange and correlation effects. *Physical review*, *140*(4A), A1133.

[39] Hammer, B. H. L. B., Hansen, L. B., & Nørskov, J. K. (1999). Improved adsorption energetics within density-functional theory using revised Perdew-Burke-Ernzerhof functionals. *Physical review B*, *59*(11), 7413.

[40] Cohen, A. J., & Handy, N. C. (2000). Assessment of exchange correlation functionals. *Chemical Physics Letters*, *316*(1-2), 160-166.

[41] Wellendorff, J., Lundgaard, K. T., Møgelhøj, A., Petzold, V., Landis, D. D., Nørskov, J. K., Bligaard, T., & Jacobsen, K. W. (2012). Density functionals for surface science: Exchange-correlation model development with Bayesian error estimation. *Physical Review B*, *85*(23), 235149.

[42] Kresse, G., & Furthmüller, J. (1996). Efficient iterative schemes for ab initio total-energy calculations using a plane-wave basis set. *Physical review B*, *54*(16), 11169.

[43] Kresse, G., & Furthmüller, J. (1996). Efficiency of ab-initio total energy calculations for metals and semiconductors using a plane-wave basis set. *Computational materials science*, *6*(1), 15-50.

[44] Henkelman, G., Uberuaga, B. P., & Jónsson, H. (2000). A climbing image nudged elastic band method for finding saddle points and minimum energy paths. *The Journal of chemical physics*, *113*(22), 9901-9904.

[45] Henkelman, G., & Jónsson, H. (2000). Improved tangent estimate in the nudged elastic band method for finding minimum energy paths and saddle points. *The Journal of chemical physics*, *113*(22), 9978-9985.

[46] *Nudged Elastic Band (NEB),* https://www.scm.com/doc/AMS/Tasks/NEB.html

[47] Henkelman, G., & Jónsson, H. (1999). A dimer method for finding saddle points on high dimensional potential surfaces using only first derivatives. *The Journal of chemical physics*, *111*(15), 7010-7022.

[48] Frenkel, D., & Smit, B. (2001). *Understanding molecular simulation: from algorithms to applications* (Vol. 1). Elsevier.

[49] Hoover, W. G., Ladd, A. J., & Moran, B. (1982). High-strain-rate plastic flow studied via nonequilibrium molecular dynamics. *Physical Review Letters*, *48*(26), 1818.

[50] Nosé, S. (1984). A molecular dynamics method for simulations in the canonical ensemble. *Molecular physics*, *52*(2), 255-268.

[51] Andersen, H. C. (1980). Molecular dynamics simulations at constant pressure and/or temperature. *The Journal of chemical physics*, *72*(4), 2384-2393.

[52] Kühne, T. D., Iannuzzi, M., Del Ben, M., Rybkin, V. V., Seewald, P., Stein, F., Laino, T., Khaliullin, R. Z., Schütt, O., Schiffmann, F., Golze, D., Wilhelm, J., Chulkov, S., Bani Hashemian, M. H., Weber, V., Borštnik, U., Taillefumier, M., Jakobovits, A. S., Lazzaro, A., Pabst, H., Müller, T., Schade, R., Guidon, M., Andermatt, S., Holmberg, N., Schenter, G. K., Hehn, A., Bussy, A., Belleflamme, F., Tabacchi, G., Glöß, A., Lass, M., Bethune, I., Mundy, C. J., Plessl, C., Watkins, M., VandeVondele, H., Krack, M., & Hutter, J. (2020). CP2K: An electronic structure and molecular dynamics software package-Quickstep: Efficient and accurate electronic structure calculations. *The Journal of Chemical Physics*, *152*(19), 194103.

[53] *Annual Energy Outlook 2021;* www.eia.gov/outlooks/aeo/.

[54] Pakhare, D., & Spivey, J. (2014). A review of dry (CO 2) reforming of methane over noble metal catalysts. *Chemical Society Reviews*, *43*(22), 7813-7837.

[55] Sehested, J., Gelten, J. A., Remediakis, I. N., Bengaard, H., & Nørskov, J. K. (2004). Sintering of nickel steam-reforming catalysts: effects of temperature and steam and hydrogen pressures. *Journal of Catalysis*, *223*(2), 432-443.

[56] Ahmed, K., & Foger, K. (2000). Kinetics of internal steam reforming of methane on Ni/YSZ-based anodes for solid oxide fuel cells. *Catalysis today*, *63*(2-4), 479-487.

[57] Supat, K., Chavadej, S., Lobban, L. L., & Mallinson, R. G. (2003). Combined steam reforming and partial oxidation of methane to synthesis gas under electrical discharge. *Industrial & engineering chemistry research*, *42*(8), 1654-1661.

[58] Kulkarni, A. R., Zhao, Z. J., Siahrostami, S., Nørskov, J. K., & Studt, F. (2018). Cation-exchanged zeolites for the selective oxidation of methane to methanol. *Catalysis Science & Technology*, *8*(1), 114-123.

[59] Engedahl, U., Grönbeck, H., & Hellman, A. (2019). First-Principles Study of Oxidation State and Coordination of Cu-Dimers in Cu-SSZ-13 during Methane-to-Methanol Reaction Conditions. *The Journal of Physical Chemistry C*, *123*(43), 26145-26150.

[60] Engedahl, U., Arvidsson, A. A., Grönbeck, H., & Hellman, A. (2021). Reaction Mechanism for Methane-to-Methanol in Cu-SSZ-13: First-Principles Study of the Z2 [Cu2O] and Z2 [Cu2OH] Motifs. *Catalysts*, *11*(1), 17.

[61] Hammond, C., Forde, M. M., Ab Rahim, M. H., Thetford, A., He, Q., Jenkins, R. L., Dimitratos, N., Lopez-Sanchez, J. A., Dummer, N. F., Murphy, D. M., Carley, A. F., Taylor, S. H., Willock, D. J., Stangland, E. E., Kang, J., Hagen, H., Kiely, C. J., & Hutchings, G. J. (2012). Direct catalytic conversion of methane to methanol in an aqueous medium by using copper-promoted Fe-ZSM-5. *Angewandte Chemie*, *124*(21), 5219-5223.

[62] Spinner, N., & Mustain, W. E. (2013). Electrochemical methane activation and conversion to oxygenates at room temperature. *ECS Transactions*, *53*(23), 1.

[63] Omasta, T. J., Rigdon, W. A., Lewis, C. A., Stanis, R. J., Liu, R., Fan, C. Q., & Mustain, W. E. (2015). Two pathways for near room temperature electrochemical conversion of methane to methanol. *ECS Transactions*, *66*(8), 129.

[64] Meloni, E., Martino, M., & Palma, V. (2020). A short review on Ni based catalysts and related engineering issues for methane steam reforming. *Catalysts*, *10*(3), 352.

[65] Von Barth, U., & Hedin, L. (1972). A local exchange-correlation potential for the spin polarized case. i. *Journal of Physics C: Solid State Physics*, *5*(13), 1629.

[66] Methfessel, M. P. A. T., & Paxton, A. T. (1989). High-precision sampling for Brillouin-zone integration in metals. *Physical Review B*, *40*(6), 3616.

[67] Patton, D. C., Porezag, D. V., & Pederson, M. R. (1997). Simplified generalized-gradient approximation and anharmonicity: Benchmark calculations on molecules. *Physical Review B*, *55*(12), 7454.

[68] Blöchl, P. E. (2000). First-principles calculations of defects in oxygen-deficient silica exposed to hydrogen. *Physical Review B*, *62*(10), 6158.

[69] Dudarev, S. L., Botton, G. A., Savrasov, S. Y., Humphreys, C. J., & Sutton, A. P. (1998). Electron-energy-loss spectra and the structural stability of nickel oxide: An LSDA+ U study. *Physical Review B*, *57*(3), 1505.

[70] Wang, L., Maxisch, T., & Ceder, G. (2006). Oxidation energies of transition metal oxides within the GGA+ U framework. *Physical Review B*, *73*(19), 195107.

[71] Peng, G., Merte, L. R., Knudsen, J., Vang, R. T., Lægsgaard, E., Besenbacher, F., & Mavrikakis, M. (2010). On the mechanism of low-temperature CO oxidation on Ni (111) and NiO (111) surfaces. *The Journal of Physical Chemistry C*, *114*(49), 21579-21584.

[72] Rohrbach, A., & Hafner, J. (2005). Molecular adsorption of NO on NiO (100): DFT and DFT+ U calculations. *Physical Review B*, *71*(4), 045405.

[73] Larsen, A. H., Mortensen, J. J., Blomqvist, J., Castelli, I. E., Christensen, R., Dułak, M., Friis, J., Groves, M. N., Hammer, B., Hargus, C., Hermes, E. D., Jennings, P. C., Jensen, P. B., Kermode, J., Kitchin, J. R., Kolsbjerg, E. L., Kubal, J., Kaasbjerg,K., Lysgaard, S., Maronsson, J., B., Maxson, T., Olsen, T., Pastewka, L., Peterson, A., Rostgaard, C., Schiøtz, J., Schütt, O., Strange, M., Thygesen, K. S., Vegge, T., Vilhelmsen, L., Walter, M., Zeng, Z., & Jacobsen, K. W. (2017). The atomic simulation environment—a Python library for working with atoms. *Journal of Physics: Condensed Matter*, *29*(27), 273002.

[74] Phatak, A. A., Delgass, W. N., Ribeiro, F. H., & Schneider, W. F. (2009). Density functional theory comparison of water dissociation steps on Cu, Au, Ni, Pd, and Pt. *The Journal of Physical chemistry c*, *113*(17), 7269-7276.

[75] Liu, H., Yan, R., Zhang, R., Wang, B., & Xie, K. (2011). A DFT theoretical study of CH4 dissociation on gold-alloyed Ni (111) surface. *Journal of natural gas chemistry*, *20*(6), 611-617.

[76] Che, F., Zhang, R., Hensley, A. J., Ha, S., & McEwen, J. S. (2014). Density functional theory studies of methyl dissociation on a Ni (111) surface in the presence of an external electric field. *Physical Chemistry Chemical Physics*, *16*(6), 2399-2410.

[77] Xu, Y., Fan, C., Zhu, Y. A., Li, P., Zhou, X. G., Chen, D., & Yuan, W. K. (2012). Effect of Ag on the control of Ni-catalyzed carbon formation: A density functional theory study. *Catalysis today*, *186*(1), 54-62.

[78] Mook, H. A. (1966). Magnetic moment distribution of nickel metal. *Physical Review*, *148*(2), 495.

[79] Towler, M. D., Allan, N. L., Harrison, N. M., Saunders, V. R., Mackrodt, W. C., & Apra, E. (1994). Ab initio study of MnO and NiO. *Physical Review B*, *50*(8), 5041.

[80] Huang, H. M., Luo, S. J., & Yao, K. L. (2010). First-principles study of the stability and the electronic structure of NiO/MgO interface. *Computational materials science*, *50*(1), 198-202.

[81] Che, F., Ha, S., & McEwen, J. S. (2016). Elucidating the field influence on the energetics of the methane steam reforming reaction: A density functional theory study. *Applied Catalysis B: Environmental*, *195*, 77-89.

[82] Wang, S. G., Cao, D. B., Li, Y. W., Wang, J., & Jiao, H. (2005). Chemisorption of CO2 on nickel surfaces. *The Journal of Physical Chemistry B*, *109*(40), 18956-18963.

[83] Kubicki, J. D., Kwon, K. D., Paul, K. W., & Sparks, D. L. (2007). Surface complex structures modelled with quantum chemical calculations: carbonate,

phosphate, sulphate, arsenate and arsenite. *European journal of soil science*, *58*(4), 932-944.

[84] Chanchlani, K. G., Hudgins, R. R., & Silveston, P. L. (1992). Methanol synthesis from H2, CO, and C02 over Cu/ZnO catalysts. *Journal of Catalysis*, *136*(1), 59-75.

[85] Ma, Y., Ge, Q., Li, W., & Xu, H. (2009). Methanol synthesis from sulfur-containing syngas over Pd/CeO2 catalyst. *Applied Catalysis B: Environmental*, *90*(1-2), 99-104.

[86] Liu, L., Lin, Z., Lin, S., Chen, Y., Zhang, L., Chen, S., Zhang, X., Lin, J., Zhang, Z., Wan, S., & Wang, Y. (2021). Conversion of syngas to methanol and DME on highly selective Pd/ZnAl2O4 catalyst. *Journal of Energy Chemistry*, *58*, 564-572.

[87] Li, X. (2020). *Prediction of acid site evolution and distribution using first-principles kinetic Monte Carlo and Genetic Algorithms: Implications for catalytic hydrotreating of biomass* (Doctoral dissertation).

[88] Latimer, A. A., Kulkarni, A. R., Aljama, H., Montoya, J. H., Yoo, J. S., Tsai, C., Abild-Pedersen, F., Studt, F. & Nørskov, J. K. (2017). Understanding trends in C–H bond activation in heterogeneous catalysis. *Nature materials*, *16*(2), 225-229.

[89] Huang, X., & Groves, J. T. (2017). Beyond ferryl-mediated hydroxylation: 40 years of the rebound mechanism and C–H activation. *JBIC Journal of Biological Inorganic Chemistry*, *22*(2-3), 185-207.

[90] Simons, M. C., Prinslow, S. D., Babucci, M., Hoffman, A. S., Hong, J., Vitillo, J. G., Bare, S. R., Gates, B. C. Lu, C. C., Gagliardi, L., & Bhan, A. (2021). Beyond

Radical Rebound: Methane Oxidation to Methanol Catalyzed by Iron Species in Metal–Organic Framework Nodes. *Journal of the American Chemical Society*, *143*(31), 12165-12174.

[91] Crabtree, R. H. (1995). Aspects of methane chemistry. *Chemical Reviews*, *95*(4), 987-1007.

[92] Lunsford, J. H. (2000). Catalytic conversion of methane to more useful chemicals and fuels: a challenge for the 21st century. *Catalysis today*, *63*(2-4), 165-174.

[93] Schwarz, H. (2011). Chemistry with methane: concepts rather than recipes. *Angewandte Chemie International Edition*, *50*(43), 10096-10115.

[94] Llorca, J., Casanovas, A., Domínguez, M., Casanova, I., Angurell, I., Seco, M., & Rossell, O. (2008). Plasma-activated core-shell gold nanoparticle films with enhanced catalytic properties. *Journal of Nanoparticle Research*, *10*(3), 537-542.

[95] Mowbray, D. J., Migani, A., Walther, G., Cardamone, D. M., & Rubio, A. (2013). Gold and methane: A noble combination for delicate oxidation. *The Journal of Physical Chemistry Letters*, *4*(17), 3006-3012.

[96] Psofogiannakis, G., St-Amant, A., & Ternan, M. (2006). Methane oxidation mechanism on Pt (111): a cluster model DFT study. *The Journal of Physical Chemistry B*, *110*(48), 24593-24605.

[97] Murray, E. P., Tsai, T., & Barnett, S. A. (1999). A direct-methane fuel cell with a ceria-based anode. *Nature*, *400*(6745), 649-651.

[98] Park, S., Vohs, J. M., & Gorte, R. J. (2000). Direct oxidation of hydrocarbons in a solid-oxide fuel cell. *Nature*, *404*(6775), 265-267.

[99] Che, F., Gray, J. T., Ha, S., & McEwen, J. S. (2017). Improving Ni catalysts using electric fields: a DFT and experimental study of the methane steam reforming reaction. *ACS Catalysis*, *7*(1), 551-562.

[100] Neugebauer, J., & Scheffler, M. (1992). Adsorbate-substrate and adsorbate-adsorbate interactions of Na and K adlayers on Al (111). *Physical Review B*, *46*(24), 16067.

[101] Momma, K., & Izumi, F. (2008). VESTA: a three-dimensional visualization system for electronic and structural analysis. *Journal of Applied crystallography*, *41*(3), 653-658.

[102] Che, F., Gray, J. T., Ha, S., & McEwen, J. S. (2015). Catalytic water dehydrogenation and formation on nickel: Dual path mechanism in high electric fields. *Journal of Catalysis*, *332*, 187-200.

[103] Moro-oka, Y. (1998). Reactivities of active oxygen species and their roles in the catalytic oxidation of inactive hydrocarbon. *Catalysis today*, *45*(1-4), 3-12.

[104] Kondratenko, E. V. (2011). Mechanistic Aspects of Short Contact Time Oxidative Functionalization of Propane and Ethane from Temporal Analysis of Products. In *Nanostructured Catalysts* (pp. 340-354).

[105] Bukhtiyarov, V. I., Hävecker, M., Kaichev, V. V., Knop-Gericke, A., Mayer, R. W., & Schlögl, R. (2001). X-ray absorption and photoemission studies of the active oxygen for ethylene epoxidation over silver. *Catalysis letters*, *74*(3), 121-125.

[106] Panov, G. I., Uriarte, A. K., Rodkin, M. A., & Sobolev, V. I. (1998). Generation of active oxygen species on solid surfaces. Opportunity for novel oxidation technologies over zeolites. *Catalysis Today*, *41*(4), 365-385.

[107] Starokon, E. V., Parfenov, M. V., Pirutko, L. V., Abornev, S. I., & Panov, G. I. (2011). Room-temperature oxidation of methane by α-oxygen and extraction of products from the FeZSM-5 surface. *The Journal of Physical Chemistry C*, *115*(5), 2155-2161.

[108] Dubkov, K. A., Sobolev, V. I., Talsi, E. P., Rodkin, M. A., Watkins, N. H., Shteinman, A. A., & Panov, G. I. (1997). Kinetic isotope effects and mechanism of biomimetic oxidation of methane and benzene on FeZSM-5 zeolite. *Journal of Molecular Catalysis A: Chemical*, *123*(2-3), 155-161.

[109] Ward, M. B., Lin, M. J., & Lunsford, J. H. (1977). The oxidative dehydrogenation of ethane by nitrous oxide over molybdenum oxide supported on silica gel. *Journal of Catalysis*, *50*(2), 306-318.

[110] Aika, K., & Lunsford, J. H. (1977). Surface reactions of oxygen ions. I. Dehydrogenation of alkanes by oxygen (1-) ions on magnesium oxide. *The Journal of Physical Chemistry*, *81*(14), 1393-1398.

[111] Shvets, V. A., & Kazansky, V. B. (1972). Oxygen anion-radicals adsorbed on supported oxide catalysts containing Ti, V and Mo ions. *Journal of Catalysis*, *25*(1), 123-130.

[112] Bielański, A., & Najbar, M. (1972). Adsorption species of oxygen on the surfaces of transition metal oxides. *Journal of Catalysis*, *25*(3), 398-406.

[113] Panov, G. I., Dubkov, K. A., & Starokon, E. V. (2006). Active oxygen in selective oxidation catalysis. *Catalysis today*, *117*(1-3), 148-155.

[114] Bielański, A., & Haber, J. (1979). Oxygen in catalysis on transition metal oxides. *Catalysis Reviews Science and Engineering*, *19*(1), 1-41.

[115] Williams, O. C., & Sievers, C. (2021). Active oxygen species in heterogeneously catalyzed oxidation reactions. *Applied Catalysis A: General*, 118057.

[116] Heracleous, E., & Lemonidou, A. A. (2006). Ni–Nb–O mixed oxides as highly active and selective catalysts for ethene production via ethane oxidative dehydrogenation. Part I: Characterization and catalytic performance. *Journal of Catalysis*, *237*(1), 162-174.

[117] Popescu, I., Skoufa, Z., Heracleous, E., Lemonidou, A., & Marcu, I. C. (2015). A study by electrical conductivity measurements of the semiconductive and redox properties of Nb-doped NiO catalysts in correlation with the oxidative dehydrogenation of ethane. *Physical Chemistry Chemical Physics*, *17*(12), 8138-8147.

[118] Heracleous, E., & Lemonidou, A. A. (2010). Ni–Me–O mixed metal oxides for the effective oxidative dehydrogenation of ethane to ethylene–Effect of promoting metal Me. *Journal of Catalysis*, *270*(1), 67-75.

[119] Varghese, J. J., & Mushrif, S. H. (2017). Insights into the C–H bond activation on NiO surfaces: The role of nickel and oxygen vacancies and of low valent dopants on the reactivity and energetics. *The Journal of Physical Chemistry C*, *121*(33), 17969-17981.

[120] Delgado, D., Solsona, B., Ykrelef, A., Rodríguez-Gómez, A., Caballero, A., Rodríguez-Aguado, E., Rodríguez-Castellón, E., & López Nieto, J. M. (2017). Redox and catalytic properties of promoted NiO catalysts for the oxidative dehydrogenation of ethane. *The Journal of Physical Chemistry C*, *121*(45), 25132-25142.

[121] Zhao, X., Susman, M. D., Rimer, J. D., & Bollini, P. (2021). Tuning selectivity in nickel oxide-catalyzed oxidative dehydrogenation of ethane through control over non-stoichiometric oxygen density. *Catalysis Science & Technology*, *11*(2), 531-541.

[122] Schneider, W. F. (2004). Qualitative differences in the adsorption chemistry of acidic (CO2, SO x) and amphiphilic (NO x) species on the alkaline earth oxides. *The Journal of Physical Chemistry B*, *108*(1), 273-282.

[123] Lavalley, J. C. (1996). Infrared spectrometric studies of the surface basicity of metal oxides and zeolites using adsorbed probe molecules. *Catalysis Today*, *27*(3-4), 377-401.

[124] Pacchioni, G., Ricart, J. M., & Illas, F. (1994). Ab initio cluster model calculations on the chemisorption of CO2 and SO2 probe molecules on MgO and CaO (100) surfaces. A theoretical measure of oxide basicity. *Journal of the American Chemical Society*, *116*(22), 10152-10158.

[125] Jensen, M. B., Pettersson, L. G., Swang, O., & Olsbye, U. (2005). CO2 sorption on MgO and CaO surfaces: A comparative quantum chemical cluster study. *The Journal of Physical Chemistry B*, *109*(35), 16774-16781.

[126] Cornu, D., Guesmi, H., Krafft, J. M., & Lauron-Pernot, H. (2012). Lewis acido-basic interactions between CO2 and MgO surface: DFT and DRIFT approaches. *The Journal of Physical Chemistry C*, *116*(11), 6645-6654.

[127] Busca, G., & Lorenzelli, V. (1982). Infrared spectroscopic identification of species arising from reactive adsorption of carbon oxides on metal oxide surfaces. *Materials Chemistry*, *7*(1), 89-126.

[128] Álvarez, A., Borges, M., Corral-Pérez, J. J., Olcina, J. G., Hu, L., Cornu, D., Huang, R., Stoian, D., & Urakawa, A. (2017). Cover Feature: CO2 Activation over Catalytic Surfaces (ChemPhysChem 22/2017). *ChemPhysChem*, *18*(22), 3087-3087.

[129] Auroux, A., & Gervasini, A. (1990). Microcalorimetric study of the acidity and basicity of metal oxide surfaces. *Journal of Physical Chemistry*, *94*(16), 6371-6379.

[130] Bhattacharyya, K., Danon, A., K. Vijayan, B., Gray, K. A., Stair, P. C., & Weitz, E. (2013). Role of the surface lewis acid and base sites in the adsorption of

CO2 on titania nanotubes and platinized titania nanotubes: an in situ FT-IR study. *The Journal of Physical Chemistry C*, *117*(24), 12661-12678.

[131] Langmuir, I. (1918). The adsorption of gases on plane surfaces of glass, mica and platinum. *Journal of the American Chemical society*, *40*(9), 1361-1403.

[132] Jaroniec, M., & Tóth, J. (1978). Adsorption of gas mixtures on heterogeneous solid surfaces. *Colloid and Polymer Science*, *256*(7), 690-695.

[133] Mathias, P. M., Kumar, R., Moyer, J. D., Schork, J. M., Srinivasan, S. R., Auvil, S. R., & Talu, O. (1996). Correlation of multicomponent gas adsorption by the dual-site Langmuir model. Application to nitrogen/oxygen adsorption on 5A-zeolite. *Industrial & engineering chemistry research*, *35*(7), 2477-2483.

[134] Kumar, A., Ropital, F., de Bruin, T., & Diawara, B. (2020). Effects of surface orientations of Cr2O3 on CO2 adsorption: A DFT approach. *Applied Surface Science*, *529*, 147127.

[135] Patrakeev, M. V., Leonidov, I. A., & Kozhevnikov, V. L. (2011). Applications of coulometric titration for studies of oxygen non-stoichiometry in oxides. *Journal of Solid State Electrochemistry*, *15*(5), 931-954.

[136] Karppinen, M., Yamauchi, H., Otani, S., Fujita, T., Motohashi, T., Huang, Y. H., & Fjellvåg, H. (2006). Oxygen nonstoichiometry in YBaCo4O7+ δ: large low-temperature oxygen absorption/desorption capability. *Chemistry of materials*, *18*(2), 490-494.

[137] Bielański, A., Dereń, J., Haber, J., & Słoczyński, J. (1962). Physico-chemical properties of alkali-and iron-doped nickel oxide. *Transactions of the Faraday Society*, *58*, 166-175.

[138] Chen, T., Li, W., Yu, C., Jin, R., & Xu, H. (2000). The importance of nonstoichiometric oxygen in NiO for the catalytic oxidative dehydrogenation of ethane. In *Studies in Surface Science and Catalysis* (Vol. 130, pp. 1847-1852). Elsevier.

[139] Lin, F., Nordlund, D., Weng, T. C., Sokaras, D., Jones, K. M., Reed, R. B., Gillaspie, D. T., Weir D. G. J., Moore, R. G., Dillon, A. C., Richards, R. M., & Engtrakul, C. (2013). Origin of electrochromism in high-performing nanocomposite nickel oxide. *ACS applied materials & interfaces*, *5*(9), 3643-3649.

[140] Niklasson, G. A., & Granqvist, C. G. (2007). Electrochromics for smart windows: thin films of tungsten oxide and nickel oxide, and devices based on these. *Journal of Materials Chemistry*, *17*(2), 127-156.

[141] Nolan, M., Elliott, S. D., Mulley, J. S., Bennett, R. A., Basham, M., & Mulheran, P. (2008). Electronic structure of point defects in controlled self-doping of the TiO 2 (110) surface: Combined photoemission spectroscopy and density functional theory study. *Physical Review B*, *77*(23), 235424.

[142] Ueno, A., Hochmuth, J. K., & Bennett, C. O. (1977). Interaction of CO2, CO, and NiO studied by infrared spectroscopy. *Journal of Catalysis*, *49*(2), 225-235.

[143] Myers, A. L., & Prausnitz, J. M. (1965). Thermodynamics of mixed-gas adsorption. *AIChE journal*, *11*(1), 121-127.

[144] Simon, C. M., Smit, B., & Haranczyk, M. (2016). pyIAST: Ideal adsorbed solution theory (IAST) Python package. *Computer Physics Communications*, *200*, 364-380.

[145] Al-Zahrani, S., Song, Q., & Lobban, L. L. (1994). Effects of carbon dioxide during oxidative coupling of methane over lithium/magnesia: mechanisms and models. *Industrial & engineering chemistry research*, *33*(2), 251-258.

[146] Galuszka, J. (1994). Carbon dioxide chemistry during oxidative coupling of methane on a Li/MgO catalyst. *Catalysis today*, *21*(2-3), 321-331.

[147] Wang, D., Xu, M., Shi, C., & Lunsford, J. H. (1993). Effect of carbon dioxide on the selectivities obtained during the partial oxidation of methane and ethane over Li+/MgO catalysts. *Catalysis letters*, *18*(4), 323-328.

[148] Stansch, Z., Mleczko, L., & Baerns, M. (1997). Comprehensive kinetics of oxidative coupling of methane over the La2O3/CaO catalyst. *Industrial & engineering chemistry research*, *36*(7), 2568-2579.

[149] Guan, C., Liu, Z., Wang, D., Zhou, X., Pang, Y., Yu, N., can Bavel, A. P., Vovk, E., & Yang, Y. (2021). Exploring the formation of carbonates on La 2 O 3 catalysts with OCM activity. *Catalysis Science & Technology*, *11*(19), 6516-6528.

[150] Guan, C., Yang, Y., Pang, Y., Liu, Z., Li, S., Vovk, E. I., Zhou, X., Li, J. P. H., Zhang, J., Yu, N., Long, L., Hao, J., & van Bavel, A. P. (2021). How CO2 poisons

La2O3 in an OCM catalytic reaction: A study by in situ XRD-MS and DFT. *Journal of Catalysis*, *396*, 202-214.

[151] Chu, C., Zhao, Y., Li, S., & Sun, Y. (2016). CO2 Chemisorption and Its Effect on Methane Activation in La2O3-Catalyzed Oxidative Coupling of Methane. *The Journal of Physical Chemistry C*, *120*(5), 2737-2746.

[152] Yao, Y.-F. Y., & Kummer, J. T. (1973). The Oxidation of Hydrocarbons and CO over Metal Oxides: I. NiO Crystals. *Journal of Catalysis, 28* (1), 124–138.

[153] Skoufa, Z., Heracleous, E., & Lemonidou, A. A. (2012). Unraveling the contribution of structural phases in Ni–Nb–O mixed oxides in ethane oxidative dehydrogenation. *Catalysis today*, *192*(1), 169-176.

[154] Chen, K., Khodakov, A., Yang, J., Bell, A. T., & Iglesia, E. (1999). Isotopic tracer and kinetic studies of oxidative dehydrogenation pathways on vanadium oxide catalysts. *Journal of Catalysis*, *186*(2), 325-333.

[155] Bronsted, J. N. (1928). Acid and Basic Catalysis. *Chemical Reviews*, *5*(3), 231-338.

[156] Evans, M. G., & Polanyi, M. (1938). Inertia and driving force of chemical reactions. *Transactions of the Faraday Society*, *34*, 11-24.

[157] Heracleous, E., & Lemonidou, A. A. (2006). Ni–Nb–O mixed oxides as highly active and selective catalysts for ethene production via ethane oxidative dehydrogenation. Part II: Mechanistic aspects and kinetic modeling. *Journal of Catalysis*, *237*(1), 175-189.

[158] Dinse, A., Schomäcker, R., & Bell, A. T. (2009). The role of lattice oxygen in the oxidative dehydrogenation of ethane on alumina-supported vanadium oxide. *Physical Chemistry Chemical Physics*, *11*(29), 6119-6124.

[159] Du Toit, F. J., Sanderson, R. D., Engelbrecht, W. J., & Wagener, J. B. (1995). The effect of surface fluorination on the wettability of high density polyethylene. *Journal of fluorine chemistry*, *74*(1), 43-48.

[160] Graupe, M., Takenaga, M., Koini, T., Colorado, R., & Lee, T. R. (1999). Oriented surface dipoles strongly influence interfacial wettabilities. *Journal of the American Chemical Society*, *121*(13), 3222-3223.

[161] Howard, J. A., Hoy, V. J., O'Hagan, D., & Smith, G. T. (1996). How good is fluorine as a hydrogen bond acceptor?. *Tetrahedron*, *52*(38), 12613-12622.

[162] Colorado Jr, R., & Lee, T. R. (2000). Physical organic probes of interfacial wettability reveal the importance of surface dipole effects. *Journal of Physical Organic Chemistry*, *13*(12), 796-807.

[163] Chaudhury, M. K. (1996). Interfacial interaction between low-energy surfaces. *Materials Science and Engineering: R: Reports*, *16*(3), 97-159.

[164] Moore, H. J., Colorado Jr, R., Lee, H. J., Jamison, A. C., & Lee, T. R. (2013). Synthesis, characterization, and relative stabilities of self-assembled monolayers on gold generated from bidentate n-alkyl xanthic acids. *Langmuir*, *29*(34), 10674-10683.

[165] Maeland, A., & Flanagan, T. B. (1964). Lattice spacings of gold–palladium alloys. *Canadian journal of physics*, *42*(11), 2364-2366.

[166] Hickman, J., & Mishin, Y. (2016). Temperature fluctuations in canonical systems: Insights from molecular dynamics simulations. *Physical Review B*, *94*(18), 184311.

[167] Dumesic, J. A., Rudd, D. F., Rudd, D. F., Aparicio, L. M., Rekoske, J. E., & Trevino, A. A. (1993). *The microkinetics of heterogeneous catalysis*. Wiley-Vch.

Appendix

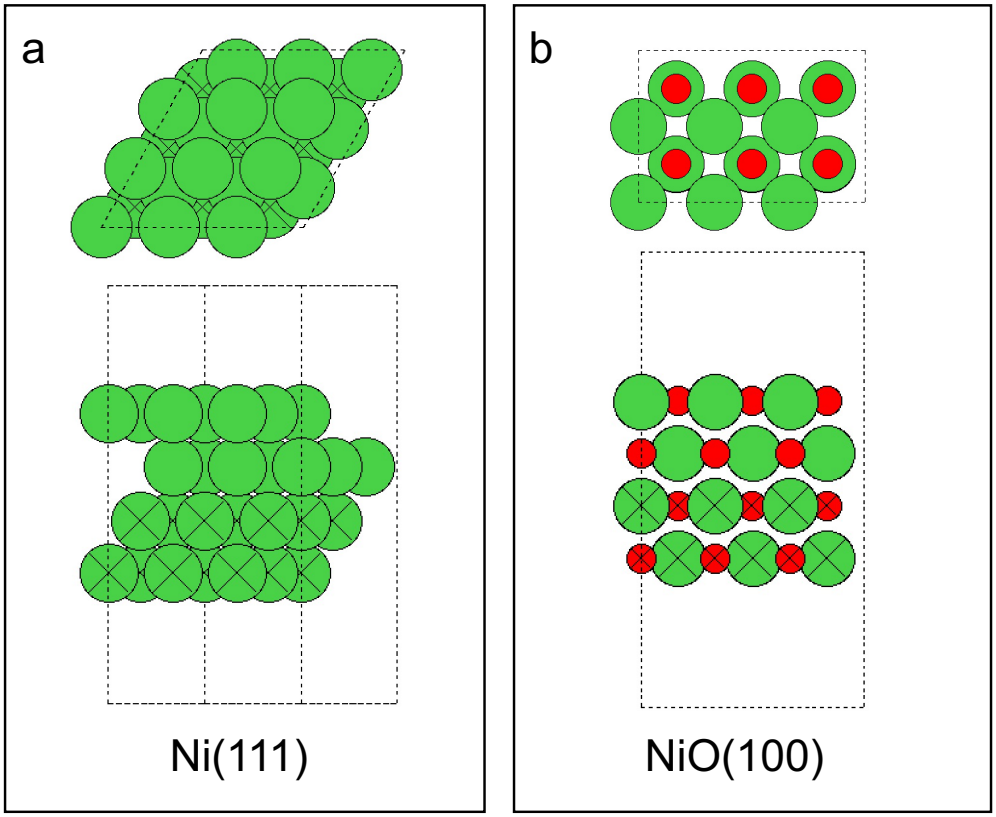

Figure A1. Top and side view of unit cell of Ni(111) (a) and NiO(100) (b). The green and red spheres represent nickel and oxygen atoms respectively.

Table A1. Reaction Enthalpy ΔH (eV) and Activation Barrier E_a (eV) of elementary steps of CO_3- and O-assisted methane conversion to methanol on Ni(111).

Reaction	Reaction Enthalpy ΔH (eV)	Activation Barrier E_a (eV)
$CH_4(g) + CO_3* + * \rightarrow CH_3* + HCO_3*$	0.19	1.32
$HCO_3* + * \rightarrow OH* + CO_2*$	-0.44	0.27
$CO_3* +* \rightarrow CO_2* + O*$	-0.82	0.16
$CH_4(g) + O* + * \rightarrow CH_3* + OH*$	0.56	1.94
$CH_3* + OH* \rightarrow CH_3OH* + *$	0.20	2.02

Table A2. Reaction Enthalpy ΔH (eV) and Activation Barrier E_a (eV) of elementary steps of CO_3-assisted and radical rebound mechanisms for methane conversion to methanol reaction on NiO(100).

Reaction	Reaction Enthalpy ΔH (eV)	Activation Barrier E_a (eV)
$CH_4(g) + CO_3* + * \rightarrow CH_3* + HCO_3*$	-1.66	1.17
$HCO_3* + *\rightarrow OH* + CO_2*$	0.56	0.69
$CH_3* + OH* \rightarrow CH_3OH* + *$	-1.12	1.74
$CO_3* +* \rightarrow CO_2* + O*$	0.20	0.44
$CH_4(gas) + O* \rightarrow CH_3(rad) + OH*$	0.14	0.50

Calculation of surface free energy of dry and hydroxylated NiO(100) surface

To estimate the thermal stability of NiO(100) with different water coverage, we corrected the gas-phase O_2 and H_2O and the temperature and pressure dependent chemical potential, or Gibbs free energy of the two gas phase species can be expressed as

$$\mu(T,p) = E_{DFT} + E_{ZPE} + \int_{oK}^{T} C_p dT - TS(T) + kT \ln\left(\frac{p}{p_0}\right), \quad \text{(A-1)}$$

where E_{DFT} (eV) is the electronic energy calculated from DFT, E_{ZPE} (eV) is the zero point energy, T (K) is temperature, the enthalpy and entropy corrections are calculated using the Shomate equation and the JANAF parameters for O_2 and H_2O, k is Boltzmann's constant, p (bar) is pressure and p_0 is the standard pressure as 1 bar. Thus, the temperature dependent enthalpy change can be calculated as

$$H^\circ - H^\circ{}_{298.15} = At + Bt^2/2 + Ct^3/3 + Dt^4/4 - E/t + F - H, \quad \text{(A-2)}$$

where $t = T/1000$. At $T = 0K$,

$$H^\circ{}_0 - H^\circ{}_{298.15} = F - H. \quad \text{(A-3)}$$

The entropy can be calculated as

$$S^\circ = A \ln t + Bt + Ct^2/2 + Dt^3/3 - E/(2t^2) + G. \quad \text{(A-4)}$$

The temperature and pressure dependent chemical potential change $\Delta\mu$ and the chemical potential of O_2 and H_2O μ can be calculated as

$$\Delta\mu = (H^\circ - H^\circ{}_{298.15}) - (H^\circ{}_0 - H^\circ{}_{298.15}) - S^\circ T \quad \text{(A-5)}$$

$$\text{and } \mu(T,p) = E_{DFT} + E_{ZPE} + \Delta\mu + kT \ln\left(\frac{p}{p_0}\right). \quad \text{(A-6)}$$

The chemical potential of O and H can then be calculated as

$$\mu_O = 0.5\mu_{O2} \tag{A-7}$$

$$\text{and } \mu_H = 0.5\mu_{H2O} - 0.25\mu_{O2}. \tag{A-8}$$

The Gibbs free energy of a hydroxylated surface can be expressed as

$$\Delta G = E - E_{ref} - n_H\mu_H - n_O\mu_O, \tag{A-9}$$

where E is the electronic energy of hydroxylated surface calculated from DFT, E_{ref} is the reference energy which is chosen to be the energy of dry NiO surface in this calculation, n_X is the extra number of H or O atom in the hydroxylated NiO compared to the dry NiO.

The partial pressure of O_2 was chosen to be 100 kPa as the reaction condition, and the partial pressure of H_2O was assumed to be 20 kPa. Calculation of dry and 1/3-, 1/2-, 2/3-, and 1-ML H_2O covered NiO were performed and the results are shown in Figure A2. The hydroxylated NiO surfaces are less stable as temperature increases and at the temperature range of reaction condition (the grey area in Figure A2) the dry NiO is the most stable surface, validating the use of dry NiO(100) for the investigation of the CO_2 adsorption and reaction thermodynamics.

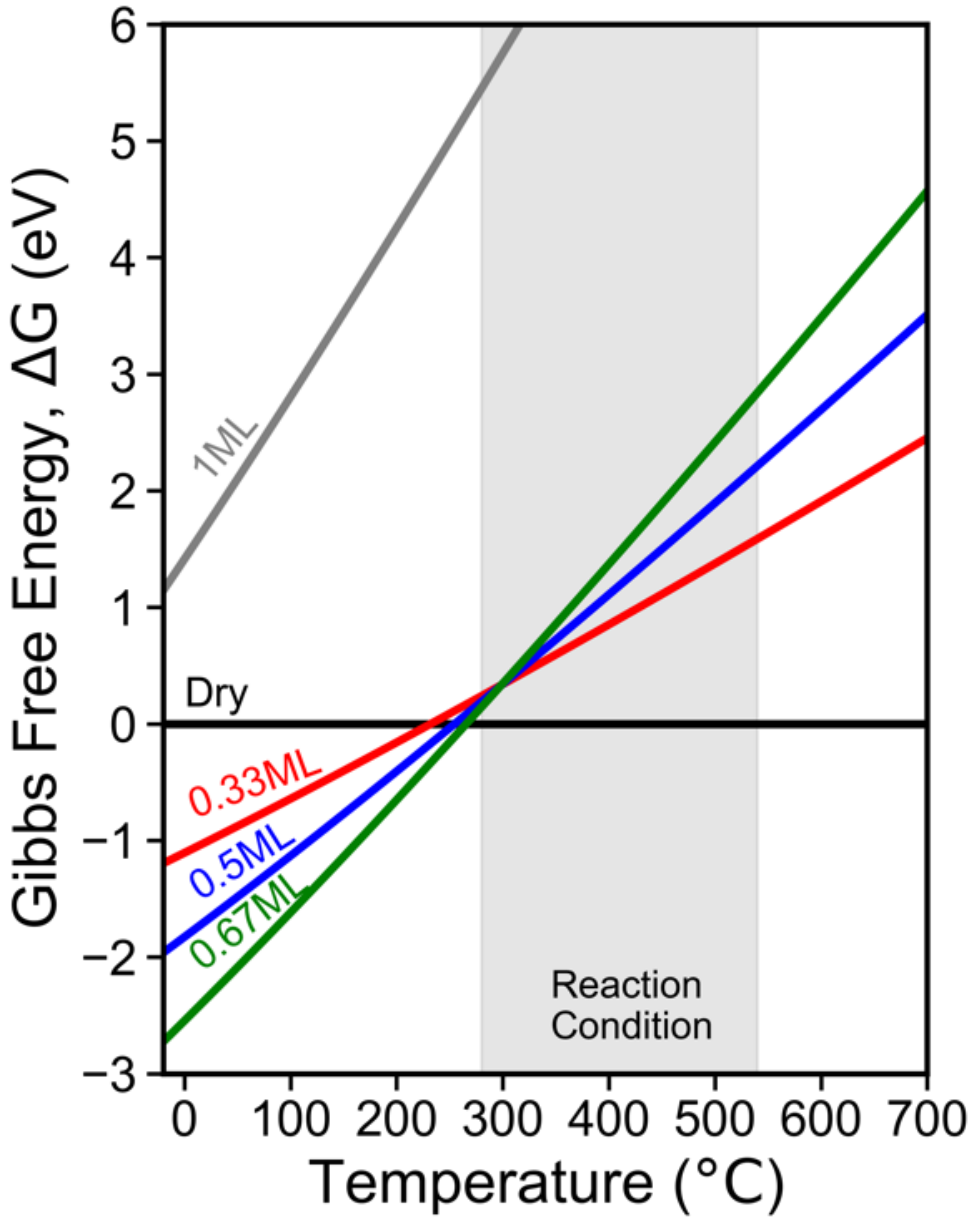

Figure A2. Gibbs free energy ΔG (eV) of dry and 1/3-, 1/2-, 2/3-, and 1-ML H_2O covered NiO.

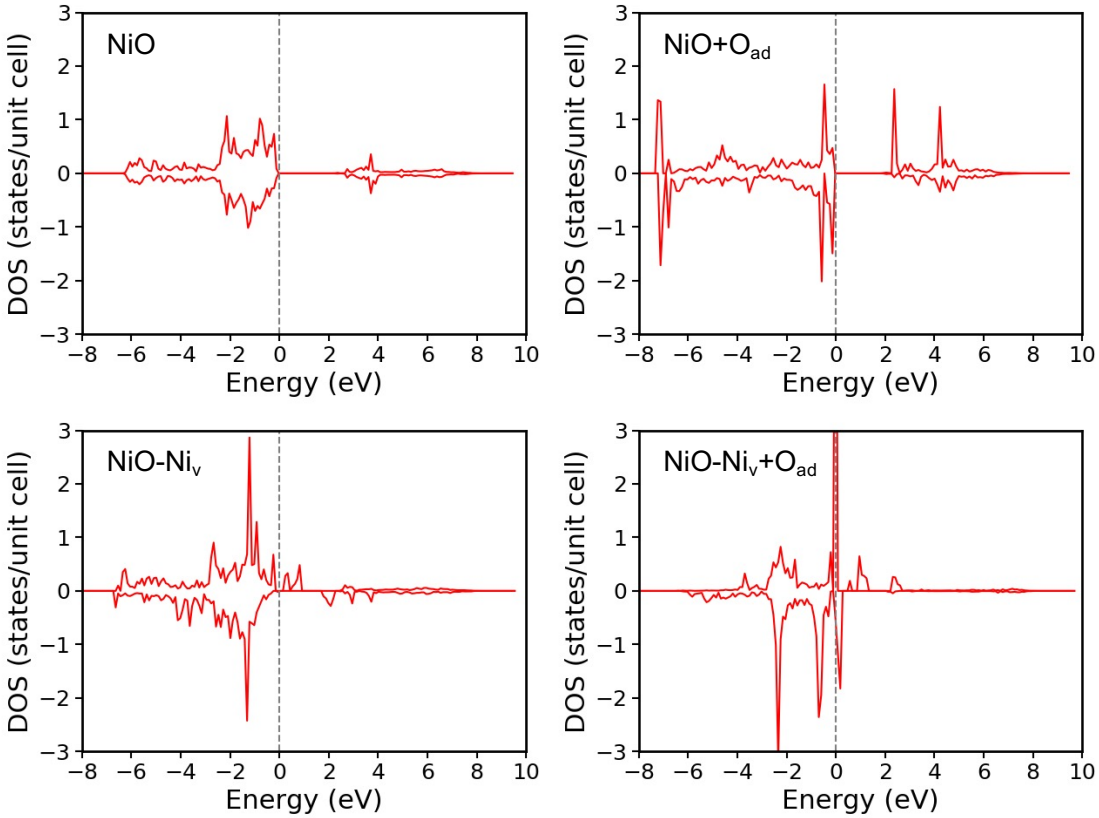

Figure A3. The density of state of *2p* states of lattice O in NiO, the O adatom in NiO (NiO+O_{ad}), the lattice O near a Ni vacancy (NiO-Ni_v) and the O adatom near a Ni vacancy (NiO-Ni_v+O_{ad}).

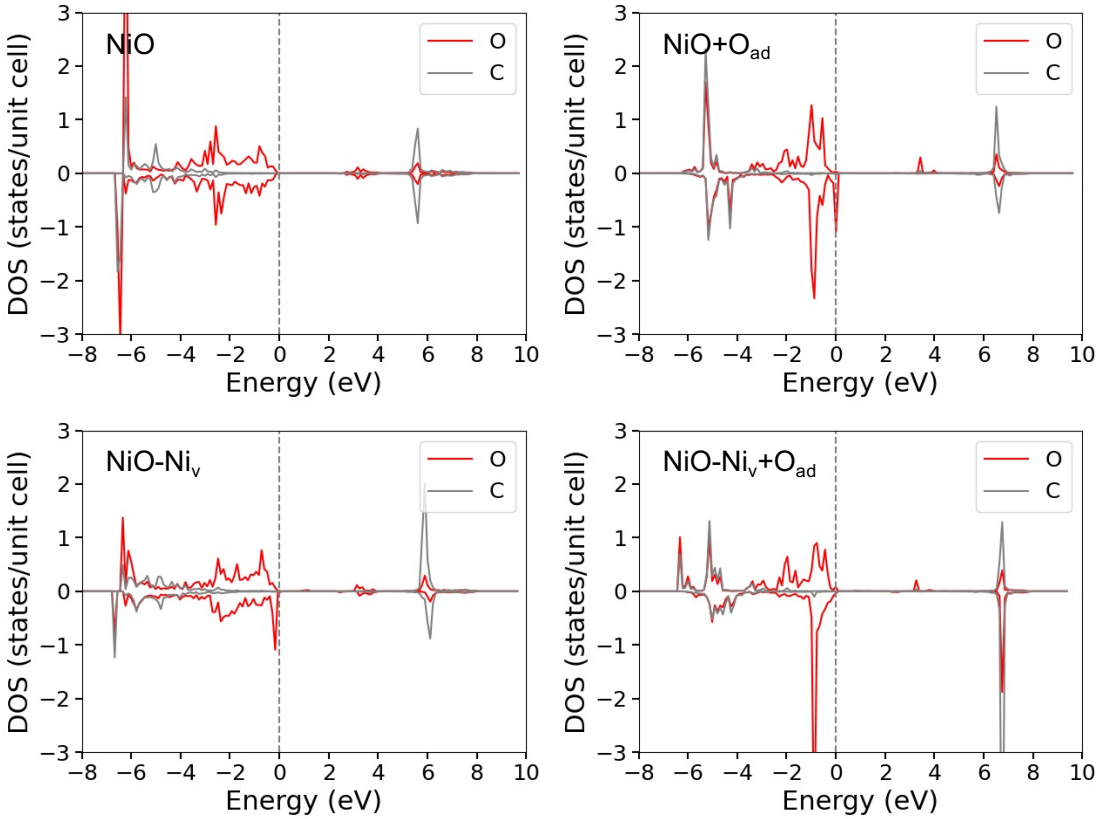

Figure A4. The density of state of *2p* states of C in adsorbed CO_2 and the O that it binds to: lattice O in NiO, the O adatom in NiO (NiO+O_{ad}), the lattice O near a Ni vacancy (NiO-Ni_v) and the O adatom near a Ni vacancy (NiO-Ni_v+O_{ad}).

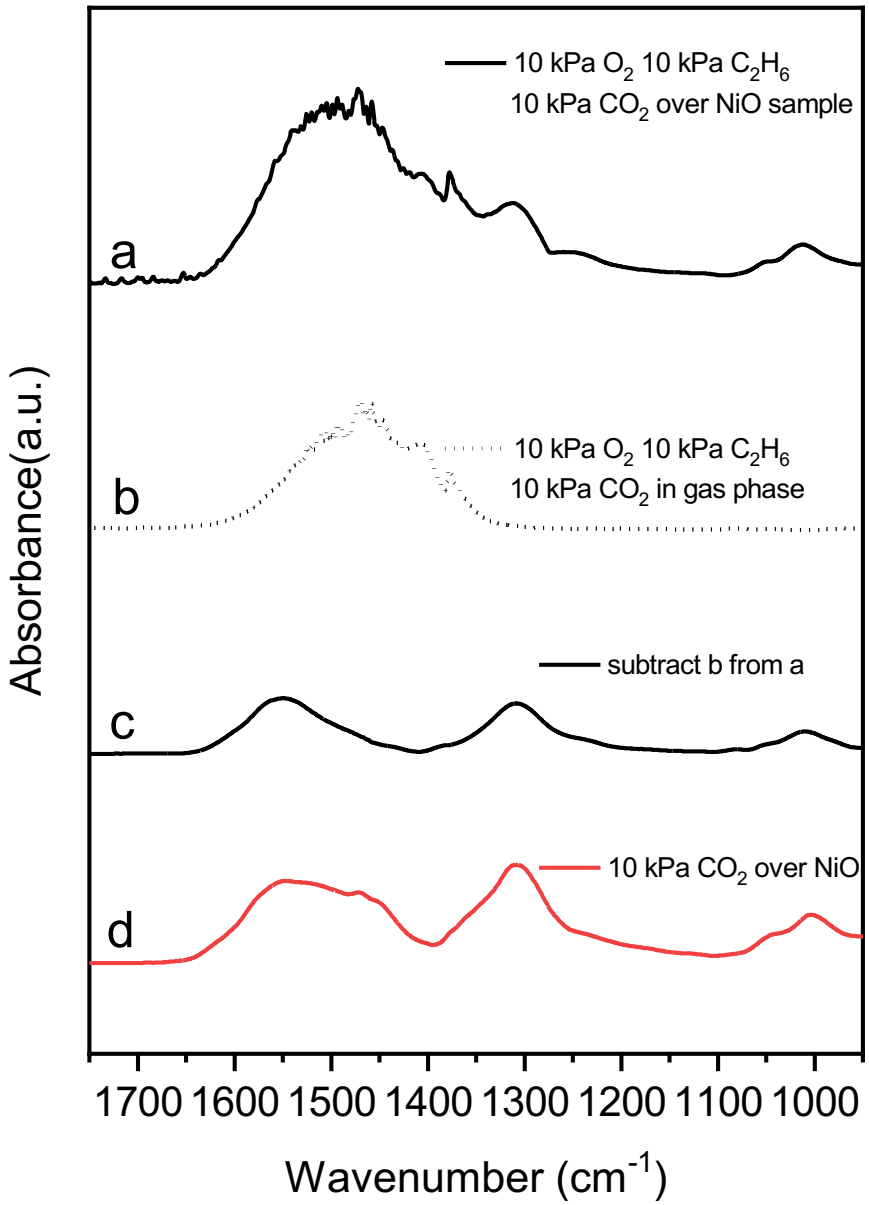

Figure A5. FTIR spectra of 10 kPa O_2/ 10 kPa C_2H_6/ 10 kPa CO_2 (a) over NiO and (b) in gas phase, at 300 °C. Spectrum shown in (c) was obtained by subtracting spectrum (b) from (a). (d) FTIR spectrum of 10 kPa CO_2 over NiO at 300 °C.

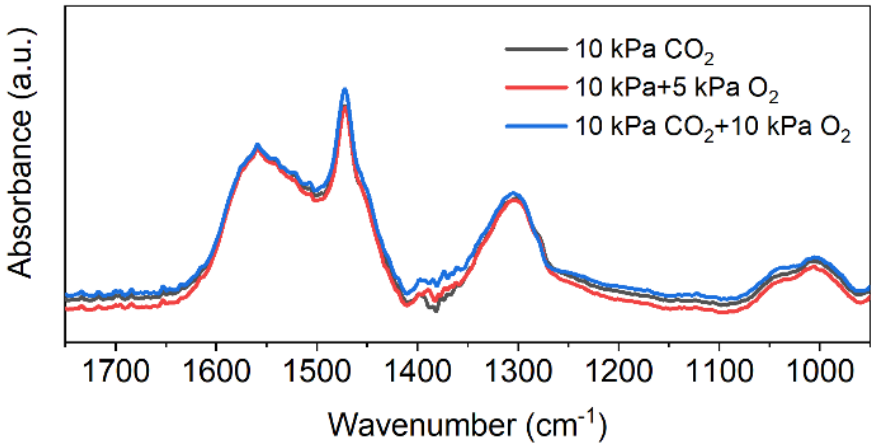

Figure A6. FTIR spectra of NiO with 10 kPa CO_2 and 0-10 kPa O_2 at 300 °C.

Table A3. Reaction enthalpy ΔH (eV) of ethane C-H bond scission over NiO and NiO-+O_{ad}.

Site	Reaction Enthalpy ΔH (eV)	
	$C_2H_6 \rightarrow C_2H_5 + H$	$C_2H_5 + H \rightarrow C_2H_4 + 2H$
NiO	1.57	0.98
NiO+O_{ad}	-1.34	0.0.01

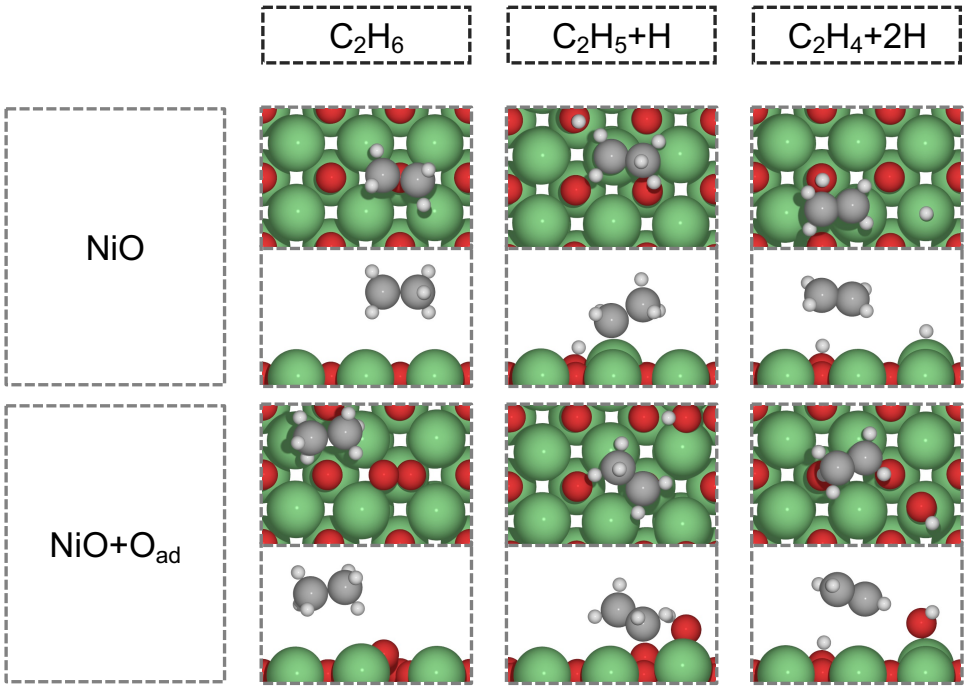

Figure A7. Top and side views of ethane C-H bond scission configurations on NiO and NiO+O_{ad}.

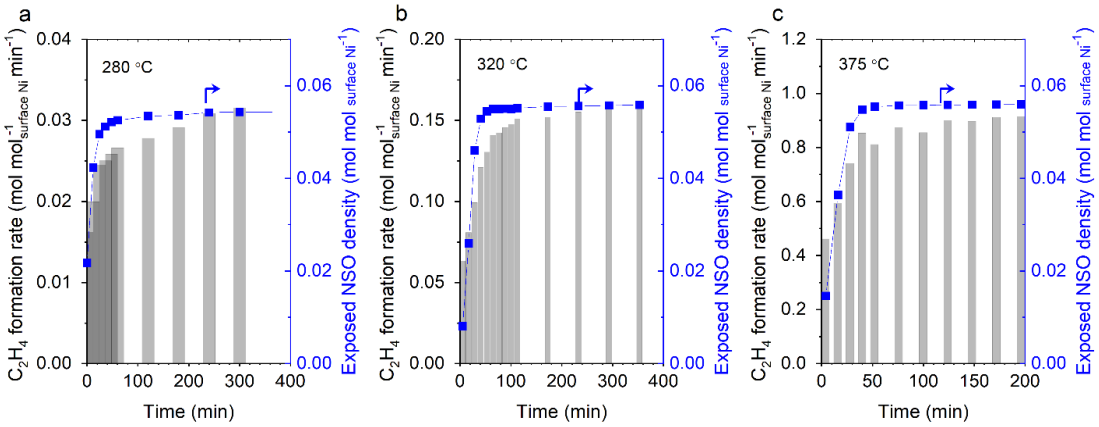

Figure A8. C_2H_4 formation rate after removing CO_2 at (a) 280, (b) 320 and (c) 375 °C. Exposed NSO density is plotted to the right axis, calculated based on CO_2 outlet pressure and CO_2 isotherm predicted by the DSL model.

Example settings for MD simulations of SAMs

```
&GLOBAL
  PROJECT 9C
  RUN_TYPE MD
  PRINT_LEVEL LOW
&END GLOBAL
&FORCE_EVAL
  METHOD QS
  &SUBSYS
    &CELL
      A 5.088814941 0.0 0.0
      B 2.54440747 4.407043014 0.0
      C 0.0 0.0 31.19667111
      PERIODIC XYZ
    &END CELL
    &TOPOLOGY
      COORD_FILE_NAME 9C_0.xyz
      COORD_FILE_FORMAT XYZ
    &END
    &KIND H
      BASIS_SET DZVP-MOLOPT-GTH
      POTENTIAL GTH-PBE-q1
    &END KIND
    &KIND C
      BASIS_SET DZVP-MOLOPT-GTH
      POTENTIAL GTH-PBE-q4
    &END KIND
    &KIND O
      BASIS_SET DZVP-MOLOPT-GTH
      POTENTIAL GTH-PBE-q6
    &END KIND
    &KIND Au
      BASIS_SET DZVP-MOLOPT-SR-GTH
      POTENTIAL GTH-PBE-q11
    &END KIND
    &KIND S
      BASIS_SET DZVP-MOLOPT-GTH
      POTENTIAL GTH-PBE-q6
    &END KIND
  &END SUBSYS
  &DFT
    BASIS_SET_FILE_NAME ./BASIS_MOLOPT
    POTENTIAL_FILE_NAME ./GTH_POTENTIALS
    CHARGE 0
    LSD
    &QS
     METHOD GPW
     EPS_DEFAULT 1.0E-6
     EXTRAPOLATION ASPC
    &END QS
    &POISSON
      PERIODIC XYZ
```

```
    &END
    &MGRID
      CUTOFF 500
      NGRIDS 4
      REL_CUTOFF 60
    &END MGRID
    &SCF
      SCF_GUESS ATOMIC
      EPS_SCF 1.0E-04
      MAX_SCF 500
      &OT
       MINIMIZER DIIS
      &END OT
      &MIXING T
        ALPHA 0.5
        METHOD PULAY_MIXING
        NPULAY 5
      &END MIXING
      &PRINT
        &RESTART OFF
        &END RESTART
      &END PRINT
    &END SCF
    &XC
      &XC_FUNCTIONAL PBE
      &END XC_FUNCTIONAL
       &VDW_POTENTIAL
         POTENTIAL_TYPE PAIR_POTENTIAL
         &PAIR_POTENTIAL
            TYPE DFTD3
            REFERENCE_FUNCTIONAL PBE
            PARAMETER_FILE_NAME ./dftd3.dat
            R_CUTOFF 15
         &END PAIR_POTENTIAL
       &END
    &END XC
  &END DFT
&END FORCE_EVAL
&MOTION
  &MD
    ENSEMBLE NVT
    STEPS 5000
    TIMESTEP [fs] 1
    TEMPERATURE [K] 298.0
    &THERMOSTAT
      TYPE NOSE
      REGION GLOBAL
      &NOSE
        LENGTH 3
        YOSHIDA 3
        MTS 2
        TIMECON [wavenumber_t] 1000
      &END NOSE
    &END THERMOSTAT
  &END MD
```

```
  &CONSTRAINT
    &FIXED_ATOMS
      COMPONENTS_TO_FIX XYZ
      LIST 1 2 3 4 5 6 7 8 9 10 11 12
    &END FIXED_ATOMS
  &END CONSTRAINT
  &PRINT
    &TRAJECTORY
      &EACH
        MD 1
      &END EACH
    &END TRAJECTORY
    &VELOCITIES
      &EACH
        MD 1
      &END EACH
    &END VELOCITIES
    &FORCES
      &EACH
        MD 1
      &END EACH
    &END FORCES
    &RESTART_HISTORY
      &EACH
        MD 500
      &END EACH
    &END RESTART_HISTORY
  &END PRINT
&END MOTION
```

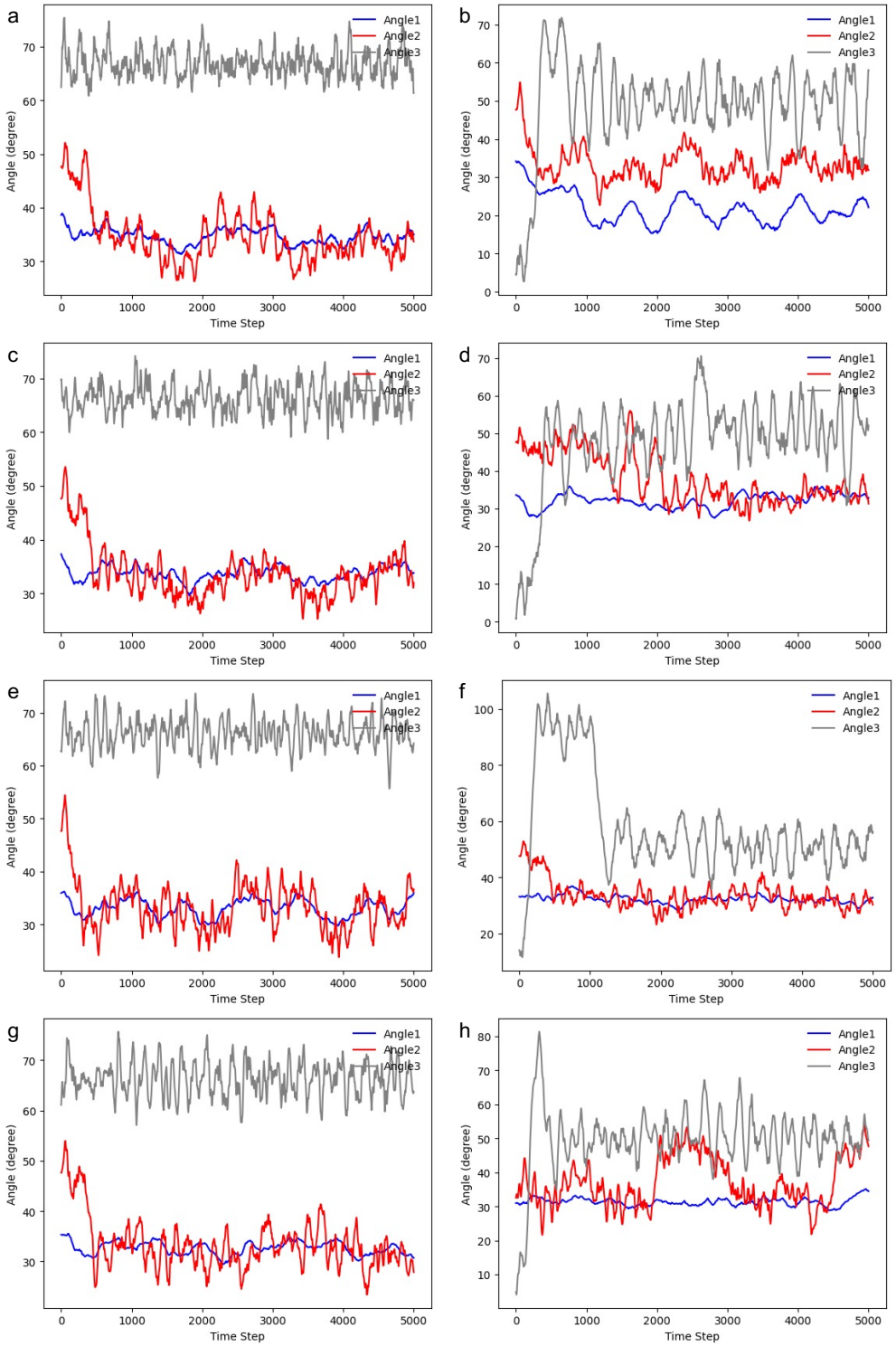

Figure A9. Angle θ_1 (blue), θ_2 (red) and θ_3 (grey) monitored along time for CH_3-$(CH_2)_n$-OS_2 SAMs with n = 8-15 as shown from a to h.

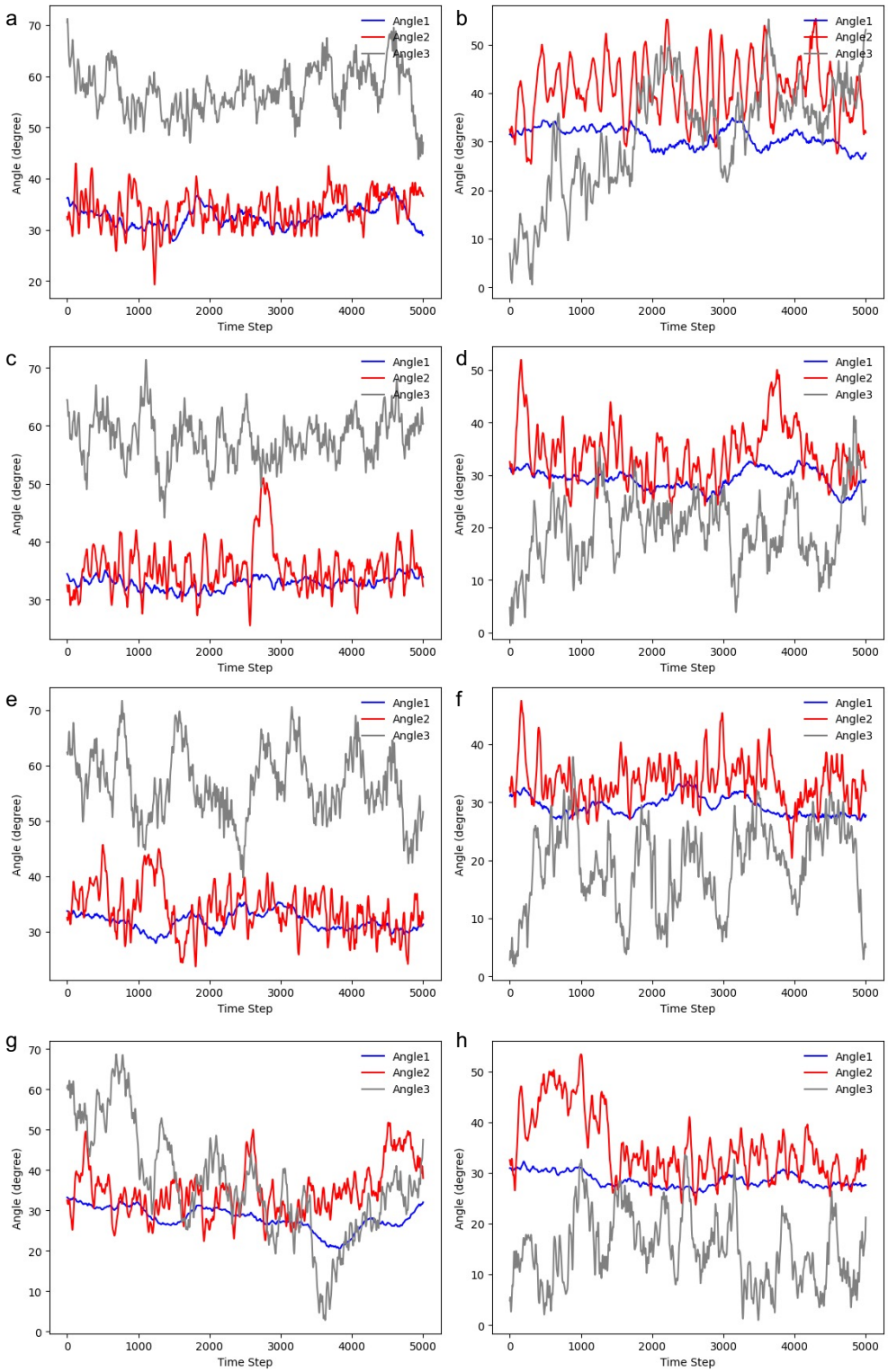

Figure A10. Angle θ_1 (blue), θ_2 (red) and θ_3 (grey) monitored along time for CF_3-$(CH_2)_n$-OS_2 SAMs with n = 8-15 as shown from a to h.